Spring 2018

# Nonlinear finite element analysis of concrete columns subjected to complex loading

Adam Christopher Morgan



Department:

# NONLINEAR FINITE ELEMENT ANALYSIS OF CONCRETE COLUMNS SUBJECTED TO COMPLEX LOADING

by

ADAM CHRISTOPHER MORGAN

A THESIS

Presented to the Faculty of the Graduate School of the

MISSOURI UNIVERSITY OF SCIENCE AND TECHNOLOGY

In Partial Fulfillment of the Requirements for the Degree

MASTER OF SCIENCE IN CIVIL ENGINEERING

2018

Approved by

Dr. Lesley H. Sneed, Advisor
Dr. John J. Myers
Dr. Cesar Mendoza

## ABSTRACT

This study details the development and implementation of a finite element model within a commercial finite element code, Abaqus CAE, for the analysis of reinforced concrete (RC) bridge columns containing interlocking spirals subjected to combined loading conditions including axial, shear, bending, and torsional loads, including the post-peak response. The model is a first of its kind attempt at simulating the response of RC columns with continuous spiral transverse reinforcement and subjected to combined loading conditions including torsion. The model is utilized to determine the quasi-static load-deformation response under various proportions of the input loads and displacements. The resulting quasi-static load-deformations, i.e., 'backbone' relationships, are compared to those experimentally obtained for three 1/2-scale prototype RC bridge columns subjected to constant axial loading and slow reversed cyclic lateral loading resulting in combined flexural moment, shear, and torsional moment. It was determined that such models can simulate the behavior of such columns with a reasonable level of error for unidirectional loading, but accurate torsional response and numerical stability of such models is difficult to obtain due to convergence errors resulting from a combination of inelastic material models and multi-body constraints used to couple the motion of the column's constituent pieces together. Attempts were made to extend the finite element model to similar RC bridge columns repaired and strengthened with externally bonded fiber reinforced polymer (FRP) composite jackets, however such attempts resulted in convergence failure as the model approached inelastic behavior.

## ACKNOWLEDGMENTS

I would like to start by thanking my lovely wife, Amanda, for all her patience while I have pursued my degrees. Furthermore, I would like to thank my parents for their continued support and faith in me and their support when I've needed it. Additionally, I would like to thank my Aunt Marge and Uncle Tom Schueck for their support which made my education possible.

I would especially like to thank Dr. Lesley Sneed for her guidance, tutelage, hard work, and excessively critical eye as I have progressed not only on this project, but through the whole of my education. I would also like to thank the members of my committee, Dr. John J. Myers, and Dr. Cesar Mendoza, for their knowledge, assistance, and support. Similarly, I would like to thank Dr. Mehdi "Saiid" Saiidi, Dr. Abdeldjelil "DJ" Belarbi, and Dr. K. Chandrashekhara for their input and assistance on the project.

For making this project possible I want to thank: The California Transportation Department (Caltrans), National University Transportation Center (NUTC) at Missouri S&T, Paul Sansone and V. L. Goedecke Corp., Patrick Schueck and Prospect Steel/Lexicon, PileMedic LLC, James Morgan, and Stephen Scott and Grainger.

Lastly for their assistance and support I would like to thank Yang Yang, Ruili He, Jason Cox, and John Bullock.

# TABLE OF CONTENTS

## LIST OF ILLUSTRATIONS

Page

# LIST OF TABLES

Page

# 1. INTRODUCTION

## 1.1. GENERAL

The reinforcement of damaged or deficient structural members by external bonding of fiber reinforced polymer (FRP) composites has become increasingly widespread in recent decades. This can be attributed to several factors ranging from the reduced cost of these systems to their inherent benefits over traditional repairs systems; being that they are lightweight, relatively easy to implement, and noncorrosive. The effectiveness and efficiency of these repairs and/or retrofits involving FRP are dependent on the accuracy of the analysis used in their design.

An element in any structural system can be subjected to one or more of four load types: axial forces, bending moments, shearing forces, and torsional moments. The combination of these loads on a structural member can results in complex internal stress distributions due to the complexity in the loading conditions, the constituent relations of the materials composing the member, and/or the geometric conditions of the member. Analyzing the response of a perfectly elastic structural element subject to complex loadings can be challenging, but analyzing the nonlinear behavior of concrete structural elements provides yet another layer of difficulty. The complexity of analysis of reinforced concrete (RC) members is made more complicated by the relative contributions of the internal reinforcing steel to the load resistance, the steel's influence on the concrete behavior, and in the case of FRP-strengthened RC members the contribution of the FRP, all of which exhibit varying degrees of inelasticity or brittle behavior.

In cases where complex loading, complex geometries, and/or complex material interactions exist it may be advantageous to discretize the structural member into a series of well understood discrete elements. In this way one complex analysis can be simplified into many simpler analyses. The stresses and/or strains imposed on a given element are dependent on those in an adjacent element. The cumulative result of the deformations of these elements is analogous to the displacements of the structural member that they represent. This process is collectively known as the finite element method (FEM), and the practical implementation and results are known as finite element analysis (FEA).

This process, which would be cumbersome by hand due to the large volume of calculations, is made practical through the use of computer software to handle the simultaneous solution of the system of thousands of equations that represent the internal responses of the elements and their interactions. Through FEA even complex conditions can be analyzed and investigated to determine the load-response sensitivity to changes in geometry or material properties. Once such a model is properly calibrated to experimental results it can be used to provide further insight into those physical experiments or to artificially expand upon their test matrix without the need for costly physical specimens.

A logical first step in the development of models to simulate the behavior of FRP-strengthened RC columns is to develop models that are proven to be able to simulate the behavior of precursory unstrengthened RC columns. This study outlines the development of such a model, which was the first of its kind for RC columns reinforced with continuous spiral transverse reinforcement and subjected to combined loading conditions including torsion. Then attempts were made to extend the model to the case of similar RC columns that were externally strengthened with FRP jackets. Although these attempts were unsuccessful, in this thesis work, lessons learned in this study can be used to help guide future studies for the simulation of FRP-strengthened RC columns with complex reinforcement and loading conditions.

## 1.2. OBJECTIVE AND SCOPE

The objective of the research presented in this thesis is to develop a three-dimensional (3D) finite element model of RC bridge columns with an oval shaped cross-section and interlocking spiral transverse reinforcement. The model is used to simulate the response of three such RC columns subjected to combined flexure, shear, torsion, and axial load.

Typically, geometric complexities associated with the helical spiral reinforcement would be simplified and simulated as discreet hoops of reinforcement, rather than a continuous spiral. While this simplification allows for conformal meshing (where the elements of two bodies share the same nodes), it also precludes the possibility of accounting for higher order effects, such as variations in confinement due to the locking

and un-locking behavior of the spiral under torsion (Li & Belarbi, 2011). In order to account for the phenomena unique to this reinforcement layout, helical reinforcement is simulated and the non-conformal meshes handled via constraints between the various bodies of the model.

The research presented within this thesis focuses mainly on the discussion of the development of this finite element model for unstrengthened RC columns and its correlation to experimental results published in the literature (Li, 2012). The physical column specimens to which the model is compared were tested to failure and then later repaired with an externally bonded FRP jacket, repair grout, and in the case of two columns replacement bar segments attached with mechanical bar couplers in a follow up study (Yang, 2014). Due to numerical stability issues, convergence of the modified version of finite element model, discussed in this thesis, could not be obtained for the repaired columns. The simulation of these repaired columns is considered outside the scope of this thesis, and FRP repair is discussed only to provide context to the experimental study and future work discussed in Section 5.2.

### 1.3. RESEARCH METHODOLOGY AND THESIS CONTENT

Because RC columns have been tested, and their behavior fully documented, the constitutive relations in the finite element model are developed in such a way to predict these known responses. Section 2 of this thesis discusses, among other topics, a variety of material models that have been developed, tested, and reported by researchers, as well as those developed and implemented into the commercial finite element code Abaqus CAE, which was used in the development of the finite element model. A description of the construction and test setup for both the original and repaired columns is presented in Section 3 of this thesis in order to give context to the setup of the finite element model and the corresponding simulation results of three columns that are presented in Section 4 of this thesis. Section 5 summarizes work and provides conclusions and recommendations for future work.

# 2. LITERATURE REVIEW

## 2.1. EXPERIMENTAL STUDIES

This section of the literature review provides an overview of experimental studies reported in the literature that are most closely related to this project. Section 2.1.1 focuses on studies involving unstrengthened RC columns, particularly experimental studies including oval shaped RC columns with interlocking spirals or studies that have utilized a similar test setup to the present study. Of particular interest is the study by Li and Belarbi (2011), described in Section 2.1.1.2, that included the testing of the columns that were later repaired as part of the experimental portion of this study. Section 2.1.2 focuses on studies related to the repair of seismically damaged RC columns. Again, focus is given to studies with a test setup or repair scheme similar to the present study, such as those where the repair technique included externally bonded FRP reinforcement and/or included considerations in the repair for fractured reinforcing bars.

**2.1.1. RC Columns.** This section begins by presenting historical works related to oval RC columns with interlocking spirals and concludes with an overview of the study that supplied the damaged columns that were repaired as part of the experimental portion of this project. The construction of the specimens and their failure modes are presented for each of the studies in order to provide an impression of the behavior of oval columns with interlocking spirals.

**2.1.1.1. Tanaka H., (1990).** This study tested four 2.88 m tall RC columns under a constant axial load with a cyclic reversed lateral load applied at the cap resulting in combined shear and bending moment. The results of this study were later published in the ACI Structural Journal (Tanaka & Park, 1993). Of the four columns, one had a 23.6 in. (600 mm) by 15.7 in. (400 mm) rectangular cross section with rectangular hoops. The remaining three columns were 23.6 in. (600 mm) by 15.7 in. (400 mm) oval shaped columns with interlocking spirals. Of the three oval columns, two were constructed with a spiral spacing of 3.15 in. (80 mm) and 2.95 in. (75 mm) in order to meet the minimum requirements for confinement and shear of the New Zealand concrete design code (NZS 3101-Part 1, 1982) (NZS 3101-Part 2, 1982). The third oval column was constructed with a spiral spacing of 100 mm. The spiral spacings of 3.15 in. (80 mm), 3.94 in. (100

mm), and 2.95 in. (75 mm) result in transverse reinforcement ratios of 1.08%, 0.92%, and 1.15%, respectively. The rectangular column had a transverse reinforcement ratio of 2.17% with a spacing of 3.15 in. (80 mm). The column details are shown in Figure 2.1.

In addition to varying the transverse reinforcement ratio, the constant axial load imposed during the test was varied as a percentage of the concrete nominal compressive strength multiplied by the gross area. For both the rectangular column and the oval column with spiral spacing of 3.15 in. (80 mm), the axial load percentage was 10%. For the oval column with spiral spacing of 3.94 in. (100 mm), the axial load percentage was 30%. For the oval column with a spiral spacing of 2.95 in. (75 mm), the axial load percentage was 50%. Each column was loaded under displacement control to varying levels of displacement ductility ($\mu_\Delta$). The load protocol consisted of one cycle of $\mu_\Delta = \pm 0.75$ followed by two cycles of $\mu_\Delta = \pm 2, \pm 4, \pm 6, \pm 8$, etc. The cycles increased by displacement ductility factors of two until failure.

The testing of the three oval columns was terminated when the first spiral fractured. This occurred at $\mu_\Delta = 10$ for the column with a spiral spacing of 3.15 in. (80 mm), during the loading towards $\mu_\Delta = 12$ for the column with spiral spacing of 3.94 in. (100 mm), and on the second cycle at $\mu_\Delta = -12$ for the column with spiral spacing of 2.94 in. (75 mm). In the oval columns, yielding of the spiral reinforcement due to confinement forces was observed at displacement ductility factors as low as $\mu_\Delta = 3$ or 4, while yielding due to shear did not occur until displacement ductility factors of between $\mu_\Delta = 6$ to 8. In the rectangular column, yielding of the hoops was not observed at any displacement level during the test. In all cases, buckling of the longitudinal reinforcement was observed at or above a displacement ductility factor of $\mu_\Delta = 8$. In all cases, the measured maximum moment exceeded the value predicted by the code approach (ACI 318, 1989) (NZS 3101-Part 1, 1982) that had been used to determine the loading protocol. However, the maximum moment was more accurately predicted by accounting for strain hardening of the reinforcement and using the concrete constitutive relation described by Mander, et al. (1988). It was also found that the code approach resulted in conservative estimates of flexural strength, particularly when the axial load was relatively high, due to neglecting the effects of lateral confinement.

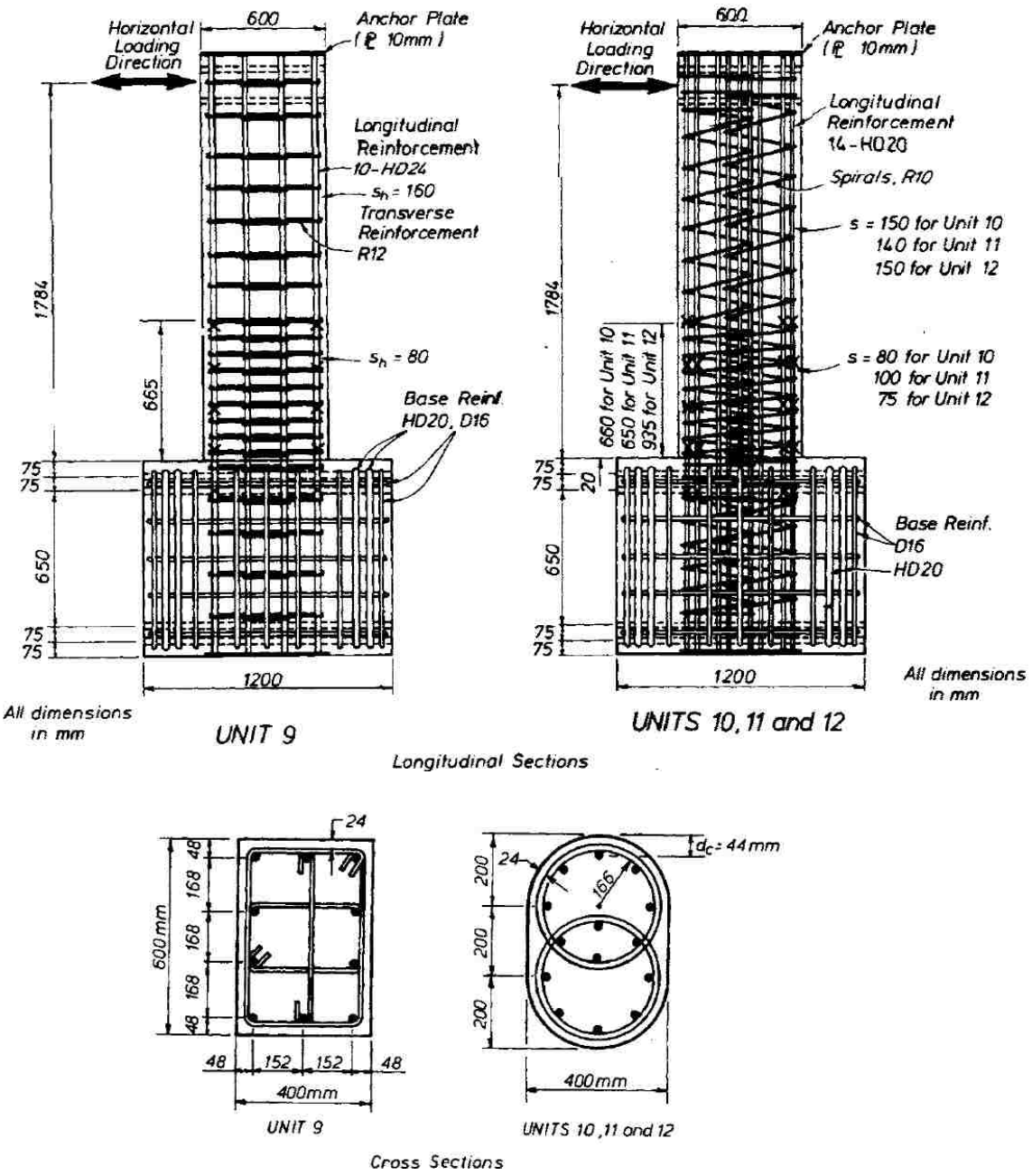


Figure 2.1 - Details of Columns (Tanaka and Park, 1993)
(1 in. = 25.4 mm)

This study provided insight into the behavior of oval RC columns with interlocking spirals. It showed that oval RC columns with interlocking spirals required substantially less transverse reinforcement than columns with rectangular hoops to

provide confinement of the concrete core. Additionally, it showed the importance of using appropriate material models and the need to use alternative analysis methods, such as the combined beam-arch theory, to accurately predict the flexural strength of these types of columns.

**2.1.1.2. Li and Belarbi, (2011).** This study tested three oval shaped RC columns with interlocking spirals under combined loading with torsional moment-to-bending moment ratios (T/M) of 0.2, 0.4, and Infinity (pure torsion). The columns were half-scale having an oval cross section of 610 mm by 915 mm with 25.4 mm of concrete cover. The columns were 3.35 m from the top of footing to the centerline of the applied lateral loads. The longitudinal reinforcement was provided by 20 No. 8 (25 mm dia.) bars that provided a longitudinal reinforcement ratio of 2.13%. The transverse reinforcement was provided by two interlocking spirals consisting of No. 4 (13 mm dia.) bars at a 70 mm pitch that provided a transverse reinforcement ratio of 1.32%. The details of these columns are depicted in Figure 2.2.

All columns were tested with a constant axial load corresponding to 7% of the column's axial capacity to account for superstructure dead load. The initial cyclic loading was performed under force control at intervals equivalent to 10% of the anticipated yield load until first yielding of the longitudinal bars was observed for specimens tested under combined loading, or until first yielding of the transverse reinforcement for the specimen tested under pure torsion. The displacement corresponding to first yielding of the reinforcement was defined as displacement ductility equal to one ($\mu_\Delta = 1$) for the specimens tested under combined loading or twist ductility equal to one ($\mu_\theta = 1$) for the specimen tested under pure torsion. Loading was performed under displacement control after the point of first yield. Three loading cycles were performed at each ductility stage in order to observe stiffness degradation characteristics.

All three specimens were tested to failure resulting in levels of severe damage including degradation of the core material. The torque-twist relation was linear up to the cracking torsional moment, of approximately 50% of the yield torque, in the specimen subjected to pure torsion. After cracking the torque-twist relationship became nonlinear with decreasing torsional stiffness. During 'positive' ductility cycles the spirals tended to unlock, resulting in reduced confinement and greater spalling compared to the 'negative'

ductility cycles where the spirals locked. This locking and unlocking resulted in asymmetric hysteresis loops with the 'negative' ductility cycles having greater load resistance. The specimen subjected to pure torsion exhibited diagonal cracks that began to develop at mid height that lengthened and widened as the test progressed, and the concrete cover eventually spalled off. Spalling of the concrete cover progressed to nearly the full height of the column, and a torsional hinge developed above mid-height where significant crushing of the core concrete occurred.

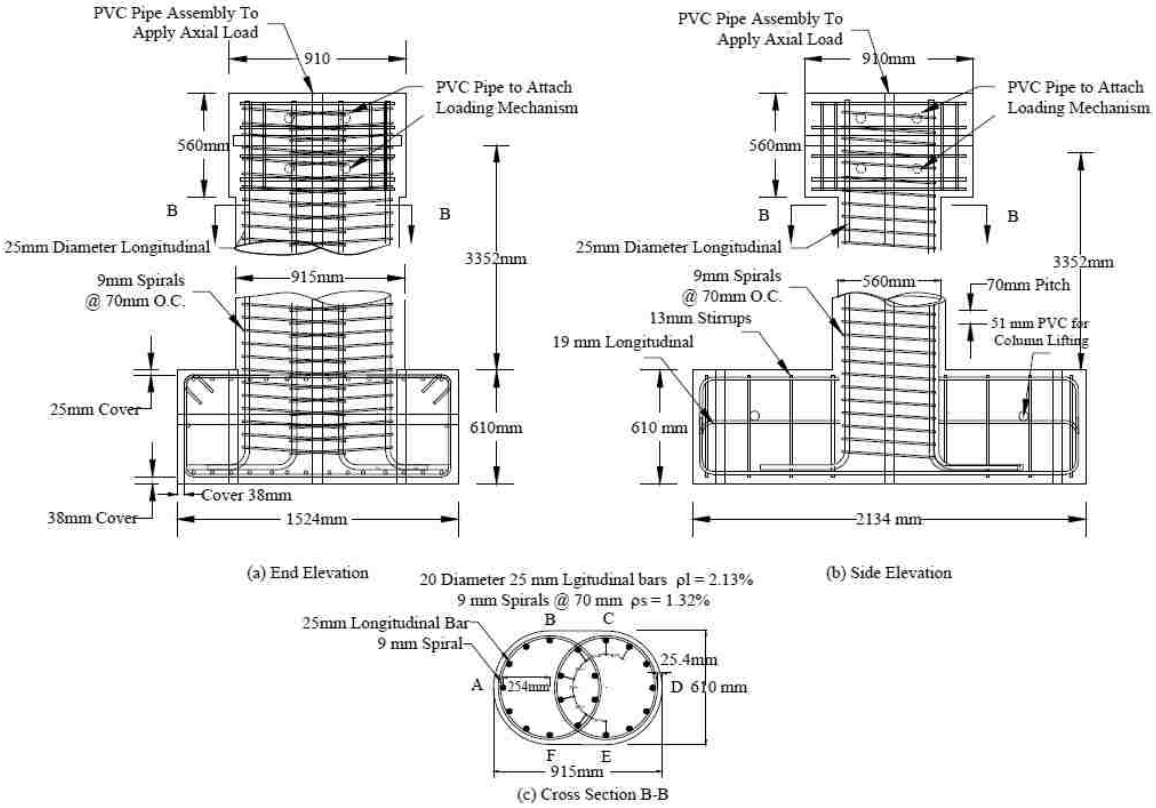


Figure 2.2 - Details of Oval Columns with Interlocking Spirals (Li & Belarbi, 2011)
(1 in. = 25.4 mm)

The two columns tested under T/M of 0.2 and 0.6 exhibited initial flexural cracks at approximately 40% of the yield strength. The orientation of these cracks became more

inclined under repeated cycling and increased load. As the loading progressed, shear cracks began to form and additional flexural cracks began to form further up the column. For the specimen tested with a T/M of 0.6, yielding of the longitudinal bars was accompanied by yielding of the spiral reinforcement. For the column tested with a T/M of 0.2, the spirals did not yield until a ductility factor of $\mu_{\Delta} = 6$. For the column tested with a T/M of 0.2, spalling of concrete cover and formation of the plastic hinge occurred in the bottom 0.6 m of the column, while in the column tested at a ratio of 0.6, the spalling spread throughout the bottom two thirds of the column, and the plastic hinge developed higher. The loading progressed until severe degradation of the core material in the plastic hinge and eventual buckling and rupture of longitudinal reinforcement occurred. Similar to the specimen tested under pure torsion, an asymmetric hysteretic behavior was observed. This was not only due to the locking and unlocking the spirals, as was present in the column tested under pure torsion, but also because one side of the specimen was always subjected to shear stress due to combination of the shear and torsional forces. During the repeated cycling at the same ductility factor, it was found that the strength degradation between the first and second cycle was greater than between subsequent cycles.

**2.1.2. Repaired RC Columns.** This section begins by presenting historical works related to columns that were repaired. The construction of the specimens and their failure modes are presented for each of the studies in order to provide an impression of the behavior of repaired columns.

**2.1.2.1. Lehman, Gookin, Nacmuli, and Moehle (2001).** In this study four circular reinforced concrete columns, which had been previously damaged under simulated seismic loading and were later repaired, under simulated seismic loading consisting of cyclic lateral loading and a constant axial load. Three of the columns were constructed and severely damaged as part of another study (Lehman & Moehle, 1998), while the fourth column was only subjected to moderate damage, prior to repair, and was constructed as part of this 2001 study.

The four columns were originally constructed to be nearly identical, varying only in the longitudinal reinforcement ratio. The columns were 24 in. (610 mm) diameter 8 ft. (3.8 m) tall, measured from the top of the footing to the centerline of the applied lateral

load. The three columns originally constructed as part of the 1998 study contained 11, 22, or 44 evenly spaced No. 5 (16 mm dia.) longitudinal reinforcing bars spaced to provide a longitudinal reinforcement ratio of 0.75%, 1.50%, or 3.00%, respectively. These three columns were denoted as 407S, 415S, and 430S, respectively. The fourth column, constructed as part of the 2001 study, included 22 evenly spaced No. 5 (16 mm dia.) longitudinal reinforcing bars and was denoted as 415M. In all cases, transverse reinforcement was provided by spiral reinforcement comprised of a 0.25 in. (6mm) diam. wire spaced at 1.25 in. (32 mm) on center, for a transverse reinforcement ratio of 0.70%. The details of these columns are depicted in Figure 2.3.

Prior to repair each column was damaged under simulated seismic loading. This consisted of a constant applied axial load and a cyclically applied lateral displacement. The axial load was selected to be 147 kips (654 kN) based on approximately 7% of the gross cross-sectional area of the column multiplied by the concrete compressive strength. The applied lateral displacement consisted of three fully reversed cycles at increasing displacement levels. For displacement levels in the post-yield regime an additional fully reversed cycle was added with an amplitude 1/3 that of the previous three cycles. These displacement levels monotonically increased by a factor of between 4/3 and 2, as shown in Figure 2.4.

The damage due to this loading varied between the specimens. In the case of columns 407S, 415S, and 430S, they were tested until severe damage occurred and a strength reduction of more than 20% was observed. This resulted in yielding of all longitudinal reinforcement, yielding and fracture of transverse reinforcement, crushing of core concrete, and extensive cracking and spalling of concrete cover within the plastic hinge region. In the case of column 415M, which was constructed identically to column 415S, only a subset of the cycles applied to 415S were applied until a level of moderate damage occurred, as defined by ATC (1996). The damage to 415M included yielding of the extreme longitudinal reinforcement, cracking with residual openings, and spalling of the concrete cover. The damage to the four columns is summarized in Table 2.1.

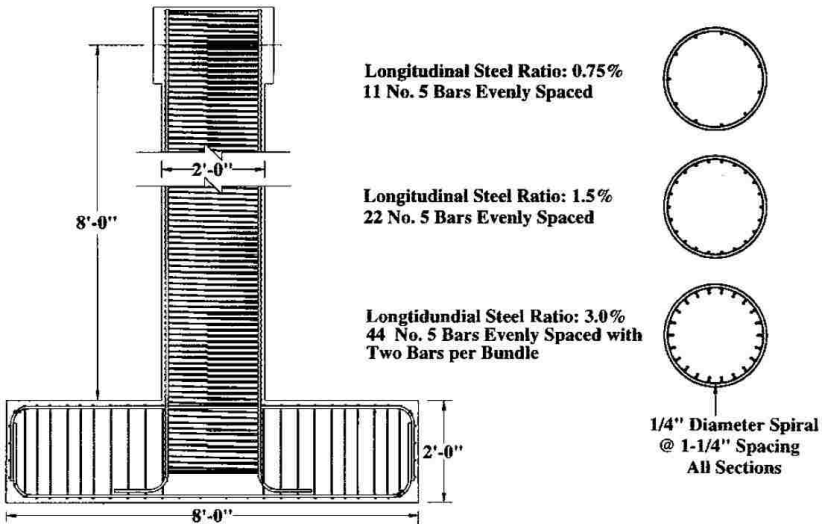


Figure 2.3 - Original Column Geometry (Lehman, et al., 2001)
(1 in. = 25.4 mm)

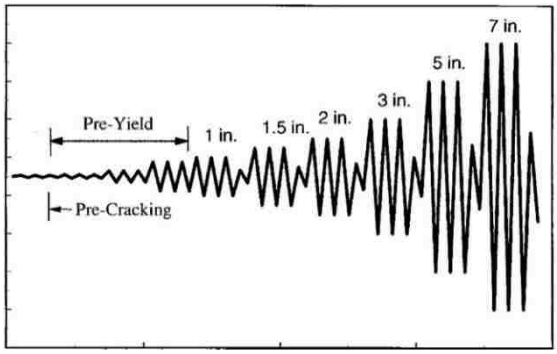


Figure 2.4 - Imposed Lateral Displacement History (Lehman, et al., 2001)

Table 2.1 - Column Damage Summary (Lehman, et al., 2001)

| | Concrete Damage | | Reinforcing Steel Damage | | | | |
|---|---|---|---|---|---|---|---|
| Column | Spalled height (in.) | Core crush depth (in.) | Yielding of longitudinal bars | No. of bucked longitudinal bars | No. of fracture longitudinal bars | No. of fractured sprials | Damage Level |
| 407S | 14 | 2 | All bars | 7 | - | 8 | Severe |
| 415M* | 15 | 0 | Extreme bars | 0 | 0 | 0 | Moderate |
| 415S* | 18 | 7 | All bars | 22 | 9 | 4 | Severe |
| 430S | 15 | 8 | All bars | 44 | 0 | 8 | Severe |

*With exception of final damage state, Columns 415M and 415S were nominally identical

The damage states of the four columns as well as their construction provided for differing repair schemes. Each of the repaired configurations is denoted with an "R" as a suffix. For example, the repaired configuration of column 430S is denoted 430SR. An overview of what each repair entails follows.

The repair of column 407S involving removal and replacement of the bottom 36 in. (914 mm) with a 28 in. (711 mm) diameter section, 4 in. (102 mm) wider than the original column. This wider section extended an addition 7 in. (178 mm) beyond where the column was severed. Additionally, loose concrete was removed and the longitudinal reinforcement severed an additional 6 in. (178 mm) below the column base. Eleven new No. 5 (15.9 mm diameter) longitudinal reinforcement bars were spliced to the existing reinforcement via mechanical couples. The use of mechanical couplers was deemed feasible due to the relatively low congestion afforded by the longitudinal reinforcement. The use of mechanical couplers was deemed inappropriate for the more congested repairs (discussed further on in this section) and thus were unique to 407S. Additionally, new No. 3 (9.5 mm diameter) spiral reinforcement was placed at a pitch spacing of 2.25 in. (57 mm) to match the original transverse reinforcement ratio. The repair configuration of 407S, 407SR, and the corresponding repair design details are shown in Figure 2.5.

Despite nominally identical original construction, the different damages states of columns 415S and 415M required wildly different repairs. The moderately damaged column, 415M, required a far less invasive repair as damage included only yielding of longitudinal reinforcement, cracking of concrete, and spalling of concrete cover. To repair 415M the concrete cover was removed over the lower 18 in. (457 mm) of the column, cracks wider that 0.003 in. (0.07 mm) were epoxy injected in the lower portions of the column, and use of a concrete patching material to replace to spalled and removed concrete. As a result, the repaired configuration of 415M, 415MR, had geometry and reinforcement detailing nominally identical to the original column, as shown in Figure 2.3.

However, column 415S suffered severe damage including all the aspects of 415M's damage as well as buckling of all 22 longitudinal reinforcing bars, fracture of nine of the longitudinal reinforcing bars, increased spalling of concrete cover, and crushing of 7 in. (178 mm) of the concrete core.

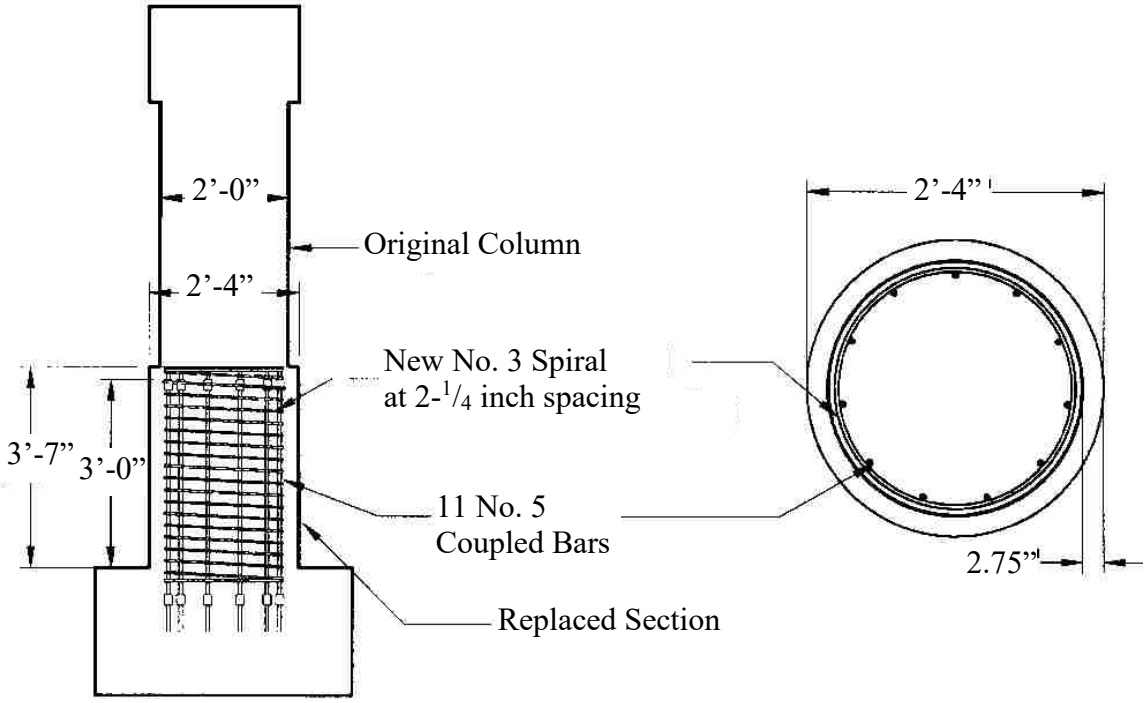


Figure 2.5 - Repair Design for Column 407S (Repaired Designation 407SR) (Lehman, et al., 2001) (1 in. = 25.4 mm)

This was repaired via placement of a so-called strong jacket in the damaged area. This strong jacket consisted of a 20 in. (508 mm) section containing ten double-headed No 6 reinforcing bars, which were embedded 9 in. (229 mm) below the base of the column. In order to ensure a flexural failure prior to reaching the columns shear capacity, the flexural strength above the jacket was reduced by severing six of the existing longitudinal reinforcing bars, 4 in. (102 mm) below the top of the jacket. The force transfer from the existing longitudinal reinforcement to the additional longitudinal reinforcement, installed as part of the repair, was idealized as inclined compressive struts in the concrete between the old and new reinforcement. This results in a horizontal imbalance which must be constrained by the addition of new transverse reinforcement. The requirement was assessed by determining the required transverse reinforcement, at yield stress, required to apply sufficient clamping force to transfer the longitudinal forces through friction, assuming a coefficient of friction of 0.5. This approach required 3/8 in. (9.5 mm) diameter spiral reinforcement at spacing of no more than 1.7 in. (43 mm) to

transfer the longitudinal load. The repair was constructed with a slightly reduced spacing of 1.5 in. (38 mm). Additionally, the repair involved removal of the lower 22 in. (560 mm) of concrete, damaged spiral reinforcement was removed in the bottom 10 in. (250 mm) of the column, fractured bars were repaired with welded lap splices, existing cracks were epoxy injected, and new concrete was cast in the jacket. The repair configuration of 415S, 415SR, and the corresponding repair design details are shown in Figure 2.6.

The design of the repair for column 430S was similar to that of 415S; in that the repair design implemented a strong jacket at the base of the column. Unlike the previously discussed repair design, however, the repair of 430S was intended to force failure below the jacket, as opposed to above. For this reason, the jacket was designed to be 36 in. (914 mm), such that flexural failure was unlikely above the repair. As the repair was designed to match previous flexural capacity and because there was a high level of uncertainty in the capacity of the existing reinforcement, the existing longitudinal reinforcement was severed at the base. The capacity of these now severed reinforcing bars was offset by the placement of an additional 16 No. 6 (15.9 mm diameter) longitudinal reinforcing bars within the strong jacket. These new reinforcing bars were anchored, with a headed side, 12 in. (305 mm) into the base. The design of the transverse reinforcement, within the repair, was done using the same procedure used to design the repair of 415S. However, unlike 415S, where failure was designed to occur above the repair, the design of the transverse reinforcement in 430S's repair was intended to transfer the ultimate stress capacity, 96 ksi (660 MPa), to the transverse reinforcement, through the friction mechanism previously discussed. This required transverse reinforcement consisting of a No. 3 spiral reinforcement at a pitch spacing no more than 1.1 in. (28 mm). The actual repair utilized a slightly lower pitch spacing of 1 in. (25 mm). The repair configuration of 430S, 430SR, and the corresponding repair design details are shown in Figure 2.7.

These four repaired columns, 407SR, 415MR, 415SR, and 430SR, were tested under the same loading, described earlier, and their results compared to that of their severely damaged counter-parts. I.e. 407SR was compared to 407S, 430SR was compared to 430S, and both 415MR and 415SR were compared to the results of 415S.

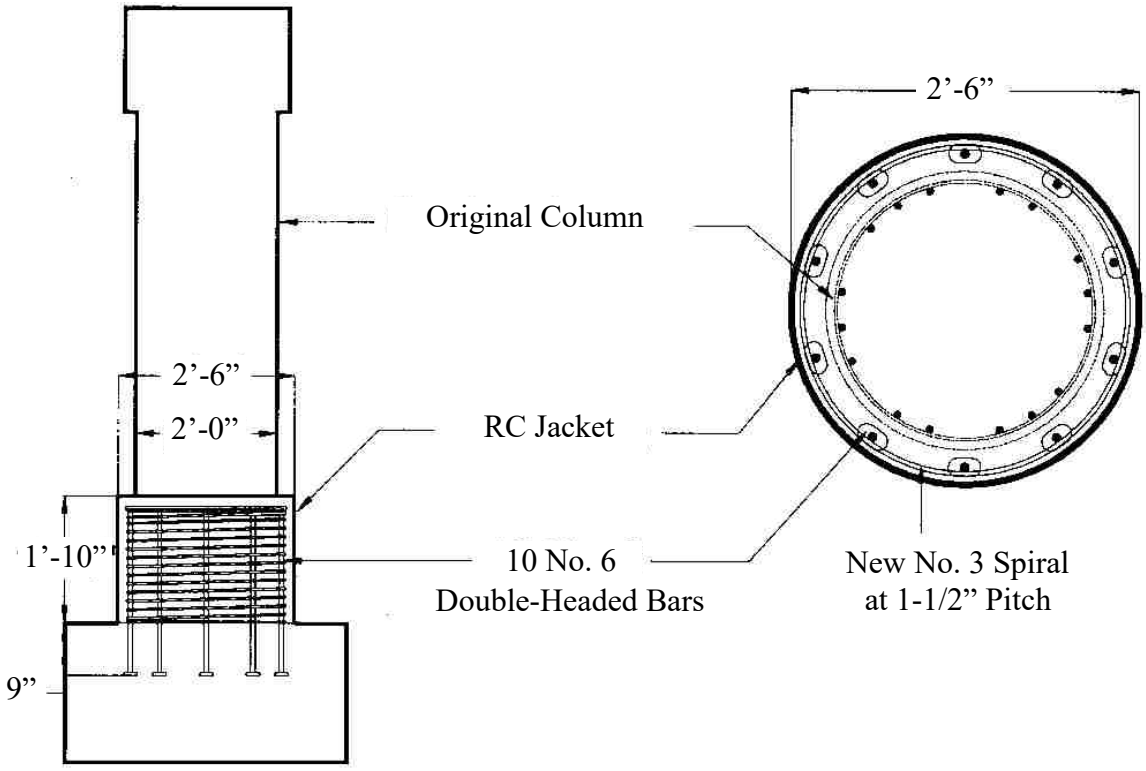


Figure 2.6 - Repair Design for Column 415S (Repaired Designation 415SR) (Lehman, et al., 2001) (1 in. = 25.4 mm)

Additionally, these results were compared to those of a force-displacement model developed under the previous study (Lehman & Moehle, 1998).This discrete model correlated the tip displacement, due to an applied force, resulting from the sum of shear deformation, bending deformation, and end rotation due to slip in the longitudinal reinforcement bond. With ultimate displacement being estimated as that which causes a tensile strain value of 0.08 in./in. (0.08 mm/mm). As this model considers displacements discretely, as opposed to collectively as in a finite element model, it cannot account for loading outside of those which it was designed for (such as torsion). Due to this limitation and an inability to capture post-peak behavior, a detailed overview of this model is considered out-of-scope for the purposes of this study.

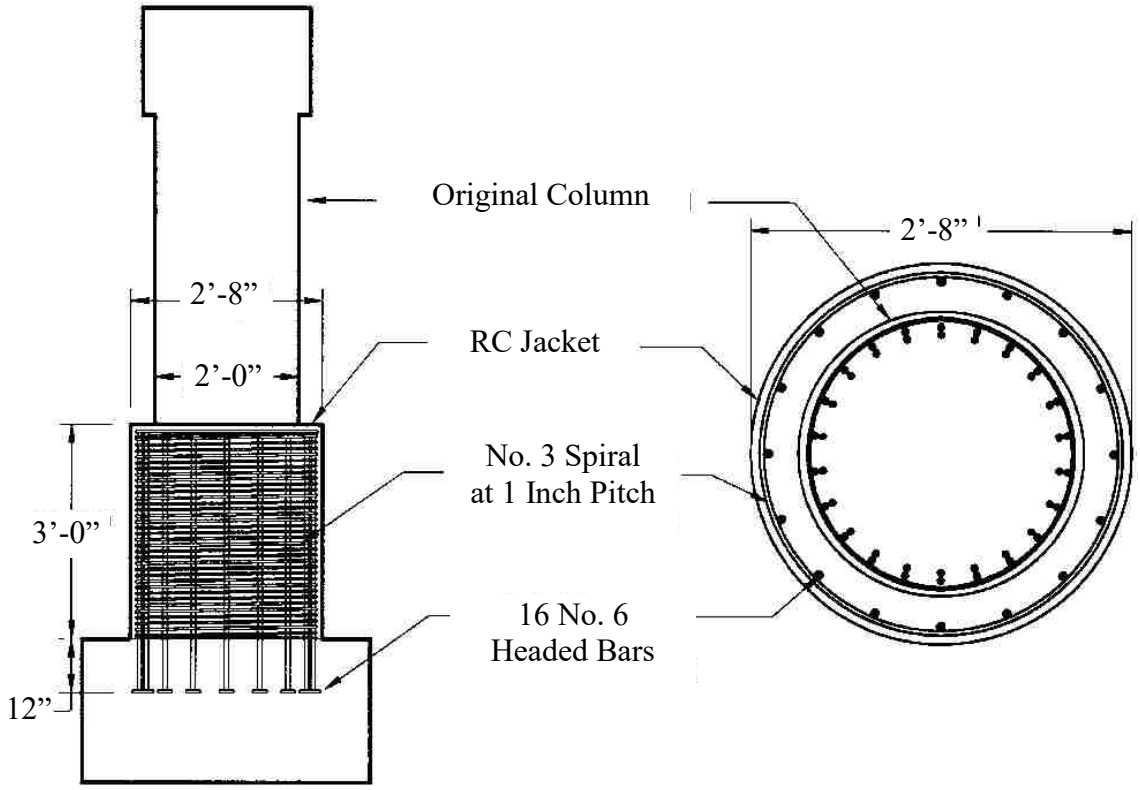


Figure 2.7 - Repair Design for Column 430S (Repaired Designation 430SR) (Lehman, et al., 2001) (1 in. = 25.4 mm)

In the case of 407SR, the strength and deformation capacity exceeded that of the original column (407S). Reaching an applied load of 51 kips (11.4 kN), compared to 39 kips (8.8 kN), and failing during the 7 in. (178 mm) displacement cycles, compared to during the 5 in. (127 mm) displacement cycles. Additionally, the response of this column was compared to that theoretical model developed under the previous study. The predicted the flexural strength was reported to be within 1% of the measured strength, but a comparison of the theoretical and measured response indicates the model under predicted the displacement capacity of the repaired column. This comparison to the theoretical model and to the original column are shown in Figure 2.8.

Both 415SR and 415MR were tested to failure. As this exceeded the loading and damage level encountered by 415M, the results of both 415MR and 415SR were compared to that of column 415S.

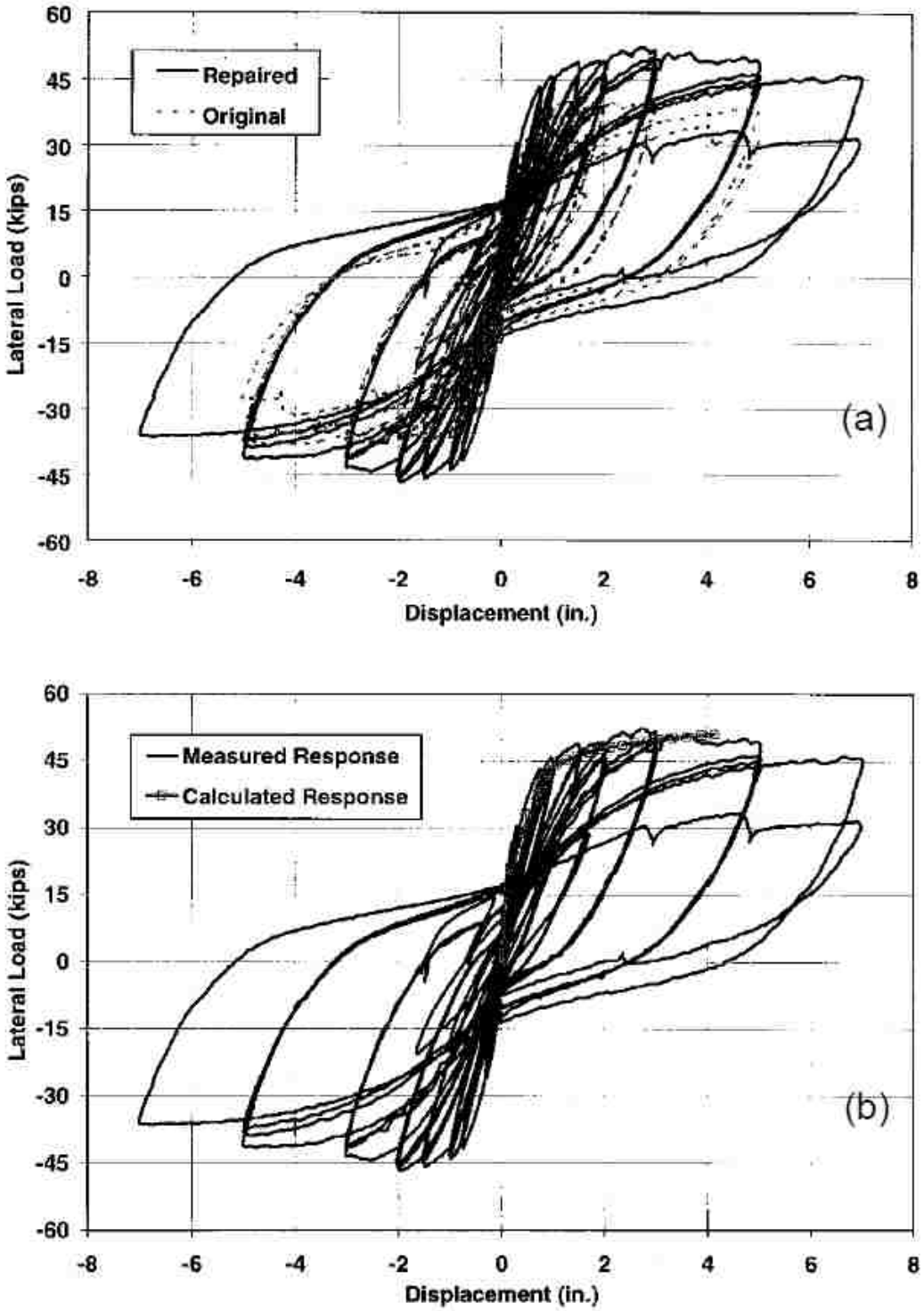


Figure 2.8 - Force-Displacement Response of 407SR Compared to: (a) 407S; and (b) Theoretical Response (Lehman, et al., 2001) (1 kip = 4.448 kN, 1 in. = 25.4 mm)

In the case of column 415SR, the repair design goal was to approximately match the load capacity and move the failure up above the newly placed strong jacket by reducing the flexural capacity at that location. By reducing the distance from the load application point to the flexural failure point, the displacement capacity of the column was expected to be adversely affected. 415SR was also compared to the results of a model, which underpredicted the strength capacity by a reported 7% and over-predicted the maximum displacement by 13%, with a prediction of 5.8 in. (147 mm). In the case of column 415MR, the repaired response was compared to 415S. The response of these two columns was very similar with 415MR providing less resistance to the lower displacement levels. This was attributed to the impacts of cyclic damage to the concrete impacting both the concrete's compressive strength and bond capacity. The paper suggests that the analytical model corrected for this by reducing the nominal compressive strength of the concrete by 50% and assuming a uniform bond capacity of $6\sqrt{f'_c}$ psi ($0.5\sqrt{f'_c}$ MPa). This was reported to bring the strength estimation within 10% of measured and to underestimate the displacement capacity by 12%. However, the comparison of the measured to the calculated response, provided by the paper and shown in Figure 2.10, does not support these numbers; with the plotted values for strength being closer and the apparent displacement capacity being under predicted by more than 42%. It is this author's belief that the presented force-displacement response represents the model prior to the aforementioned modifications. The results of both 415MR and 415SR compared to the results of 415M and 415S, and theoretical results are shown in Figure 2.9 and Figure 2.10, respectively.

Similar to the previous three columns, the response of 430SR was compared to both that of the original column, 430S, and a theoretical response based on a model. The design intent of repair of 430SR, to force flexural failure below the repair jacket, was effectively met with the plastic hinge forming in the lower portion of the jacket. The strength and displacement capacities of the repaired configuration were both diminished, with 430SR never having slightly lower load capacity and failing to complete a full 7 in. (178 mm) displacement cycle. The theoretical model again provided a good prediction of load capacity, with the prediction reported as being within 2% of the measure capacity, but predicted only a 4 in. (102 mm) displacement capacity. It is noted that the model

predicted a displacement capacity of 5in. (127 mm), compared to a measure 7 in. (178 mm) capacity, for column 430S. This indicated the model is capable of capturing the general trend of diminished deformation capacity of the repair column. These results are shown in Figure 2.11.

This work shows three approaches to repairing circular reinforced concrete columns with spiral reinforcement. One being the replacement of concrete and reinforcement in the flexural plastic hinge area, utilizing mechanical couplers, as employed in the repair of 407S. The second repair method being the design and application of a strong jacket which was implemented in two different ways in the repair of columns 415S and 430S. Where 415S was designed to force a flexural failure above the applied repair jacket while 430S was designed to force a flexural failure below the repair jacket. Finally, 415M was repaired with a less invasive repair involving epoxy injection of existing cracks and removal and replacement of loose concrete with a patching material. These repaired columns were then tested to failure and the resulting force-displacement response compared to that of the original column. Furthermore, results were compared to those of an analytical model which summed displacements from discrete sources up to the predicted failure load. While this model proved capable of estimating maximum load resistance, it did not predict the displacement capacity of the columns well and did not model post-peak behavior. Additionally, modification to account for cyclic damage were required for the model of 415MR, but no explanation as to why such modifications were not required for the more severely damaged columns was missing.

**2.1.2.2. Belarbi, Silva, and Bae (2008)**. This study presented the test results of three columns that were cyclically tested under pure torsion, pure bending, and under combined loading with a T/M ratio of 0.2. The column that was tested under combined loading was consequently damaged, and was subsequently repaired using a flowable grout and an external FRP jacket. This retrofitted column was then subjected to the same loading, i.e., with a T/M ratio of 0.2, that caused the initial damage.

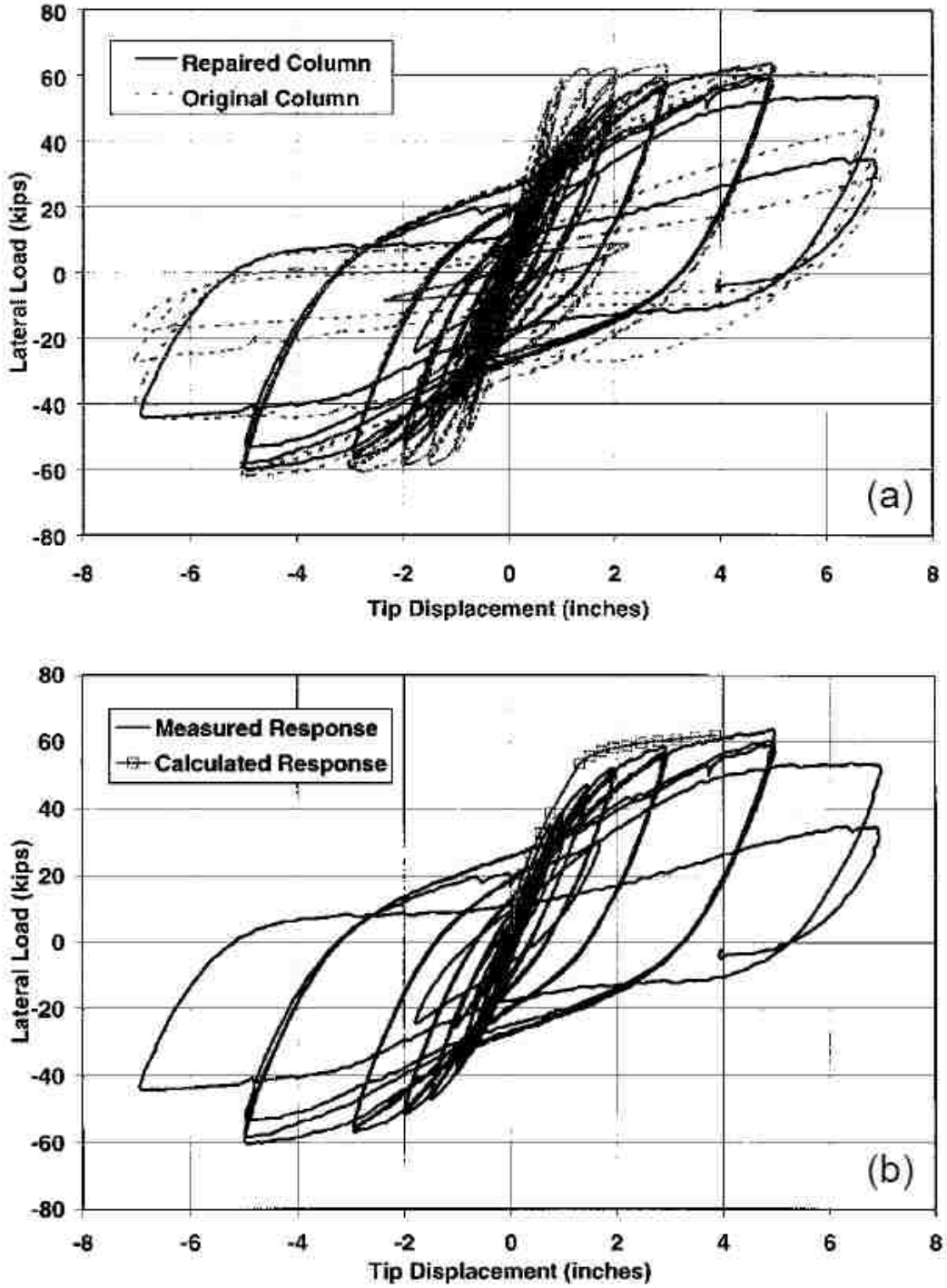


Figure 2.9 - Force-Displacement Response of 415MR Compared to: (a) 415M; and (b) Theoretical Response (Lehman, et al., 2001) (1 kip = 4.448 kN, 1 in. = 25.4 mm)

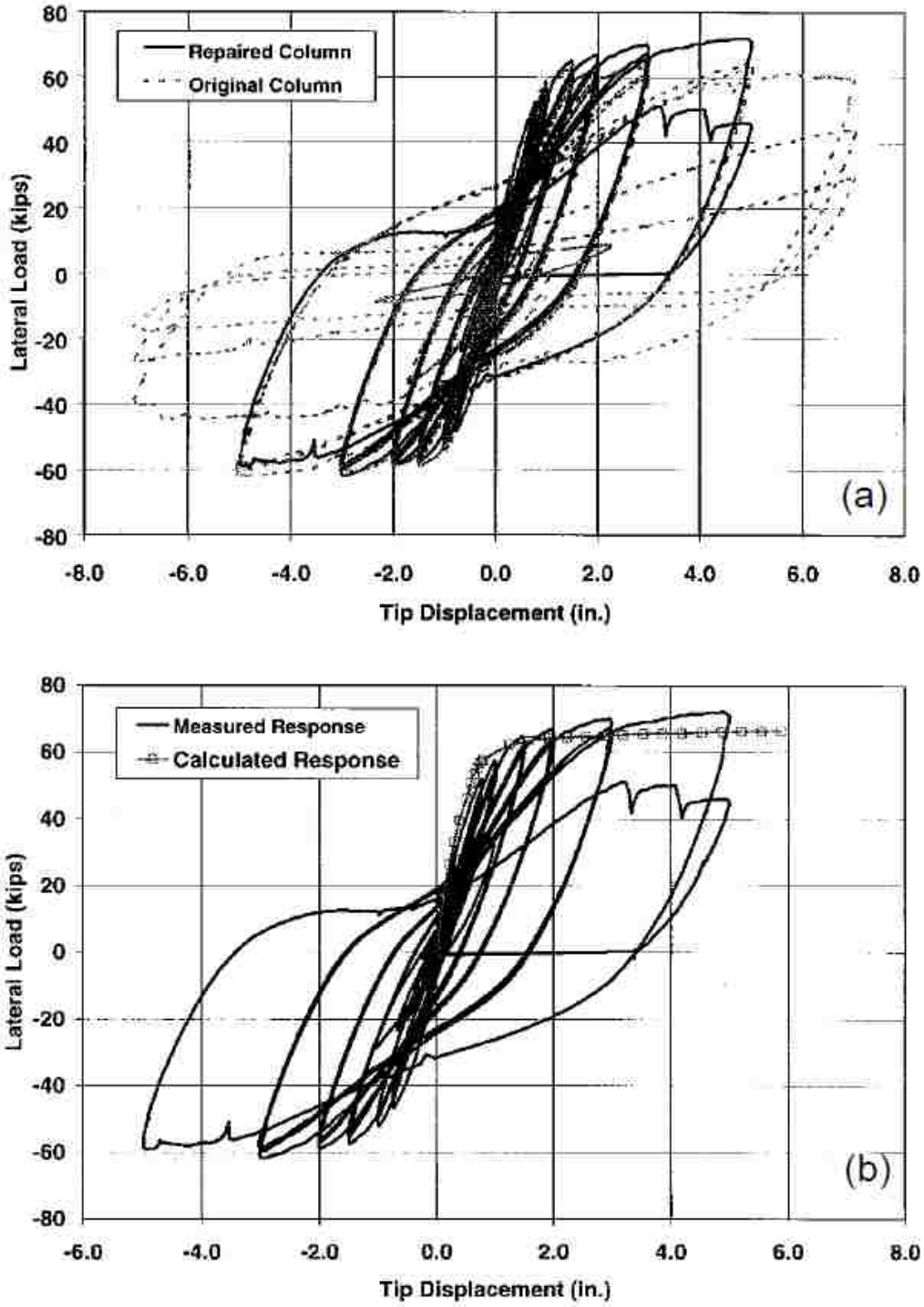


Figure 2.10 - Force-Displacement Response of 415SR Compared to: (a) 415S; and (b) Theoretical Response (Lehman, et al., 2001) (1 kip = 4.448 kN, 1 in. = 25.4 mm)

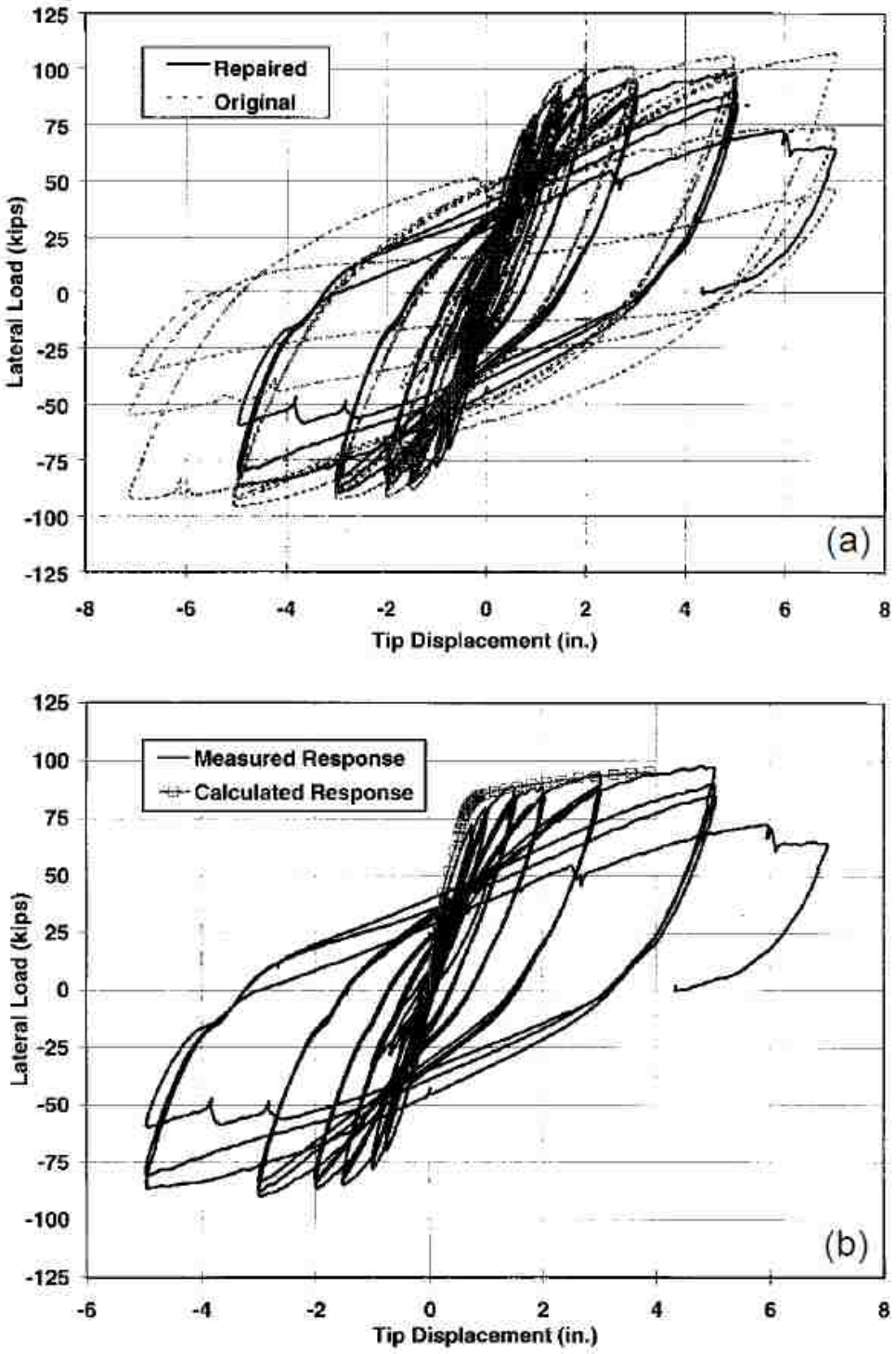


Figure 2.11 - Force-Displacement Response of 430SR Compared to: (a) 430S; and (b) Theoretical Response (Lehman, et al., 2001) (1 kip = 4.448 kN, 1 in. = 25.4 mm)

All four column tests, the three original columns and the repaired column, were loaded initially under force control. This was performed with a single cycle at 25%, 50%, 75%, and 100% of the theoretical first yield, determined via moment-curvature analysis.

For the columns tested under pure bending and a combination of bending and torsion, the force controlled cycles were followed by displacement controlled cycles. These displacement cycles consisted of three cycles at each displacement level, with the same displacement levels being applied in to both columns tested at a torque-to-moment ratio of 0.2. For the column tested under pure torsion the force controlled cycles were followed by displacement controlled cycles at rotation levels increasing at five degree increments.

For the columns tested with an applied lateral load, the pure bending column, the undamaged column tested with a T/M=0.2, and the repaired column tested with a T/M=0.2, the resulting load displacement relationship is plotted in Figure 2.12. In addition, the figure presents the results of a moment curvature analysis, but does not specify which column or loading it corresponds to. The applied torque to resulting twist, for the columns tested under pure torsion, the undamaged column tested with a T/M=0.2, and the repaired column tested with a T/M=0.2, is shown in Figure 2.13. Similar to the previous figure, analytical results are presented without specifying which column or load it pertains to. However, the two figures collectively show the repair's ability to restore the flexural strength and ductility as well as exceed the torsional capacity of the original undamaged column.

**2.1.2.3. He, et al. (2013).** This study tested three RC columns that had been rapidly repaired after sustaining severe damage in a previous study (Prakash, Li, & Belarbi, 2012). The columns were subjected to cyclic lateral loading with varying T/M ratios and a constant axial load. The columns were originally built as 22 in. (560 mm) square columns with four No. 9 (29 mm dia.) reinforcing bars in the each of the corners and eight No. 8 (25 mm dia.) reinforcing bars in the column faces, resulting in a longitudinal reinforcement ratio of 2.13%. Transverse reinforcement was provided by square and octagonal ties, enclosing all of the longitudinal reinforcement, constructed from No. 3 (10 mm dia.) reinforcing bars spaced at 3.25 in. (82 mm).

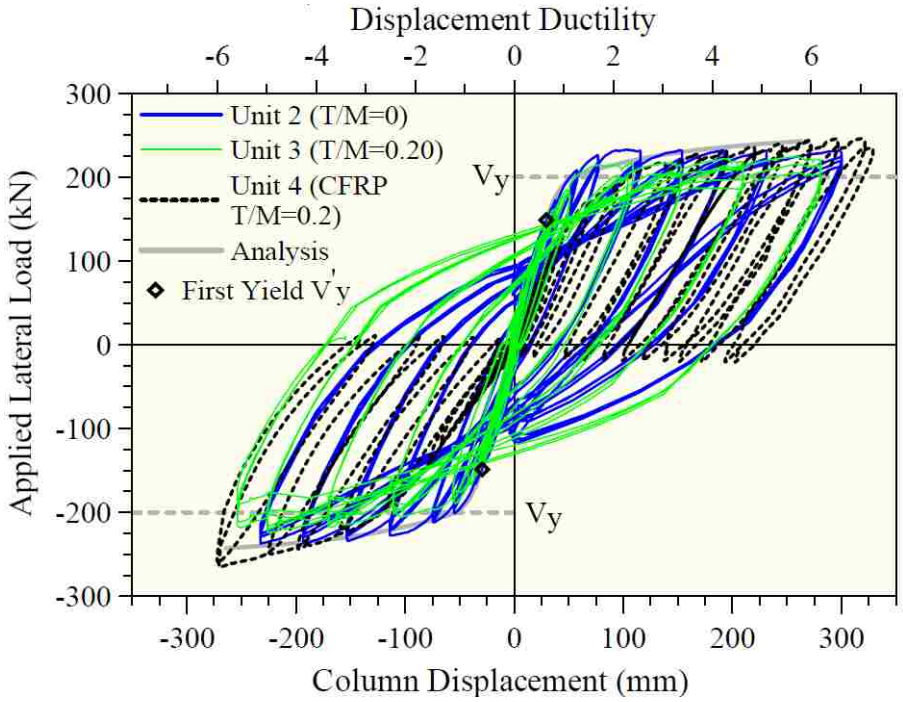


Figure 2.12 - Lateral Load-Displacement Relationship
(Belarbi, et al. 2008) (1 kip = 4.448 kN, 1 in. = 25.4 mm)

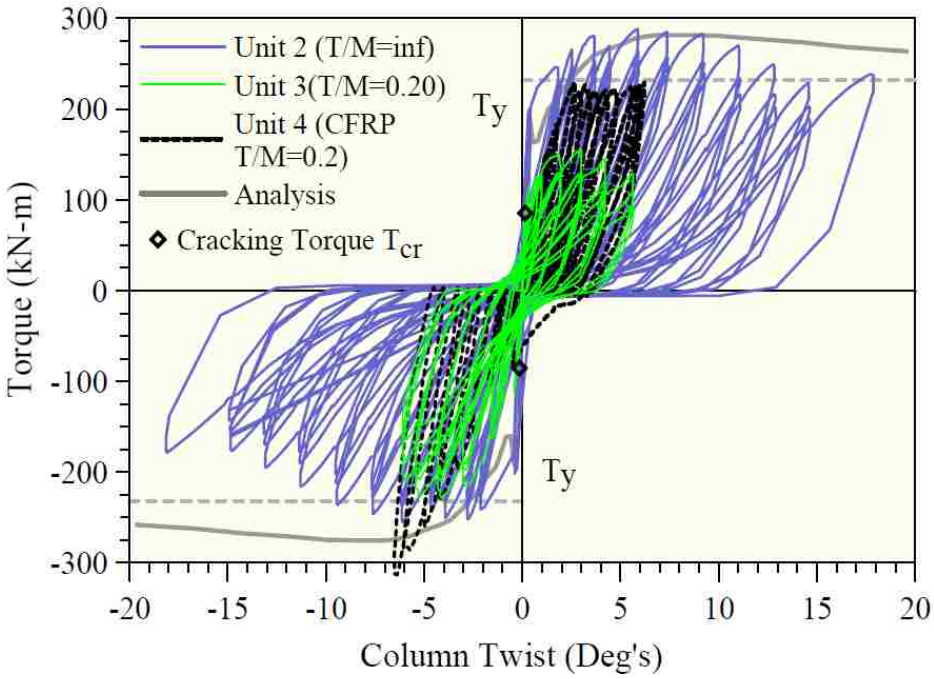


Figure 2.13 - Torque-Twist Relationship
(Belarbi, et al. 2008) (1 kip-ft = 1.356 kN-m)

A volumetric transverse reinforcement ratio of 1.32% was provided by the ties. The reinforcement details of the columns are shown in Figure 2.14. The three columns had been tested previously with a constant axial load of approximately 150 kips (667 kN) under cyclic lateral loading resulting in pure bending (no torsion), bending with torsion with a T/M of 0.2, or bending with torsion at a T/M of 0.4. In each of these columns, damage to the concrete included cracking, spalling of cover, and crushing of the core, as well as yielding and buckling of the longitudinal reinforcement and yielding and end-hook straightening of the transverse reinforcement. In the case of the column subjected to pure bending, two of the No. 9 (29 mm dia.) longitudinal reinforcing bars fractured at the base of the column at opposing corners.

Due to the rapid nature of the repair, the repair materials were selected based on their ability to achieve their required strengths within the timeframe required for the rapid repair. The CFRP, used in the external jacket, consisted of 20 in. (508 mm) wide dry unidirectional carbon fiber sheets with a nominal thickness of 0.0065 in. (0.165 mm) per ply. The following material properties for the CFRP were given by the manufacturer: an ultimate tensile strength of 550 ksi (3800 MPa), an ultimate rupture strain of 16,700 microstrain, and a Young's modulus of 33,000 ksi (227 GPa). A pre-extended micro concrete was selected to replace the damaged and removed concrete. The compressive strength of the repair material was between 5410 psi (37.3 MPa) and 5855 psi (40.4 MPa) at the time of testing.

The repair designs were targeted at restoring ultimate strength only, due to the rapid nature of the repair, noting that in long-term repairs ductility and stiffness should be explicitly considered. The repairs were designed assuming that buckled longitudinal reinforcement could only resist tensile forces, the compressive strength of the repair mortar would be 4000 psi (27.6 MPa) at the time of retesting, and that failure of the FRP anchorage system would not occur. Initially the design of the transverse and longitudinal jacketing was conducted separately, followed by a sectional analysis to finalize the design.

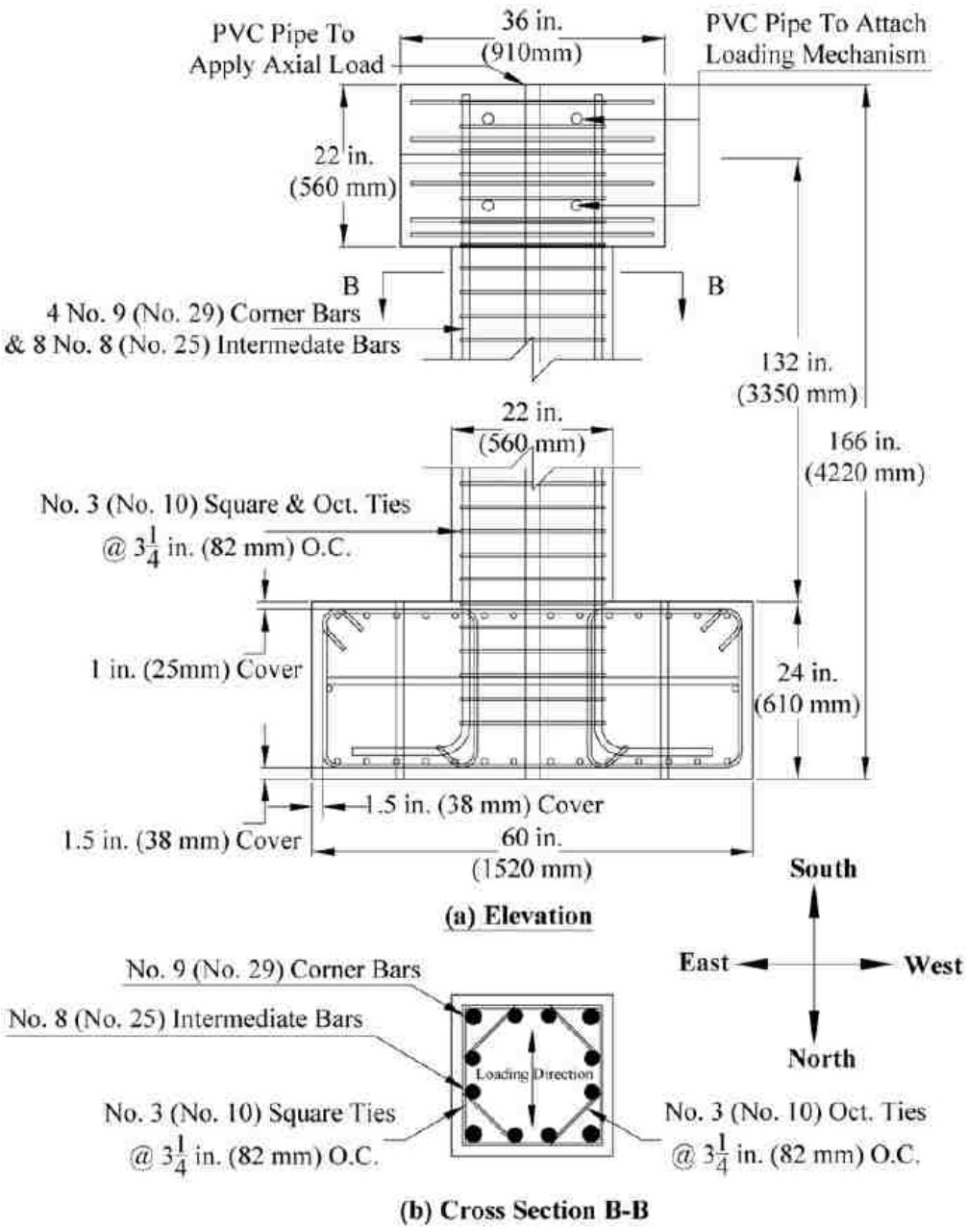


Figure 2.14 - Details of Undamaged Square Columns (He, et al. 2013)

The thickness of the transverse FRP jacket required for shear strength was selected based on the Caltrans criteria for seismic shear design of ductile concrete members (California Department of Transportation, 2006) with an effective strain of 4,000 microstrain, while the thickness required for confinement was determined using a

Caltrans method using a dilating strain of 4,000 microstrain (California Department of Transportation, 2007). The longitudinal reinforcement was designed to meet the yield capacity of the fractured bars and was applied to the extreme tension and compression faces of the column. The subsequent design for the other two columns were modifications of the repair design for the first column and used a space truss model to determine the FRP jacket requirements to resist the additional torsion forces.

Testing of the repaired columns was performed similarly to the original columns, with the initial cycle being performed under force control and the later cycles being performed under displacement control. The repaired columns were tested under the same T/M as they had been tested previously. In the case of the column tested under pure bending, the CFRP jacket came in contact with the anchorage system resulting in rupture of the fibers, and testing was terminated upon audible indication of rupturing of two longitudinal reinforcing bars at a lesser load than that carried by the undamaged column. The problems with the anchorage system detailing were addressed in the other two columns, and they were able to meet the capacity of the original undamaged columns. The testing of the column subjected to a T/M of 0.2 terminated as its capacity began to diminish significantly, while the testing of the column subjected to a T/M of 0.4 terminated due to the rotational limit of the actuator connections being reached. This study demonstrated that FRP jackets can not only be utilized to restore the capacity of severely damaged columns, but do so in a very rapid manner.

## 2.2. ANALYTICAL WORKS

Finite element modeling and analysis is the application of computational mechanics, which is to say it is the implementation of both mathematical models and numerical methods. As such, this section focuses on summarizing the development of analytical and mathematical models that have been used to describe concrete behavior, describing recent studies performed using FEM to investigate concrete behavior, and lastly describing some facets of implementing concrete material models in a modern commercial finite element code, such as Abaqus CAE, that are related to this study.

In recent decades, the implementation of finite element analysis in the research and prediction of RC behavior has increased dramatically. This increase in use of FEA is

spurred on for a variety of reasons, among which is the rapid advancement in computer technology, that has allowed both increased availability and increased computing capacity as hardware has become both cheaper and more powerful. This availability of cheap computing power is the catalyst for the progression of the FEM as the formulation of the element stiffness matrices, the solving of equations, the evaluation of mode shapes, and the evaluation of mode frequencies are all computationally intensive (Wilson, 2008). The result of this progress in computational capacity is an equally impressive growth in both size and complexity of simulations. The resulting body of knowledge is too large to overview here; instead the remainder of this section will summarize the analytical models that have contributed the development of numerical methods for concrete, key facets of implementing concrete into a finite element model in modern commercial finite element software, and works most closely related to the present study.

**2.2.1. Drucker-Prager Yield Criterion.** The Drucker-Prager yield criterion was developed as a pressure dependent failure surface for soils and granular material (Drucker & Prager, 1952). It is formulated on the basis of there being a linear relationship between the first stress invariant and the square root of the first deviatoric stress invariant. The first deviatoric stress invariant is the first stress invariant minus three times the hydrostatic pressure. This results in a yield surface resembling a smoothed version of the Mohr-Coulomb yield surface.

The Drucker-Prager yield criterion differs from non-pressure dependent yield criteria, such as Von-Misses' or Tresca's, in its capacity to capture shear strength increases with increasing levels of hydrostatic pressure, a unique property of concrete and other granular materials (Yu, Teng, Wong, & Dong, 2010).

**2.2.2. Compression Field Theory.** The compression field theory, referred to as CFT, was formally presented by Collins in 1978 (Collins, 1978). However, a version of CFT was presented by Collins and Mitchell in 1974 in which a "diagonal compression field theory" was applied to describe the behavior of symmetric reinforced concrete members subjected to pure torsion (Mitchell & Collins, 1974). This model assumes that concrete does not have sufficient tensile capacity to prevent the concrete cover from spalling off the core at higher torsional moments. As a result, the model assumes that all

shear flow occurs within the concrete core, which is bounded by the centerline of the transverse reinforcement.

CFT uses an equivalent stress block derived from the parabolic stress-strain distribution, proposed by Hognestad (Hognestad, 1951), to describe the behavior of concrete in compression. Concrete compression struts are assumed to be placed at an angle, α, relative the cross section, resulting in both a shear flow and compression about the cross-section. The magnitude of the force in the compression strut is a result of the applied torsional moment, and is averaged, or smeared, across the geometry. The resulting axial forces that the compression struts provide are resisted by the longitudinal reinforcement, which provides a tensile force.

**2.2.3. Modified Compression Field Theory.** The modified compression field theory, referred to as MCFT, was developed at the University of Toronto as part of an experimental program that included the testing of 30 reinforced concrete panels subjected to in-plane shear and axial loads (Vecchio & Collins, 1986). It is a simple analytical model for predicting the load-deformation response of RC elements subject to in-plane shear and normal forces and has formed the basis for several finite element models, such as secant-stiffness based formulation by Vecchio in 1989 (Vecchio, 1989). That model was improved upon to create the analysis program known as TRIX by Vecchio in 1990 to include initial strains in materials. The program TRIX was later used by Vecchio to account for the lateral expansion of concrete perpendicular to the principal compression forces, in order to account for expansion and confinement, leading to improved simulation of shear walls (Vecchio, 1992). The experimental basis was provided by (Lefas, 1990), who tested a total of 13 walls with two geometric configurations, those with a height-to-width ratio of 1.0 and 2.0, under varying axial load conditions, and with a monotonically increasing lateral load. Those shear walls that possessed a height-to-width ratio of 1.0 were denoted as SW11 thru SW17, and those with a height-to-width ratio of 2.0 were denoted as SW21 thru SW26. The use of TRIX yielded the results in Figure 2.15 that shows the simulated, denoted as “Theoretical”, load response compared to experimental results, for a shear wall with a height-to-width ratio of 1.0 (SW16) and a height-to-width ratio of 2.0 (SW25), as obtained by (Lefas, 1990).

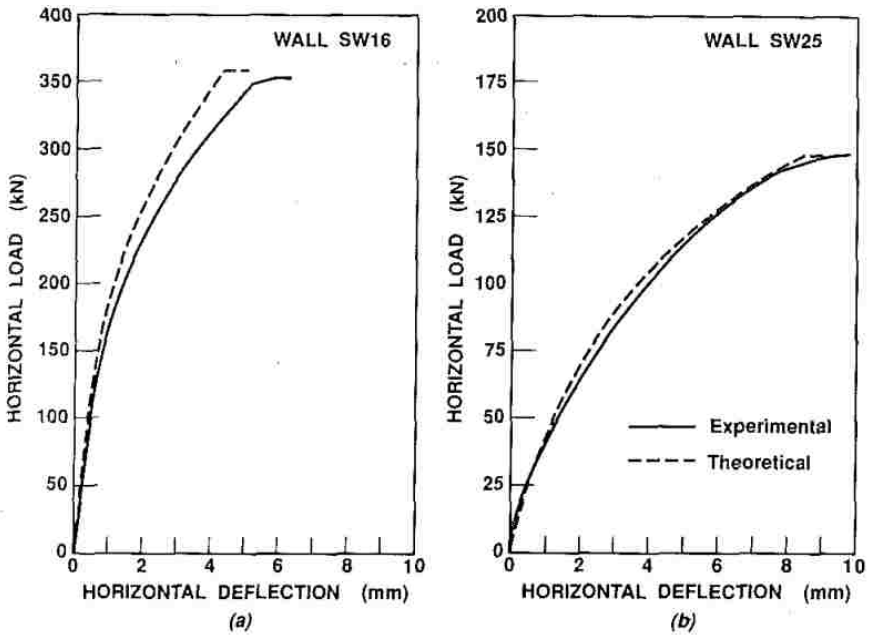


Figure 2.15 - Comparison of Experimental and Numerical Load-Deformation Response of Shear Walls using TRIX (Vecchio, 1992) (1 kip = 4.448 kN, 1 in. = 25.4 mm)

**2.2.4. Lee and Fenves (1998).** In 1998, Lee and Fenves proposed a modification to the model for concrete developed by Lubliner, et al. (1989), known as the Barcelona model. In the Barcelona model, a fracture energy based scalar damage variable is used to account for all damage states, and elastic and plastic degradation values are used to account for diminishing stiffness (Lubliner, et al., 1989). In this model, the yield function is a function of both the effective stress and damage variables, the generic form of which is shown in Equation 1, where $\bar{\sigma}$ represents the effective stress, and $\kappa$ represents the damage variables.

$$F(\bar{\sigma}, \kappa) \leq 0 \qquad \text{(Eq. 1)}$$

Using this definition of the yield function, where *F* is an isotropic scalar function with multiple hardening evolution, the plastic-damage model can be written as equations 2a, 2b, and 2c that are subjected to the Kuhn-Tucker complimentary conditions, such that

$\dot{\lambda} \geq 0;\ \dot{\lambda}F = 0; and\ \dot{\lambda}\dot{F} = 0$, where $\dot{\lambda}$ is a positive plastic multiplier. Within the plastic-damage models the strain tensor is represented by $\varepsilon$, and the plastic portion of the strain tensor is represented by $\varepsilon^p$.

$$\overline{\sigma} = \mathrm{E}_0 : (\varepsilon - \varepsilon^{\mathrm{p}}) \in \{\overline{\sigma} | \mathrm{F}(\overline{\sigma}, \kappa) \leq 0\} \quad \text{(Eq. 2a)}$$

$$\dot{\varepsilon}^{\mathrm{p}} = \dot{\lambda} \nabla_{\sigma} \Phi(\overline{\sigma}) \quad \text{(Eq. 2b)}$$

$$\dot{\kappa} = \dot{\lambda} \mathrm{H}(\overline{\sigma}, \kappa) \quad \text{(Eq. 2c)}$$

The total stress can then be evaluated using the relationship in Equation 3.

$$\sigma = [1 - \mathrm{D}(\kappa)]\overline{\sigma} \quad \text{(Eq. 3)}$$

In Equation 3 the term $D(\kappa)$, representing the stiffness degradation variable, is subject to $0 \leq D(\kappa) < 1$ and is determined using $D(\kappa) = 1 - (1 - D_t)(1 - D_c)$, where $D_t$ and $D_c$ are the tensile and compressive damage parameters, respectively. This differs from the Barcelona model in which a single scalar damage variable was implemented. The addition of a second scalar damage parameter makes the model appropriate for simulating the cyclic behavior of concrete.

The model goes on to derive a damage evolution equation for a uniaxial case, $\dot{\kappa}_x$, in terms of specific fracture energy, a function of the uniaxial damage variable, and the scalar plastic strain rate. The scalar plastic strain rate is evaluated in the three-dimensional case to derive a damage evolution equation in the multidimensional case, given by Equation 4a, where $\delta$ is the Kronecker delta, $\dot{\varepsilon}^{\hat{p}}_{max}$ and $\dot{\varepsilon}^{\hat{p}}_{min}$ are the maximum and minimum eigenvalues of the plastic strain tensor, and $r(\hat{\sigma})$ is a weight function. The weight function $r(\hat{\sigma})$ is a function equal to zero if $\hat{\sigma} = 0$, else is it defined by Equation 4b.

$$\dot{\varepsilon}^{p} = \delta_{tN} r(\hat{\sigma}) \dot{\varepsilon}^{\hat{p}}_{max} + \delta_{cN}(1 - r(\hat{\sigma})) \dot{\varepsilon}^{\hat{p}}_{min} \quad \text{(Eq. 4a)}$$

$$r(\hat{\sigma}) = \frac{(\sum_{i=1}^{3}\langle\hat{\sigma}\rangle)}{(\sum_{i=1}^{3}|\hat{\sigma}|)} \quad \text{(Eq. 4b)}$$

Similar to the Barcelona model, the model proposed by Lee and Fenves implements cohesion parameters to make the yield surface more realistic for concrete materials. In the model, cohesion is accounted for by making the yield surface a function of the largest principal stress, resulting in different behavior under compression and tension. The implemented yield function takes the form shown in Equation 5, where $\alpha$ and $\beta$ are dimensionless constants, $\hat{\sigma}_{max}$ is the algebraic maximum principal stress, and $c_c$ is the compressive cohesion stress.

$$F(\sigma,\kappa) = \frac{1}{1-\alpha}\left[\alpha I_1 + \sqrt{3J_2} + \beta(\kappa)\langle\hat{\sigma}_{max}\rangle\right] - c_c(\kappa) \quad \text{(Eq. 5)}$$

The yield surface in the plane stress space generated by this yield function is shown in Figure 2.16.

Since the model's yield function is essentially a Drucker-Prager type (discussed in Section 2.2.1), being that the yield surface is dependent on the first stress invariant, Lee and Fenves implemented a Drucker-Prager type plastic potential function. Equation 6 shows the plastic potential function of the Lee and Fenves model.

$$\Phi = \sqrt{2J_2} + \alpha_p I_1 \quad \text{(Eq. 6a)}$$

$$\Phi = \|s\| + \alpha_p I_1 \quad \text{(Eq. 6b)}$$

where $\|s\|$ indicates the norm of the deviatoric stress.

The model was then implemented into a finite element framework to replicate the results of several experimental studies with generally good results. A single element model was used to simulate monotonic uniaxial tension and compression of concrete; the results were then compared to the experimental works of Gopalaratnam and Shah (1985)

and Karsan and Jirsa (1969). These showed good agreement, but the tensile softening curve was not as concave as recorded in the experimental studies. Later in the paper a mesh sensitivity study was performed for the tensile case, and the softening curve became markedly more concave with improved mesh refinement. Unfortunately, a direct comparison of the refined mesh to the experimental study was not presented, nor was a measure of error presented.

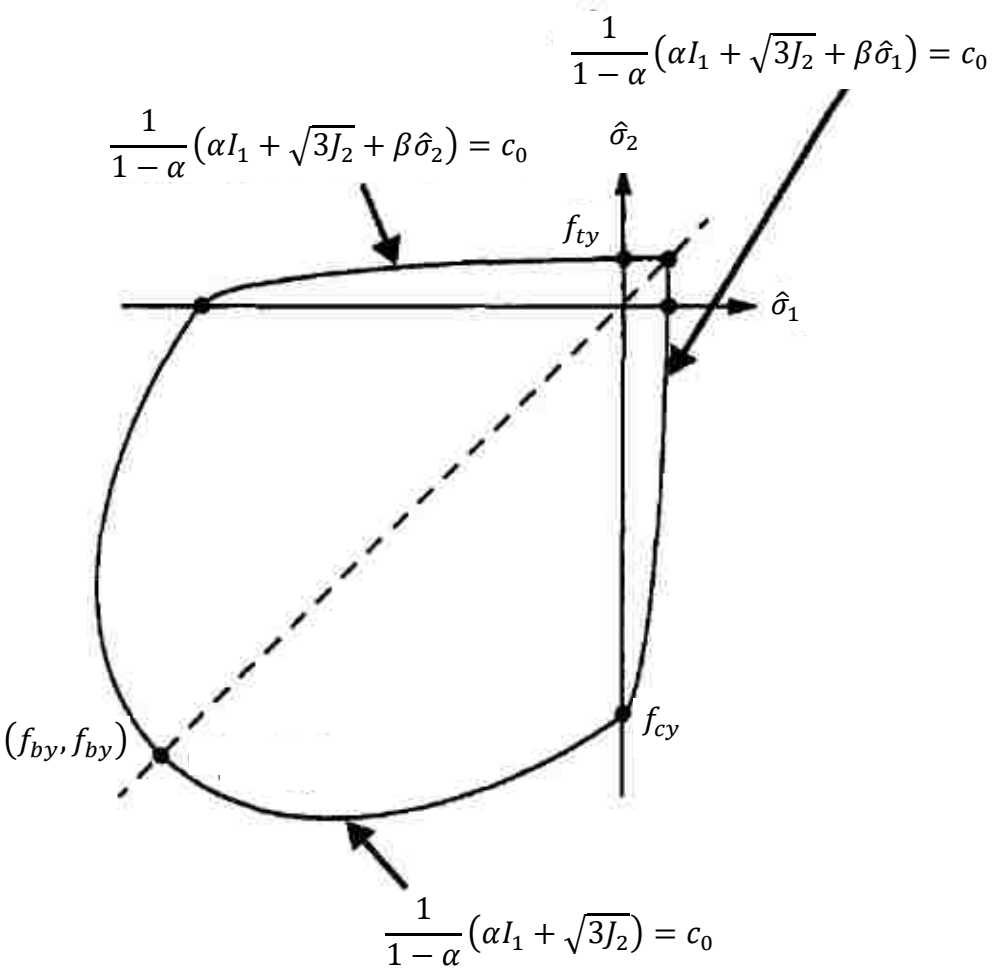


Figure 2.16 - Yield Function in Plane Stress Space (Lubliner, et al. 1989)

In addition to the uniaxial cases, biaxial tension and biaxial compression simulations were performed. The later was shown to provide a good agreement with the

experimental work of Kupfer, Hilsdorf, and Rusch (1969). In addition to monotonic loading, cyclic loadings were simulated for pure tension, pure compression, and tension-compression; the results of these simulations were compared to the experimental works of Gopalaratnam and Shah (1985), Karsan and Jirsa (1969), and Reinhardt (1984), respectively. Again, a single element model was used, and the softening curve for the pure tensile case was less concave than the experimental study. In general, the cyclic simulations showed good agreement, though the model does not exhibit softening before peak load of subsequent cycles, similar to the phenomena known as the Bauschinger effect.

## 2.3. FINITE ELEMENT WORKS

As the body of work involving the finite element analysis of concrete and concrete structural members is too vast to summarize here, and is beyond the scope of this work, this section instead focuses on summarizing selected works that are most related to the present study. Similarly, there exist many commercial finite element codes that can be implemented in the finite element analysis of concrete structural elements (Johnson, 2006). As this study was performed using Abaqus CAE, the primarily focus is on studies that have used the Abaqus code for their framework. Of particular interest is those studies that explore the behavior of concrete structural elements under combined loading, studies that include provisions for passive confinement of concrete, or those that examine the behavior of FRP strengthened concrete structural elements. Furthermore, this section summarizes some proposed constitutive models for modeling concrete behavior under multi-axial stress states.

**2.3.1. Han, Yao, and Tao (2007).** Han, Yao, and Tao presented a pair of papers in 2007 on the behavior of concrete-filled steel tubes under pure torsion (Han, Yao, & Tao, 2007) and combined loadings (Han, Yao, & Tao, 2007) including compression-torsion, bending-torsion, and compression-bending-torsion. These papers present a finite element study that was developed to predict the behavior of both circular and square shaped concrete-filled steel tubes (CFST) and a set of simplified models to predict the ultimate strength of these types of members.

The finite element model was developed in the commercial code Abaqus CAE using the preexisting damaged plasticity model, in which the optional fracture energy based formulation for the tensile softening behavior, based on the work of Hillerborg, et al. (1976), was selected to represent the concrete.

The results of this finite element analysis were compared to the published works of Gong (1989), Zhou (1990), Xu, et al. (1991), Han and Zhong ST (1995), and Beck and Kiyomiya (2003). Once the validity of the model was established, a series of parametric studies was performed to determine the relationship between member strength and key parameters.

In many ways, the analysis of CFST is similar to the analysis of concrete members strengthened or repaired with external FRP jacketing. In both cases either the steel tube or the FRP jacket act as a passive confining system that increases both the compressive strength and ductility of the member. The resulting behavior is similar to the point where ACI Committee 440 recommends using Mander's model, which was originally developed for members confined by steel jackets, to analyze the apparent concrete strength and maximum usable compressive strain in circular concrete members with FRP jacketing (ACI 440, 2002).

**2.3.2. Prakash, Belarbi, and You (2010).** Prakash et al. tested a series of eight circular columns with varying height-to-depth ratios under combined loading. Four columns with a height-to-depth ratio of 6 and four with a ratio of 3 were constructed and tested cyclically with vary ratios of torque to moment with a constant applied axial load. In each height-to-depth ratio a column was tested with a T/M of 0.0 (pure bending), infinity (pure torsion), 0.2, and 0.4. All columns were 24 in. (610 mm) in diameter and constructed with twelve 1.0 in. (25 mm) diameter longitudinal reinforcing bars, resulting in a longitudinal reinforcing ratio of 2.10%, and spiral transverse reinforcement in varying ratios. The columns with a height-to-depth ratio of 6 tested under pure torsion and pure bending were constructed with a spiral reinforcement ratio of 0.73%, and the remaining columns were constructed to with a spiral reinforcement ratio of 1.32%. Testing was conducted under load control, at intervals of 25%, 50%, 75%, and 100% of anticipated yield strength, until yielding of the first longitudinal bar, unless tested under pure torsion when load control was performed until yielding of the first spiral, denoted as

$\mu_\Delta$=1 and $\mu_\theta$=1, respectively. After initial yielding of the reinforcement was observed, loading continued cyclically under displacement control, with three cycles at each displacement interval.

In addition to the experimental program, the study presented a three-dimensional nonlinear finite element analysis performed using the commercial code DIANA. A linear 8 node solid brick element, denoted as HX24L in DIANA, was implemented to represent the concrete material as well as a linear elastic 'rigid' material used to represent the cap and base. Additionally, bar elements representing the steel were embedded within the solid 'parent' elements. The model setup is shown graphically in Figure 2.17 and suggests that the spiral transverse reinforcement was simplified to be represented by circular reinforcing rings. The Newton-Raphson method was implemented to obtain a solution with a maximum of twenty iterations using force and displacement fields, with values of 0.01 lbs. (0.045 N) and 0.01 in. (0.254 mm) respectively, as convergence and stopping criteria.

A total of 12 analysis cases were tested with this model setup, with all but six of those cases being experimentally tested as part of the study, as outlined in Table 2.2. For those cases analyzed under pure bending, the model was run under displacement control at increments of 0.24 in. (6 mm) until 5.9 in. (150 mm), and results correlated well during the elastic responses to the experimental data. This is short of the 17.7 in. (450 mm) experienced during the experimental portion of the study, however, due to issues with convergence. Similar to the experimental results, the finite element model showed a marginal increase in capacity when the transverse reinforcement ration was increased from 0.73% to 1.32%.

The finite element models under pure torsion were loaded similarly, being loaded at 0.24 in. (6 mm) intervals with equal and opposite displacements being applied to each load point. These pure torsion cases showed generally good agreement with experimental results, but had a reduced initial stiffness and did not exhibit asymmetric response due to the locking and unlocking effect. The paper notes this lack of asymmetric behavior as being due to a neglect of the confinement effect present during locking. However, if the graphical representation of the model presented in the paper,

shown in Figure 2.17, is accurate, then this lack of asymmetric behavior could also be due to the simplification of the reinforcement.

In the load cases that included combined loads, including bending, shear, and torsion, the finite element response was generally stiffer but predicted the overall behavior reasonably well; except in the case of the column tested with a high T/M of 0.4 and ratio of transverse reinforcement of 0.73%. This specimen failed suddenly and prematurely due to the complex internal load distributions post-cracking.

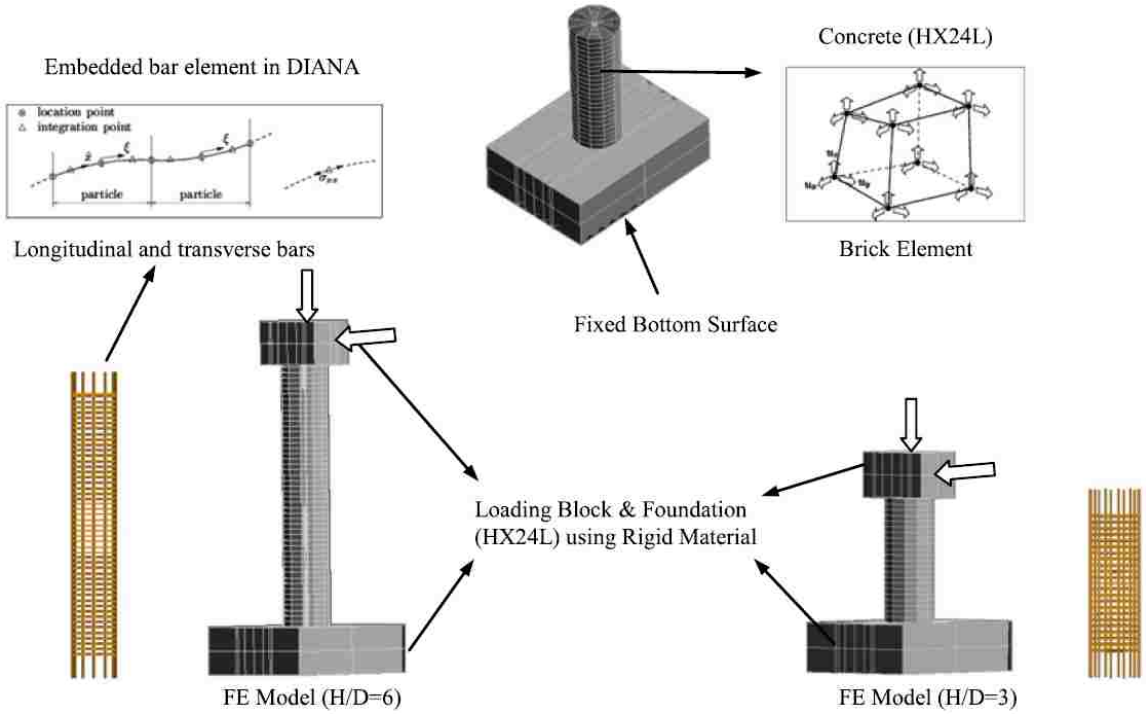


Figure 2.17 - Finite Element Model Setup (Prakash, Belarbi, & You, 2010)

The paper goes on to present von Mises stress distributions on the column surfaces and through mid-section, cut parallel to the primary loading direction, and compares these stress distributions to photographs of the damage for the load cases that were validated with experimental results. Locations where these stress distributions were concentrated tended to correspond to the locations of spalled and crushed concrete in the images of the experimental results.

Table 2.2 - Analysis Cases for Finite Element Model (Prakash, Belarbi, & You, 2010)

| Analysis Cases | Height/Depth Ratio | Torque/Moment Ratio | Transverse Reinforcement (%) | Experimentally Tested (Y/N) |
|---|---|---|---|---|
| 1 | 3 | 0 (Pure Bending) | 0.73 | N |
| 2 | 3 | 0.4 | 0.73 | N |
| 3 | 3 | ∞ (Pure Torsion) | 0.73 | N |
| 4 | 3 | 0 (Pure Bending) | 1.32 | Y |
| 5 | 3 | 0.4 | 1.32 | Y |
| 6 | 3 | ∞ (Pure Torsion) | 1.32 | Y |
| 7 | 6 | 0 (Pure Bending) | 0.73 | Y |
| 8 | 6 | 0.4 | 0.73 | N* |
| 9 | 6 | ∞ (Pure Torsion) | 0.73 | Y |
| 10 | 6 | 0 (Pure Bending) | 1.32 | N |
| 11 | 6 | 0.4 | 1.32 | Y |
| 12 | 6 | ∞ (Pure Torsion) | 1.32 | N |

* (Prakash, Belarbi, & You, 2010) states both FE and experimental results exist for this case, but it is not included in the experimental test matrix or description.

# 3. EXPERIMENTAL PROGRAM

## 3.1. EXPERIMENTAL PROGRAM OVERVIEW

This section summarizes the most relevant points of the experimental program, for which the test results served as the basis for validation and comparison of the finite element model developed in this study (discussed in Section 4). A complete description of the experimental program is included in the Ph.D. dissertations by Li (2012) and Yang (2014). However, a description of the specimen construction, test procedure, and results are provided in this section in order to provide context and justification for the setup of the material model and to provide a benchmark for the validation of the simulation results.

The experimental program consisted of essentially two parts. The first part consisted of the construction and testing of the original undamaged columns, performed in a previous study (Li, 2012). These results were used to develop the initial finite element model discussed in Section 4. The second part of the experimental program consisted of repairing and retesting the columns from the first part of the study (Yang, 2014). The initial model was modified in an attempt to simulate these repaired columns through the alteration of existing material models and the edition of shell body representing the FRP jacketing used with the repair. Due to numerical stability issues, convergence of the modified finite element model could not be obtained for the repaired columns, as discussed in Section 4.

## 3.2. OBJECTIVES

The first part of the experimental program sought to examine the behavior of oval shaped RC columns with interlocking spirals under a constant axial load and cyclic combined loading, including torsional moment, bending moment, and shear (Li, 2012). Six columns were included in the first part of the experimental program. For the purpose of this investigation, test results of three specimens selected from the first part of experimental program are intended to provide a benchmark for the development and validity of the finite element model described in this thesis.

The second part of the experimental program sought to examine the effectiveness of techniques developed to repair three of the six severely-damaged columns when subjected to the same loading conditions (Yang, 2014). As discussed in Section 3.3, two columns were repaired using the same repair procedure, while the third column was repaired using a different procedure. For the purpose of this investigation, test results of the two specimens from the second part of the experimental program with the same repair procedure are used to examine the flexibility of the model to include and account for the repair system employed.

### 3.3. TEST MATRIX

This investigation examines the behavior of the three columns from the first part of the experimental program (Li, 2012) that were repaired and used in the second part (Yang, 2014), the construction of which is detailed in Section 2.1.1.2. The columns are referred to as Calt-1, Calt-2, and Calt-3 in this thesis for consistency with the naming used in (Yang, 2014). These three columns were nominally the same and tested under different torsional moment-to-bending moment ratios of 0.2, 0.6, and 0.2 respectively, with all but Calt-3 being oriented such that the primary bending force was along the weak axis, as shown in Figure 3.1. Calt-3 was instead oriented such that the principal bending occurred 35° off the strong axis, as shown in Figure 3.2, which resulted in biaxial bending.

The repaired columns are referred to as R-Calt-1, R-Calt-2, and R-Calt-3 for consistency with the naming used in (Yang, 2014). Columns R-Calt-1 and R-Calt-2 were repaired using a similar procedure. The repair procedure included removal of longitudinal bar segments and sections of the spiral ties within the plastic hinge region. The removed sections of longitudinal reinforcing bar were replaced with new reinforcing bar segments that were attached to the adjacent segments of original reinforcement by means of mechanical couplers. After replacing the concrete in the plastic hinge region, an externally bonded CFRP jacket was installed in order to restore the shear and torsional strength that had previously been provided by the section of spiral ties that had been removed. Columns R-Calt-1 and R-Calt-2 were tested under the same protocol as before they were repaired (Yang, 2014) (Yang, et al., 2015).

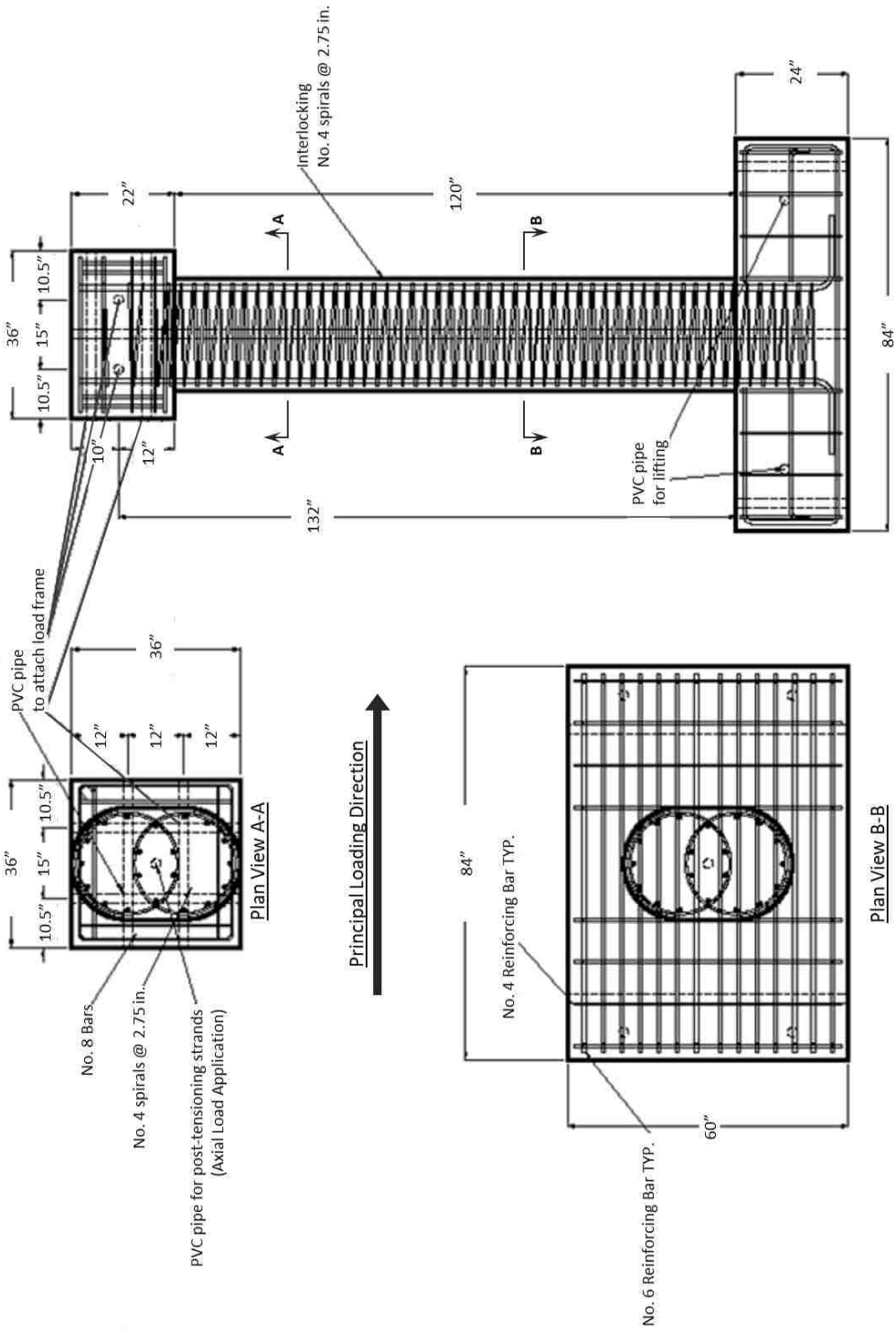


Figure 3.1 - Geometry and Reinforcement Details of Calt-1 and Calt-2 (1 in. = 25.4 mm)

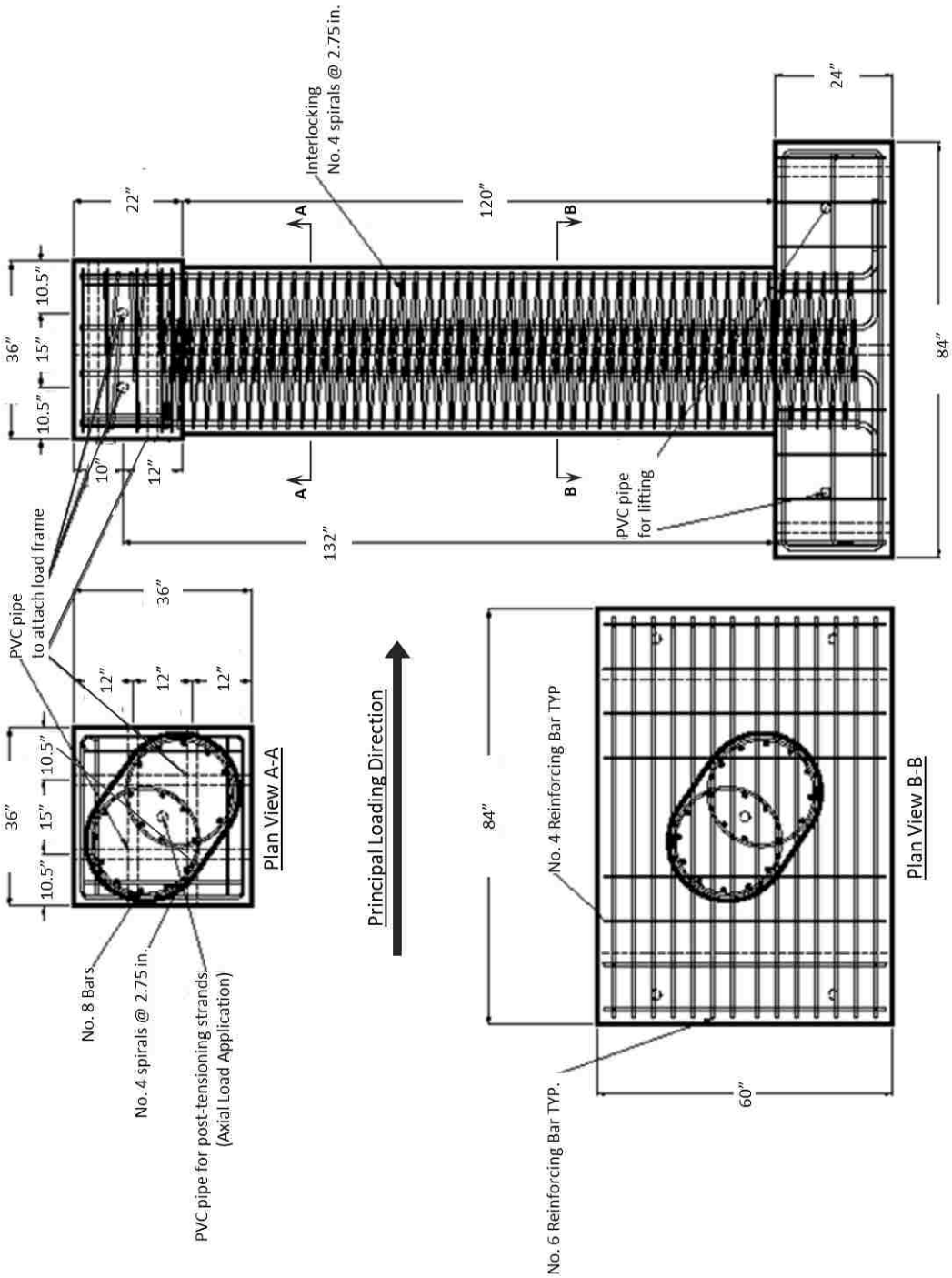


Figure 3.2 - Geometry and Reinforcement Details of Calt-3 (1 in. = 25.4 mm)

It should be noted that R-Calt-3 was also repaired and retested (Yang, 2014) (Yang, et al., 2015), but due to its novel repair system it is considered outside the scope of any future work based upon the model developed for this study. A summary of test matrix is presented in Table 3.1.

Table 3.1 - Test Matrix for Experimental Study

| Study | Specimen ID | T/M | Orientation of Weak Axis | Bar Splice | FRP Jacket |
|---|---|---|---|---|---|
| 1[1] | Calt-1 | 0.2 | 0° | N/A | N/A |
| | Calt-2 | 0.6 | 0° | N/A | N/A |
| | Calt-3 | 0.2 | 35° | N/A | N/A |
| 2[2] | Calt-1R | 0.2 | 0° | Sleeve anchors | Unidirectional |
| | Calt-2R | 0.6 | 0° | Swaged anchors | Unidirectional |
| | Calt-3R | 0.2 | 35° | None | Bidirectional |

1. Li (2012)
2. Yang (2014)

### 3.4. TEST SETUP

The testing of both the undamaged and repaired columns took place at the Missouri S&T Structural Engineering Research Laboratory (SERL). The tests were conducted adjacent to the SERL's strong wall, which served as a reaction for the applied lateral load. The footing of the column was placed between two concrete chairs. These chairs were spaced far enough apart to allow for prestressing cables, used to apply axial load, passing through the column along the longitudinal axis and anchored beneath the column footing. Hydro-stone was placed between the column footing and the chairs in order to provide a more uniform bearing surface. Next, a pair of wide-flange steel beams

was placed across the footing and chairs on either side of the column. These beams were in turn held in place by steel beams, comprised of two steel channels welded back to back with a ~1 in. (25 mm) space between them, that were placed perpendicular to the wide flange beams and anchored to the strong floor using prestressed Dywidag bars. Together the steel beams, the reinforced concrete chairs, and the Dywidag anchors were intended to provide a fixed condition for the column footing.

Transverse (lateral) loading was applied to the cap of the columns by means of two actuators. The actuators were both manufactured by MTS, and are models 243.45T and 243.7T. The 243.45T actuator has a total stroke of 20 in. (508 mm.) and a load capacity of 650 kN in compression and 445 kN in tension, while the 243.7T has a total stroke of 28 in. (712 mm) with a load capacity of 1460 kN in compression and 961 kN in tension. These actuators were controlled in a closed-loop system using the FlexTest GT digital controller system manufactured by MTS and were connected to the SERL's strong wall and to steel jigging. The jigging was attached to the column cap by multiple prestressed Dywidag bars and allowed the actuators to attach in line with the faces of the column cap, 36 in. (914 mm) on center and 131 in. (3327 mm) from the top of the footing. The test setup and lateral loading are shown in Figure 3.3.

Equations 7, 8, and 9 provide the base shear ($V_{base}$), the bending moment (M), and the torsional moment (T) applied by the two actuator loads ($P_1$ and $P_2$):

$$V_{base} = P_1 + P_2 \quad \text{(Eq. 7)}$$

$$M = (V_{base})*H \quad \text{(Eq. 8)}$$

$$T = (P1 - P2)*\frac{d}{2} \quad \text{(Eq. 9)}$$

Where d is the on center spacing, 36 in. (914 mm), and H is the distance from the top of the footing to the elevation at which the load is applied, 131 in. (3327 mm).

Similarly, the nominal drift of the cap ($\Delta_{avg}$) and the twist of the cap ($\theta_{twist}$) can be determined by the displacements of the actuators ($\Delta_1$ and $\Delta_2$). These are shown in Equations 10 and 11.

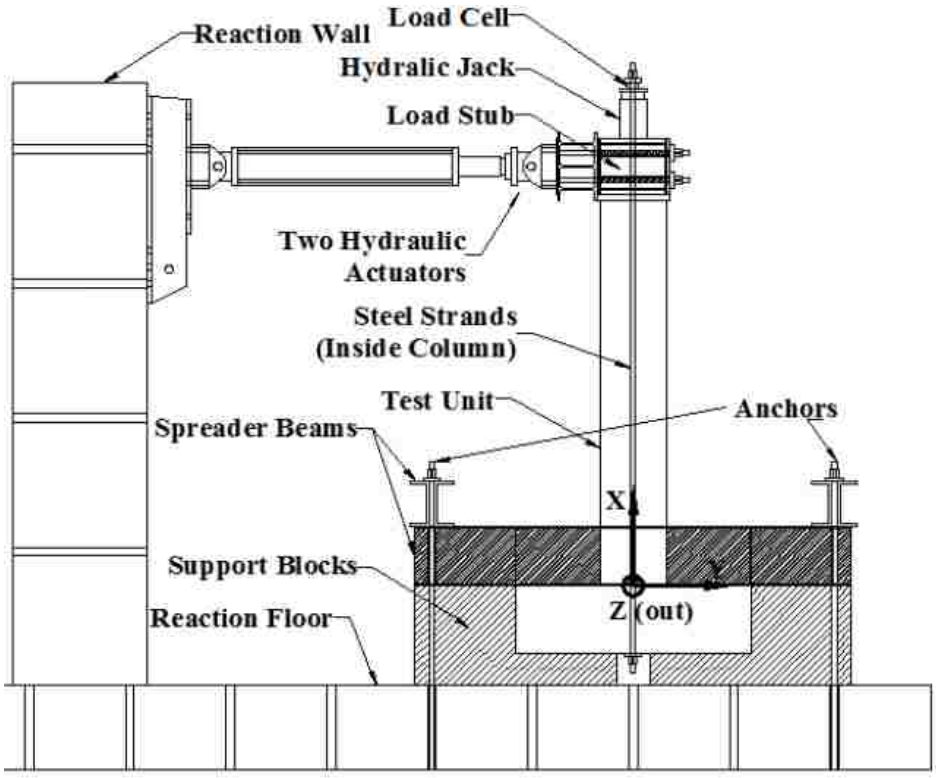


ELEVATION VIEW

(a)

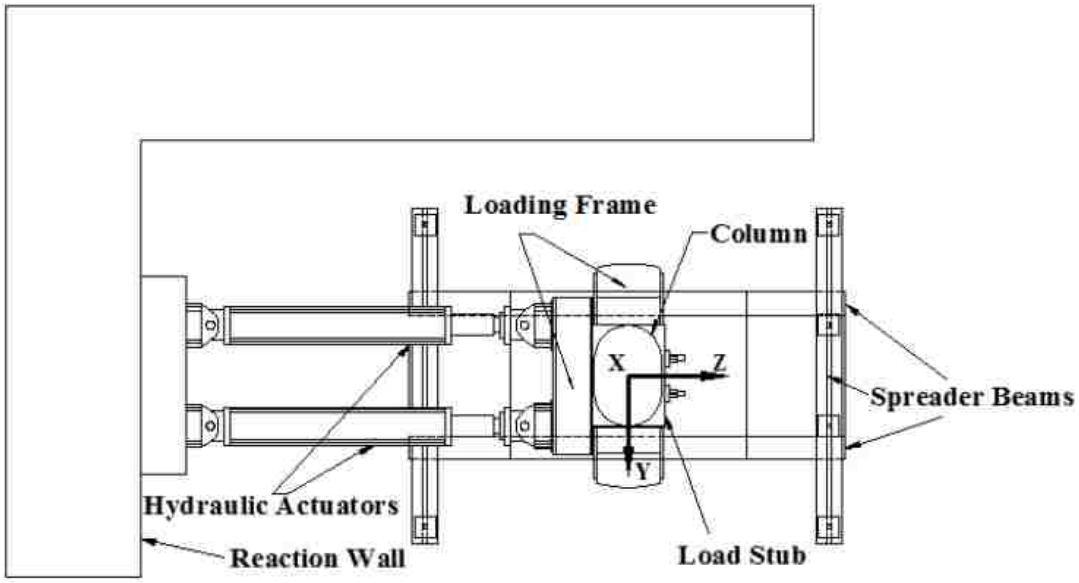


PLAN VIEW

(b)

Figure 3.3 - Test Setup

$$\Delta_{avg} = \left[\frac{(\Delta_1 + \Delta_2)}{2}\right] \quad \text{(Eq. 10)}$$

$$\theta_{twist} = \sin^{-1}\left[\frac{(\Delta_1 - \Delta_2)}{d}\right] \quad \text{(Eq. 11)}$$

In addition to the transverse loading provided by the actuators, an axial load was provided by means of prestressing tendons running through a PVC duct in the center of the column along the longitudinal axis (shown in Figure 3.3). The tendons were anchored below the footing and above a hydraulic jack placed on top of the column caps. By appling a load with the hydraulic jack, the tendons are stressed resulting in an axial load that was measured by a pair of load cells placed between the hydraulic jack and the anchor for the prestressing tendons.

### 3.5. INSTRUMENTATION

Electric resistive strain gages were affixed to both the longitudinal reinforcement and transverse reinforcement in order to ascertain the strain at the point where the gages were applied. Additionally, linearly variable differential transformer (LVDT) rosettes and/or demec rosettes were implemented to determine the nominal strain state at the surface of the column. Additional instrumentation included string potentiometers, used as displacement transducers, attached at various elevations that were used to determine the transverse displacement at that height. In order to measure the axial load applied by the prestressing strands, a load cell was mounted between the cap and the prestressing anchor. Lastly, the two actuators, used to provide the transverse load and torque, were outfitted with load cells and displacement transducers that were used to determine the imposed loading and global behavior. For the purpose of this study the data collected by the load cells and displacement transducers in the actuators will be the focus of investigation.

## 3.6. MATERIALS AND CONSTRUCTION

This section will provide an overview of the materials utilized in both the constructions of the original columns and in later repair and strengthening of those columns.

**3.6.1. Original Columns.** Materials utilized in the construction of Calt-1, Calt-2, and Calt-3included the longitudinal steel reinforcing bars, the reinforcing bars used in the transverse spirals, and the concrete.

The concrete used in the construction of the columns was intended be a 5 ksi (34.5 MPa) compressive strength mixture by design, with a 1 in. (25.4 mm) maximum aggregate size, and utilized a high-range water reducer (super plasticizer) for improved workability and flow during placement. 6 in. x 12 in. (152.4 mm x 304.8 mm) cylindrical test specimens were cast and tested in accordance with ASTM C39-04 to ascertain the compressive strength at 28 days, $f'_c$, and the compressive strength at the test day. The results are summarized in Table 3.2.

The reinforcing steel utilized for the longitudinal and spiral reinforcement conformed to ASTM A706 and were grade 60 reinforcing bars. Actual yield stress for the reinforcing steel, based on the 0.20% offset method, was 76.7 ksi (529 MPa) and 65.8 ksi (454 MPa) for the longitudinal and spiral reinforcement, respectively. The bars utilized for longitudinal reinforcement were No. 8 (1.00 in. [25.4 mm] diameter) bars, while those utilized for the spiral reinforcement are No. 4 (0.50 in. [12.7 mm] diameter) bars. The properties of the reinforcing bars are summarized in Table 3.3.

Table 3.2 - Measured Concrete Material Properties

| Column ID | Calt-1 | Calt-2 | Calt-3 |
|---|---|---|---|
| 28 Day | 4,360 psi (30.1 MPa) | 5,670 psi (39.1 MPa) | Not Reported |
| On Test Date | 5,430 psi (37.4 MPa) | 5,260 psi (36.3 MPa) | 5,860 psi (40.4 MPa) |

Table 3.3 - Measured Reinforcing Steel Properties

| Reinforcing Bar Description | Yield Strength | Ultimate Strength |
|---|---|---|
| Longitudinal (No. 8) Bars | 76,700 psi (529 MPa) | 104,100 psi (718 MPa) |
| Spiral (No. 4) Bars | 65,800 psi (454 MPa) | 98,000 psi (676 MPa) |

**3.6.2. Repaired Columns.** Repair materials that were used for R-Calt-1 and R-Calt-2 included concrete and flowable grout used to replace the damaged and removed concrete, the components of the FRP jacket, reinforcing steel bar segments attached with mechanical bar splices, and circular ties around the splices.

The damaged concrete that was removed during the repair was replaced by a combination of a high slump concrete and a pumpable grout. These were selected to have a similar compressive strength as the existing concrete (i.e., 5 ksi [34.5 MPa] nominal compressive strength).

The reinforcing steel used to replace the segments of longitudinal reinforcing bars within the plastic hinge region and the steel used to provide circular ties at the top and bottom of the plastic hinge conformed to ASTM A706. The No. 8 (1.00 in. [25.4 mm] diameter) bars used to replace segments of the longitudinal reinforcing were determined to have a yield strength of 65.5 ksi (452 MPa) and an ultimate strength of 97.9 ksi (675 MPa).

The mechanical couplers used in R-Calt-1 and R-Calt-2 were a bolt-grip (Lenton Lock from Erico) type and a cold-swaged connector (BarGrip from BarSplice) type, respectively. For R-Calt-1 Erico Lenton Lock B series for No. 8 (1.00 in. [25.4] diameter) bars were implemented to splice the longitudinal rebar. These are a bolt-grip type coupler that utilizes bolts whose heads shear off once the required torque is obtained. In the case of R-Calt-2, BarSplice XL from BarSplice Inc for No. 8 (1.00 in. [25.4] diameter) bars were implanted. These are a swaged type coupler that utilizes a hydraulic crimping tool to cold work the coupler in order to form the connection.

In the case of R-Calt-1 and R-Calt-2, layers of a 0.04 in. (1.0 mm) thick unidirectional carbon fiber (Tyfo® SCH-41) were used to create the eternally bonded jacket using a wet lay-up procedure. The manufacturer specified properties for this material are: modulus of elasticity ($E_{FRP}$) of 11,900 ksi (82,000 MPa), tensile strength ($f_u$) of 121 ksi (834 MPa), and ultimate tensile strain ($\varepsilon_{ut}$) of 0.0085 in./in. (0.0085 mm/mm).

### 3.7. TEST PROCEDURE

The testing of the original column specimens in the first part of the experimental program occurred in two stages. Each stage of loading was comprised of multiple load intervals. During each interval, progressively greater loads or displacements were applied to the column cap via the two actuators in both the push and pull directions.

During the initial stage a force controlled approach was adopted wherein the load was incrementally increased at intervals based on 10% of the predicted yielding force. This was done until yielding of the first longitudinal bar (indicated by strain gage measurements) was observed. This point was defined as displacement ductility one ($\mu_\Delta$=1) and marks the final force controlled interval before the second stage of loading.

During the second stage of loading the actuator displacements corresponding to displacement ductility one were incrementally factored up during subsequent load stages, under displacement controlled load. At each displacement level three cycles were applied to observe stiffness degradation.

A similar approach was adopted for the repaired columns, wherein the columns were initially tested under force control, to maintain the desired torque-to-moment ratio, until the predicted yielding of the first longitudinal bar. Then the columns were tested under displacement control, with three cycles being performed at each displacement level. The comparison of the displacement histories for column Calt-1 and Calt-2 to their repaired counterparts, R-Calt-1 and R-Calt-2, can be seen in Figure 3.4.

### 3.8. TEST RESULTS

This section presents the hysteretic load-deformation relationships of the three original columns the finite element model attempted to replicate. These responses are

used in the development of the boundary conditions imposed on the model, a process explained in Section 4.5.2.

For the sake of brevity, the hysteretic load-deformation relationships of the repaired columns are not included in this section, because convergence of the modified finite element model could not be obtained for the repaired columns due to numerical stability issues. The hysteretic responses of the repaired columns are reported in (Yang, 2014).

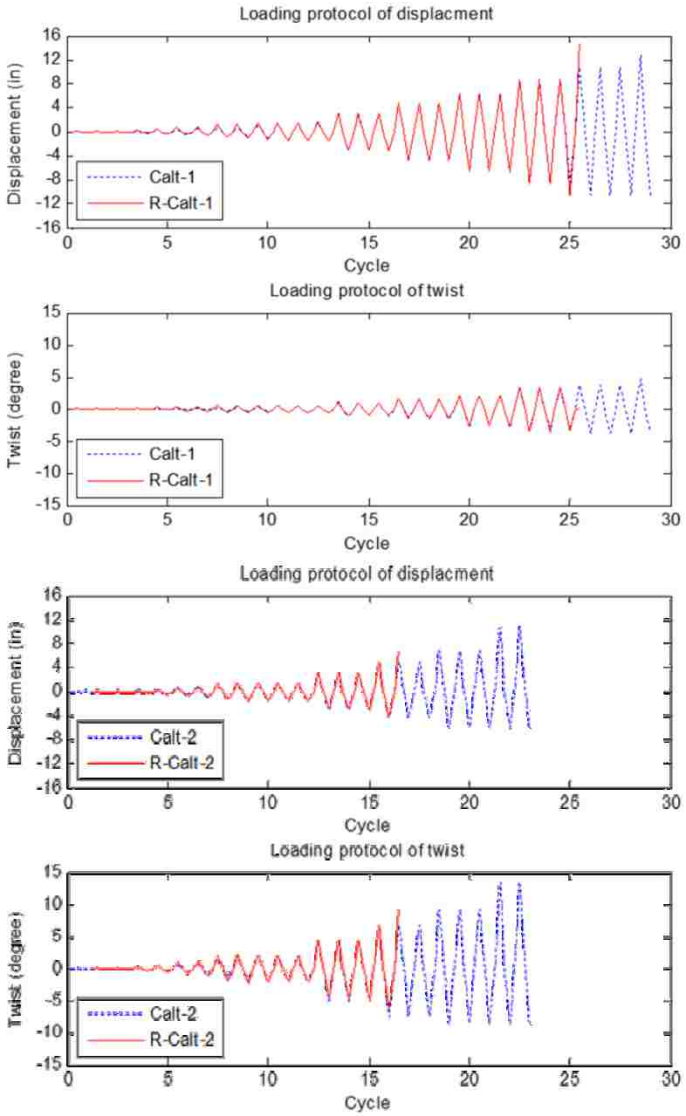


Figure 3.4 - Loading protocol of Calt-1, R-Calt-1, Calt-2, and R-Calt-2. (Yang, et al., 2015) (1 in. = 25.4 mm)

**3.8.1. Calt-1 Test Results.** The experimental response of Calt-2 is summarized within this section. These results are presented in the form of the hysteresis response of the column's base shear to cap displacement relationship and torque to twist relationship in Figure 3.5. These results are used to determine the experimental backbone curves, presented in Section 4.5.2.1.

The results for Calt-1 show that the column successfully completed three displacement controlled cycles at 1.0, 1.5, 3.0, 4.5, 6, 8, and 10 times the displacement to first yielding of the reinforcement (D1). The column then failed during cycling at twelve times the D1 displacement.

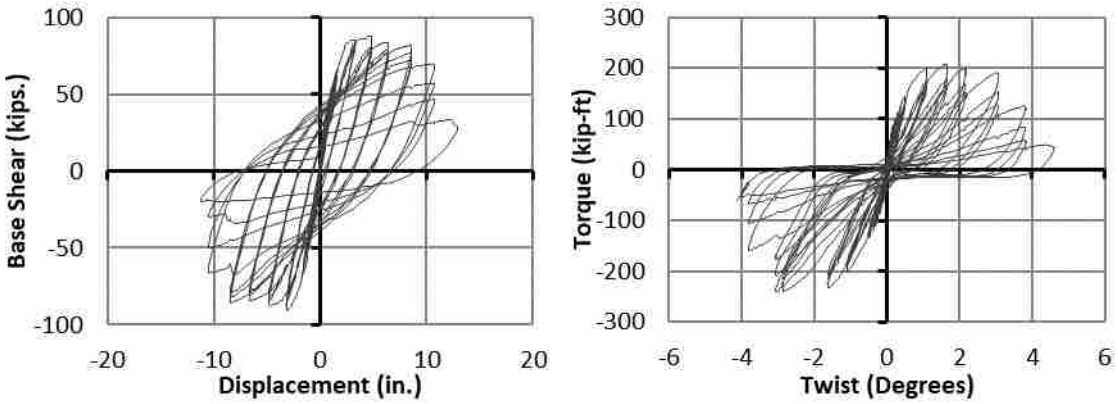


Figure 3.5 - Calt-1 Experimental Results; Shear-Displacement (left) Torque-Twist (right) (1 kip = 4.448 kN, 1 kip-ft = 1.356 kN-m, 1 in. = 25.4 mm)

**3.8.2. Calt-2 Test Results.** The experimental response of Calt-2 is summarized within this section. These results are presented in the form of the hysteresis response of the column's base shear to cap displacement relationship and torque to twist relationship in Figure 3.6. These results are used to determine the experimental backbone curves, presented in Section 4.5.2.2.

The results for Calt-2 show that the column successfully completed three displacement controlled cycles at 1, 2, 3, and 4 times the displacement to first yielding of the reinforcement (D1). The column then failed during cycling at six times the D1

displacement. It is worth noting that while cycling at six times the D1 displacement, the peak base shear was reached approximately 70% the way through the cycle. Additionally, both the peak torque and peak base shear decreased between the last load controlled cycle and first displacement control cycle. These two factors result in the short interval between the last two points of the backbone curves and the early 'saw-tooth' in the Calt-2 backbone curves, presented in Section 4.5.2.2.

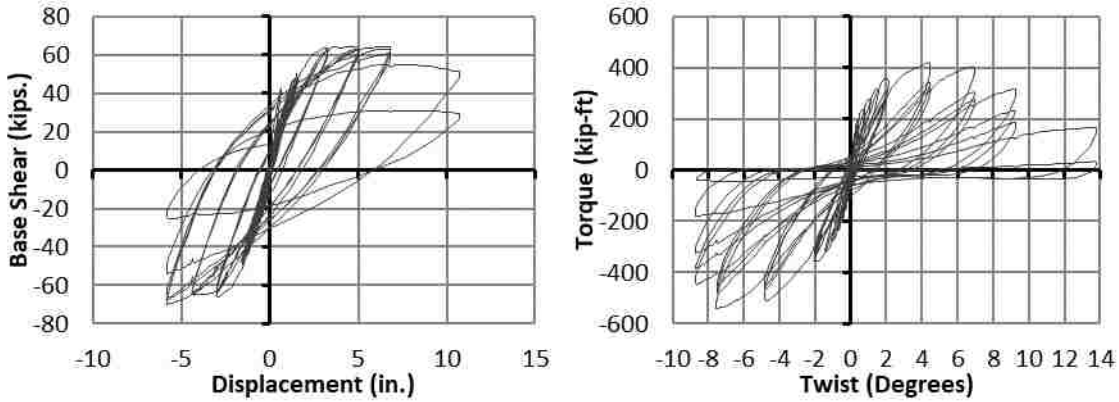


Figure 3.6 - Calt-2 Experimental Results; Shear-Displacement (left) Torque-Twist (right) (1 kip = 4.448 kN, 1 kip-ft = 1.356 kN-m, 1 in. = 25.4 mm)

**3.8.3. Calt-3 Test Results.** The experimental response of Calt-3 is summarized within this section. These results are presented in the form of the hysteresis response of the column's base shear to cap displacement relationship and torque to twist relationship in Figure 3.7. These results are used to determine the experimental backbone curves, presented in Section 4.5.2.3.

The results for Calt-3 show that the column successfully completed three displacement controlled cycles at 1, 2, 3, 5 and 6 times the displacement to first yielding of the reinforcement (D1). Similar to Calt-2, Calt-3 exhibited a decrease in the peak torque and peak base shear between the last load controlled cycle and first displacement control cycle. This results in the 'saw-tooth' in the early portions of the Calt-3 backbone curves, presented in 4.5.2.3.

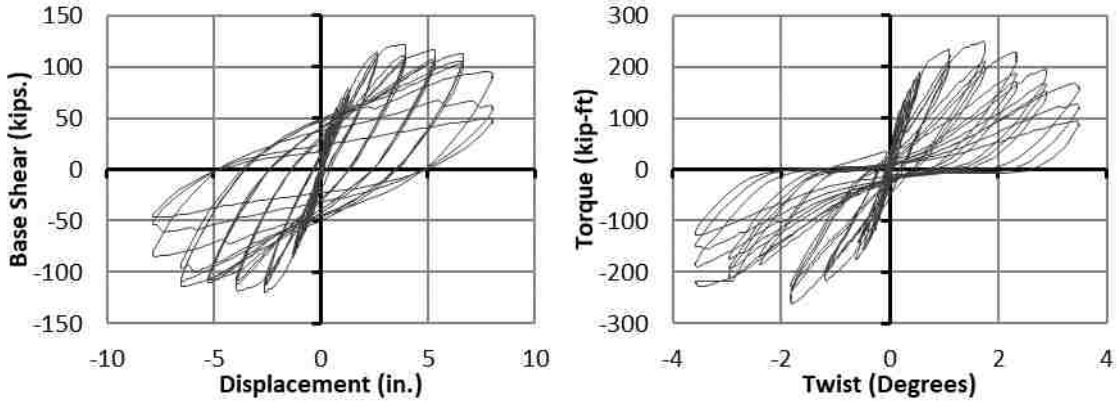


Figure 3.7 - Calt-3 Experimental Results; Shear-Displacement (left) Torque-Twist (right)
(1 kip = 4.448 kN, 1 kip-ft = 1.356 kN-m, 1 in. = 25.4 mm)

# 4. FINITE ELEMENT ANALYSIS

## 4.1. FINITE ELEMENT ALANALYSIS OVERVIEW

This section provides a description of the finite element model developed in this study. It begins with an overview of the process that led to development of the model (Section 4.2) followed by a more in-depth look at individual aspects of the model; examining first the simplification of the physical specimens geometry (Section 4.3), followed by a description of the mesh elements used to discretize the geometry (Section 4.4), an overview of boundary conditions imposed on the mesh (Section 4.5), and a description of the various material models that define the behavior of the model (Section 4.6). Section 4.7 describes the solution settings, whereas Section 4.8 discusses sources of errors. Section 4.9 presents the simulated load response of the model when displacements, equivalent to those imposed on the physical specimens, are imposed on the model. Lastly, Section 4.10 briefly describes the attempt to extend the model to the repaired, FRP-strengthened columns and the limitations encountered.

## 4.2. MODELING METHODOLOGY

A top-down approach, wherein the geometry is separately defined from the mesh that is later associated to it, was adopted for the creation of the finite element model. Using the software Siemens NX 7.5, a three-dimensional solid model of the column and its reinforcement was generated, as illustrated in Figure 4.1. This solid model was parametrically defined so as to allow for easy development of modified geometry for future studies. The solid model was then simplified by replacing the solid bodies that represented the reinforcing steel with lines defined along the centerline of the solid bodies, by sectioning off the geometry at the top and bottom of the column and deleting the now separate cap and footing, and finally by replacing the cap with a solid body that lofts the column profile to a single point at the centroid of the cap, around which the actuators are assumed to act. Lastly, the top 1.0 in. (25.4 mm) and bottom 1.0 in. (25.4 mm) were partitioned off of the solid representing concrete in order ‘soften’ the rigid boundary condition with an elastic buffer material. This is done to prevent stress concentrations that would not otherwise arise due to the finite rigidity of the cap and

footing, that the boundary condition would otherwise assume them to be infinitely rigid. The resulting bodies from this process were then imported into Abaqus CAE using Initial Graphics Exchange Specification (IGES) files. These bodies and their purposes are described and discussed in Section 4.3.

Figure 4.1 - Comprehensive Three-Dimensional CAD Model
(Note: Dimensions Given in Figure 3.1 and Figure 3.2)

### 4.3. MODEL COMPONENTS

A total of 26 bodies were used to represent the column in finite element model. These can be categorized into five groups and are identified as such by different colors in Figure 4.2.


Figure 4.2 - Model Components in Abaqus CAE

Two groups of linear bodies were utilized to represent the reinforcing bars. The first of these is comprised of 20 linear bodies representing the No. 8 (1.00 in. [25.4 mm] diameter) longitudinal reinforcing bars, shown in red. The second consists of two helical curves that represent the No. 4 (0.5 in. [12.7 mm] diameter) spiral reinforcement.

The remaining three groups were solid bodies that represent the concrete portion of the column and the cap. The column comprised two of these groups. The first group represented the bulk of the column and is shown in a translucent grey and represents the middle 9 ft.-10 in. (3.0 m) of the 10 ft. (3.05 m) the column spans from the top of the footing to the bottom of the cap. The second portion, shown in translucent green, consisted of the 1 in. [25.4 mm] slices of the column just below the cap and just above the footing. These bodies were taken separately from one another so that different material properties could be assigned at the very top and very bottom of the column. As the constraints were infinitely rigid in the finite element model, it was necessary to define a portion of the column's concrete, in the model, as a linear elastic material to prevent convergence issues stemming from unrealistic stress concentrations at the boundaries. The final group consisted of one solid body and was used to represent the column cap and transitions from a single point in the center of the cap to the column cross-section. This shape was purely for convenience as the cap was represented by discrete rigid elements, described in Section 4.4.3, whose location and orientation were tied to a single reference point. This allowed for loads and displacements to be defined at a single reference point, which existed at the tip of the solid.

## 4.4. MESH ELEMENTS

Three types of bodies needed to be discretized through meshing. These are line bodies, solid bodies, and shell bodies. Line bodies can be represented by beam and/or truss elements, solid bodies can be meshed with a variety of solid elements ranging from four node tetrahedral elements to polyhedral shapes with 14 or more faces, and shell bodies can be meshed using a variety of shell elements. The different elements used in this model and their purposes are discussed further in Section 4.4.1 to Section 4.4.3.

**4.4.1. Eight Node Brick Elements.** These elements were used to model all deformable solids in the model, including the concrete and the elastic buffer at the top and bottom of the column. The C3D8R element, used in this model, is a linear brick element with reduced integration. The term "reduced integration" refers to the element having only a single integration point, used to evaluate the material response, as compared to having eight integration points with the C3D8 linear brick element with full integration. In general, this substantially reduces the computational demand but results in an increase in discretization error and, because the integration point is in the center of the element, eliminates the ability to evaluate stress concentrations at the boundary. The issue with increased discretization error, associated with reduced integration, is mitigated with sufficient levels of h-refinement, where more of the same order elements are utilized. This is convenient since the curved surfaces of the column require reasonably small spacing between nodes to properly discretize the geometry. Additionally, accurately accounting for contact stresses and boundary conditions is rendered superfluous by the elastic buffer at the top and bottom of the column, thereby eliminating the need for additional integration points at the boundary nodes.

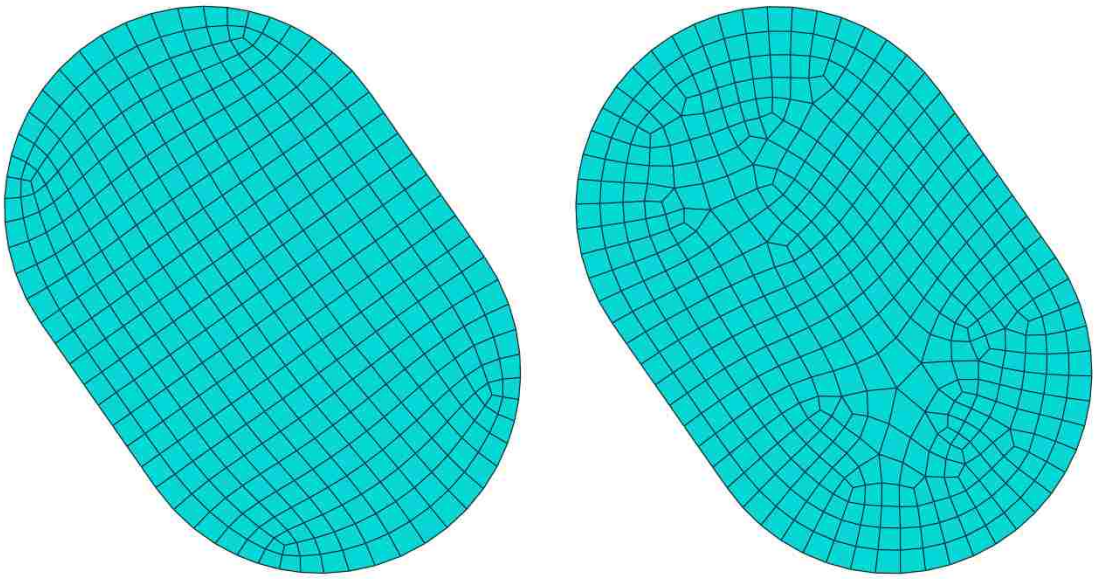

Figure 4.3 - Comparison of Medial Axis (Left) to Advancing Front (Right) Meshing

The mesh for the solid bodies was generated using the medial axis algorithm in Abaqus CAE. This method breaks the region to be meshed into several simpler regions and generates a structured mesh in each region. This method results in a more regular mesh than the alternative "advancing front" meshing algorithm that generates layer after layer of elements, advancing from the boundaries of the region. For the geometry of the column the medial axis algorithm results in a more regular and balanced mesh. A comparison of the resulting meshes produced by these methods is presented in Figure 4.3.

**4.4.2. Two Node Beam Elements.** These elements were utilized to mesh both the longitudinal reinforcement and the transverse spiral reinforcement. Beam elements, as opposed to truss elements, were utilized to account for the reinforcing bars resistance to bending and shear by restricting relative rotation between adjacent beam elements. The B31 element was selected for the role and is a Timoshenko beam element that accounts for transverse shear deformation. This is because these elements assume plane sections remain plane but not necessarily perpendicular to the centerline of the beam element. In two dimensions Timoshenko beam elements are governed by two equations, Equation 12 and Equation 13, that are defined in terms of deflection, δ, and rotation, ψ, where $c_f$ is the elastic foundation modulus of a beam element.

$$-\frac{d}{dx}\left[GAK_s\left(\Psi+\frac{d\delta}{dx}\right)\right]+c_f\delta=q \qquad \text{(Eq. 12)}$$

$$-\frac{d}{dx}\left(EI\frac{d\Psi}{dx}\right)+GAK_s\left(\Psi+\frac{d\delta}{dx}\right)=0 \qquad \text{(Eq. 13)}$$

**4.4.3. Discrete Rigid Elements.** These are a special type of shell element used to define the rigid body of the lofted cap used to impose the desired drift and twist at the top of the column. These elements are non-deformable quadrilateral and triangular shell elements, R3D4 and R3D3 respectively. By using discrete rigid elements to model the surface of the solid lofted shape the need to mesh the internal volume of the lofted cap is eliminated, and nodal values related the development of the stiffness matrix need not be stored, reducing the computational demand. In these elements, the location of all nodes is dependent on the location and orientation of a reference point that in turn acts as the reaction point for any load imposed on the rigid body.

## 4.5. BOUNDARY CONDITIONS AND CONSTRAINTS

The way in which the bodies within the finite element model interact with each other and with the imposed boundary conditions can impact both the results and stability of the analysis. There were essentially three types of interactions present in this model. The first were reactionary boundary conditions that are constant conditions externally imposed on the model. These reactionary boundary conditions are discussed further in Section 4.5.1. Another type of external boundary condition is those intended to load the structure and change during the course of an analysis. These boundary conditions are discussed in Section 4.5.2. Lastly, there were interactions between bodies in the model, where neighboring bodies act as each other's boundary condition. The interactions are discussed further detail in Section 4.5.3.

**4.5.1. Reactionary Boundary Conditions.** Constraints to prevent rigid body motion were defined along the lower face of the lower 1 in. (25.4 mm) thick elastic portion of the concrete and on the lowest nodes of each longitudinal reinforcing bar and each helical spiral reinforcement. These constraints defined the motion in all six degrees of freedom as zero at the applicable nodes.

**4.5.2. Load and Displacement Imposing Boundary Conditions.** Loading of the model is achieved through the reference point on the discrete rigid body representing the cap of the column. In this model, the tip of the lofted cap was defined as the reference point. This point allows for convenient loading of the finite element model by defining either load or fixed displacements at the reference point and recording the reaction force at the reference point.

The loading of the column and measurement of reactions was accomplished through the reference point in three key ways. Firstly, the axial load provide by the prestressing cables was simulated by apply a fixed load to this reference point. This fixed load was applied in the first step of the simulation and consisted of a vertical load of 150 kips (667 kN), and was defined such that it would follow any rotation of the reference point in subsequent steps. In this way, the fixed load is always point along a vector between the reference point and the centroid of the surface where the cap-to-column interaction is defined. This is similar to how the prestressing cables in the experimental study (see Section 3.4) have a tendency to act normal to the cap of the column.

Additionally, this reference point was subjected to fixed displacement boundary conditions to impose the desired drift and twist values, measured during the experimental study, during subsequent steps. Lastly the reaction forces on the reference node were used to determine the simulated base shear and torsional moment.

The magnitude of the desired drift and twist at the later load stages were prescribed based on the displacements corresponding to the peak moment recorded at the first cycle of each drift level in the experimental tests (see Section 3.8). These peaks were used to form the experimental back-bone curves to which the model results were compared. These peaks were taken from the first cycle of each positive displacement level (i.e. those load cycles primarily in the positive Y-axis of Figure 3.3a). This was done in order to minimize the impact of hysteretic damage on the resulting back-bone curve to more closely approximate the static back-bone curve, which the model simulates, from the cyclic results. The displacements imposed during the loading steps utilized a subset of the peaks to break the simulation down into convenient intervals for varying the solutions settings, as defined in Section 4.7, to reduce unnecessary computational effort during less computational demanding portions of the columns behavior. For example, the solution requirements for the model prior to material nonlinearities is less demanding than during portion of simulation influenced heavily by both material and geometric nonlinearities; thus, it is beneficial to treat these portions of the simulation differently. The subset of the peak values used to define the displacements for the various load steps is referred to hereafter as the control points. The peak values and control points are abbreviated as PV and CP, respectively, throughout this thesis.

**4.5.2.1. Calt-1 peak values and control points.** Peak values and corresponding control points were selected from the experimental results, of cycles with positive displacements, that are summarized in Section 3.8.1 per the methods described in Section 4.5.2 of this thesis. As the selection of these points is dependent on the maximum moment, which is derived from the measured base shear multiplied by the moment arm, the measured drift-shear relationship and corresponding peak values are plotted in Figure 4.4. These peak values and corresponding control points are then tabulated in Table 4.1. Additionally, the experimental backbone curves, to which the numerical results are compared, are derived from these peak values and are shown in Figure 4.5 and Figure 4.6

for the base shear-displacement relationship and torque-twist relationship, respectively, where displacement and twist are determined at the column cap. Finally, the torque-to-moment ratio (T/M) of these peak values is presented in Figure 4.7 as a function of cap displacement.

**4.5.2.2. Calt-2 peak values and control points.** Peak values and corresponding control points were selected from the experimental results, of cycles with positive displacements, that are summarized in Section 3.8.2 per the methods described in Section 4.5.2 of this thesis. As the selection of these points is dependent on the maximum moment, which is derived from the measured base shear multiplied by the moment arm, the measured drift-shear relationship and corresponding peak values are plotted in Figure 4.8. These peak values and corresponding control points are then tabulated in Table 4.2. Additionally, the experimental backbone curves, to which the numerical results are compared, are derived from these peak values and are shown in Figure 4.9 and Figure 4.10 for the base shear-displacement relationship and torque-twist relationship, respectively, where displacement and twist are determined at the column cap. Finally, the torque-to-moment ratio (T/M) of these peak values is presented in Figure 4.11 as a function of cap displacement.

**4.5.2.3. Calt-3 peak values and control points**. Peak values and corresponding control points were selected from the experimental results, of cycles with positive displacements, that are summarized in Section 3.8.3 per the methods described in Section 4.5.2 of this thesis. As the selection of these points is dependent on the maximum moment, which is derived from the measured base shear multiplied by the moment arm, the measured drift-shear relationship and corresponding peak values are plotted in Figure 4.12. These peak values and corresponding control points are then tabulated in Table 4.3. Additionally, the experimental backbone curves, to which the numerical results are compared, are derived from these peak values and are shown in Figure 4.13 and Figure 4.14 for the base shear-displacement relationship and torque-twist relationship, respectively, where displacement and twist are determined at the column cap. Finally, the torque-to-moment ratio (T/M) of these peak values is presented in Figure 4.15 as a function of cap displacement.

### 4.5.3. Interactions and Kinematic Constraints Between Components.

Kinematic relationship between the various components are required to be defined within the finite element model in order to ensure strain compatibility between the various components. In other words, interactions had to defined such that the equal and opposite loading applied between the bodies results in the one or more bodies deforming together.

Two types of interactions were utilized in the construction of this model. The first was embedded constraints that were used to define the interaction between the concrete and the steel reinforcement. The second was tie constraints that were used to define the interactions between the mating surfaces of the inelastic and elastic solid bodies representing the concrete and the cap.

To define the embedded relationship of the reinforcing bar within the concrete a beam-in-solid embedded relationship was defined between the inelastic set of concrete and the set of reinforcement, both longitudinal and transverse, beam elements contained wholly within the inelastic portion of the concrete. In this configuration, the inelastic concrete elements constitute what is referred to in Abaqus as the host element set, and the reinforcing bar elements constitute the embedded elements. This embedded constraint cannot be extended to the elastic portions of the concrete, at the extreme top and bottom of the column, as this would result in nodes involved in the embedded relationship also being involved in the tie constraint discussed in following paragraph. This results in an over constrained condition and the solver neglecting the constraint definition.

The remaining interactions defined in this model take the form of a surface-based tie constraint in which a constraint is formed between two surfaces on the geometry, a master and a slave surface. In this approach a single slave node's displacements are related to the displacements of multiple nodes on the master surface. This results in reduced stress discontinuities in the vicinity of the interaction, sometimes referred to as numerical noise, as compared to other interaction definitions (Dassault Systems, 2010). This benefit can be numerically costly, particularly in models such as this where a large fraction of tied degrees of freedom exists. However, the numerical noise, associated with other interaction definitions, can result in stability issues when combined with nonlinear materials models.

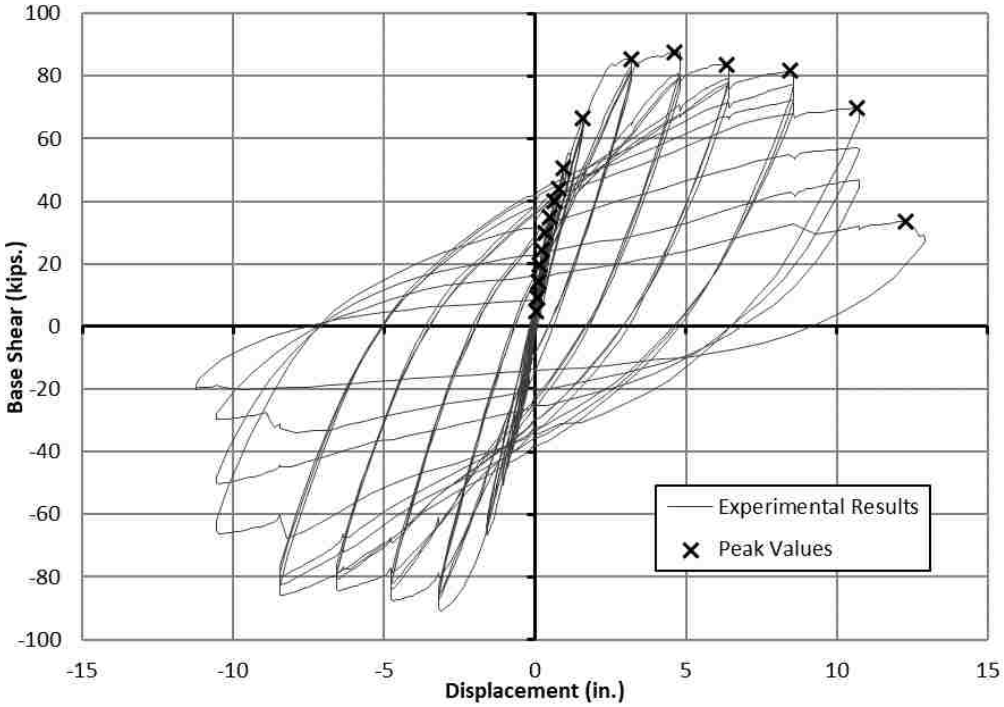


Figure 4.4 - Calt-1 Base Shear vs. Cap Displacement Experimental Results and Corresponding Peak Values (1 kip = 4.448 kN, 1 in. = 25.4 mm)

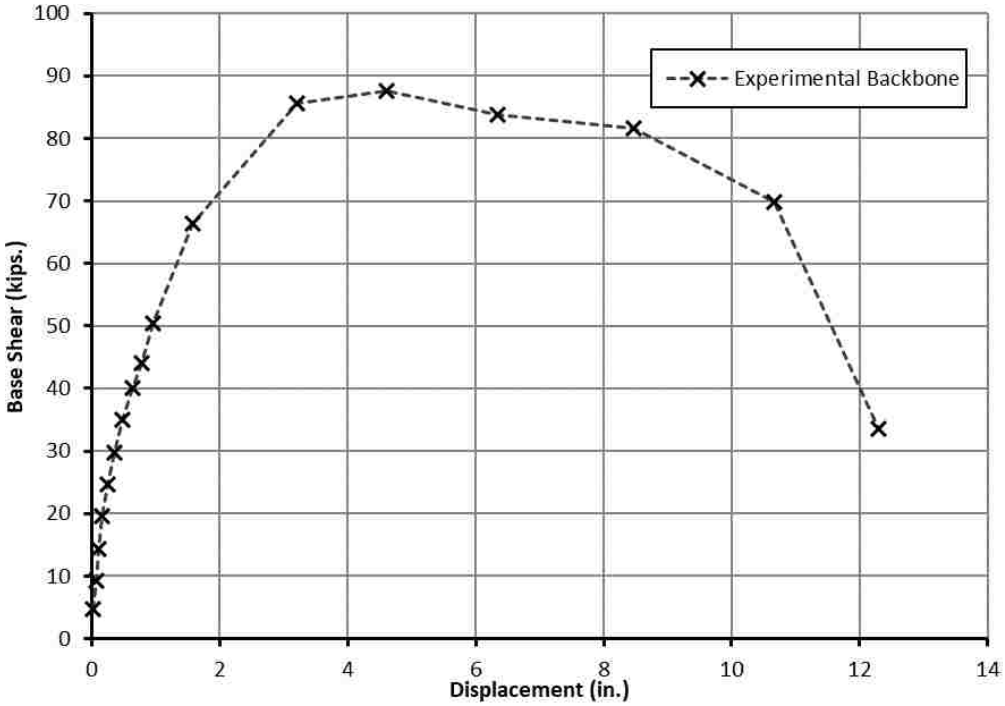


Figure 4.5 - Calt-1 Base Shear-to-Cap Displacement Backbone Relationship (1 kip = 4.448 kN, 1 in. = 25.4 mm)

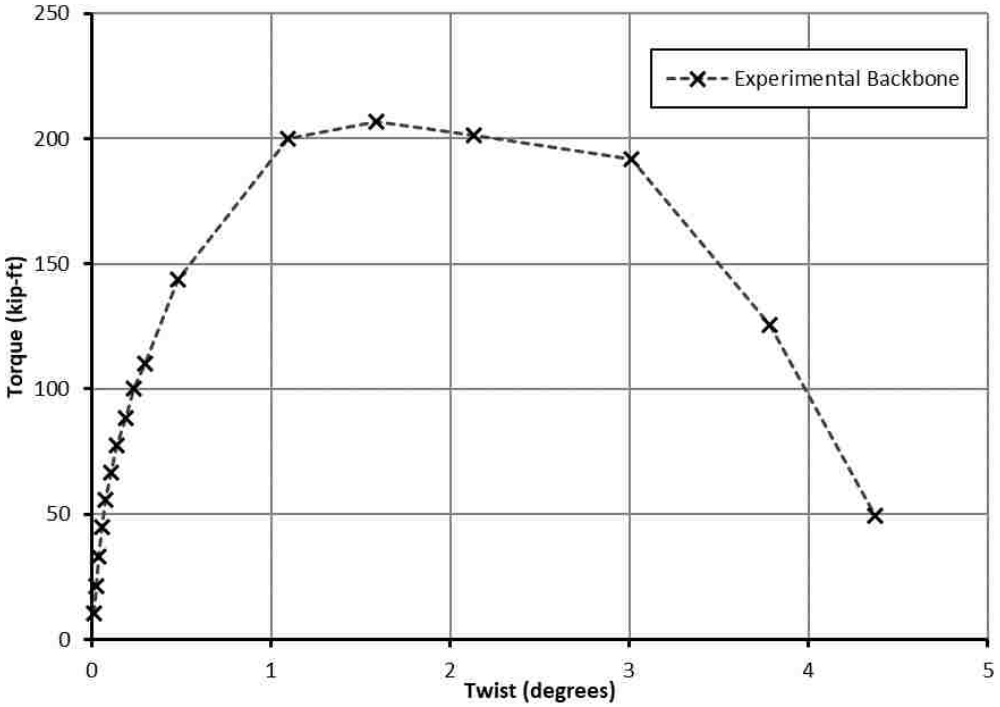


Figure 4.6 - Calt-1 Torque-to-Cap Twist Backbone Relationship
(1 kip-ft = 1.356 kN-m, 1 in. = 25.4 mm)

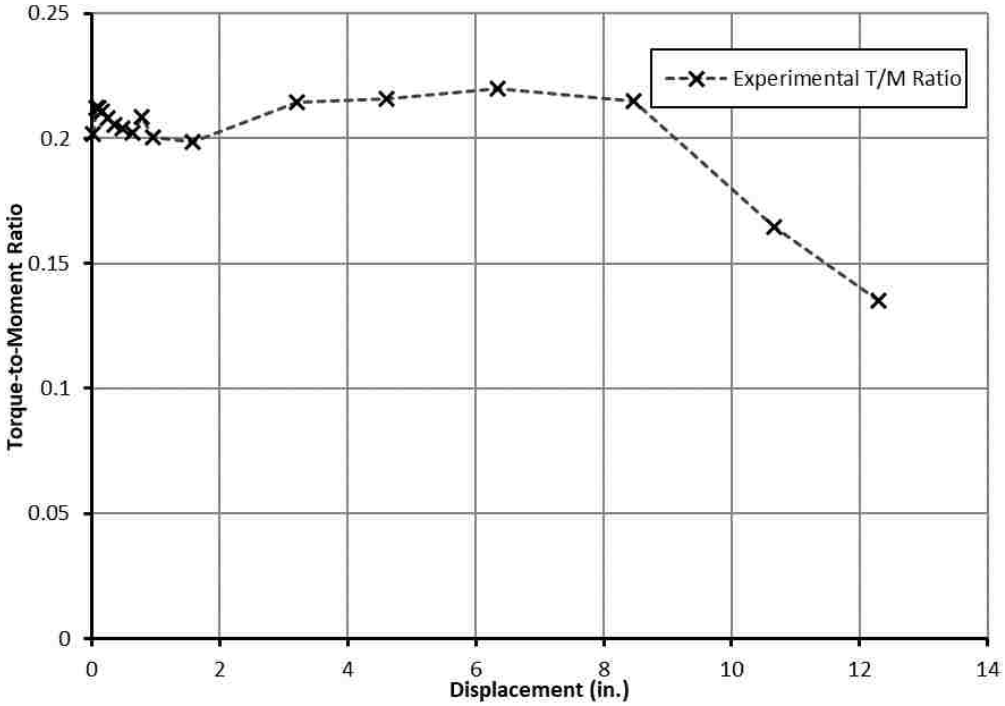


Figure 4.7 - Calt-1 Peak Values from Torque to Moment (T/M) Relationship
(1 in. = 25.4 mm)

Table 4.1 - Calt-1 Peak Values and Model Control Points

| Peak Value (PV) Identifier | Control Point (CP) Identifier | Cap Displacement (in.) | Base Shear (kips) | Cap Twist (degrees) | Torque (kip-ft) |
|---|---|---|---|---|---|
| 0.1*Fy | - | 0.0261 | 4.7 | 0.0162 | 10.4 |
| 0.2*Fy | - | 0.0638 | 9.3 | 0.0272 | 21.5 |
| 0.3*Fy | - | 0.1129 | 14.4 | 0.0404 | 33.2 |
| 0.4*Fy | - | 0.1678 | 19.6 | 0.0580 | 45.0 |
| 0.5*Fy | - | 0.2459 | 24.6 | 0.0749 | 55.9 |
| 0.6*Fy | - | 0.3546 | 29.8 | 0.1049 | 66.8 |
| 0.7*Fy | - | 0.4849 | 34.9 | 0.1424 | 77.7 |
| 0.8*Fy | - | 0.6321 | 40.1 | 0.1871 | 88.6 |
| 0.9*Fy | - | 0.7852 | 44.0 | 0.2362 | 100.2 |
| D1 | CP-1 | 0.9499 | 50.4 | 0.2972 | 110.3 |
| D1.5 | CP-2 | 1.5744 | 66.4 | 0.4844 | 143.8 |
| D3 | CP-3 | 3.1984 | 85.5 | 1.0928 | 200.2 |
| D4.5 | CP-4 | 4.6146 | 87.7 | 1.5877 | 206.6 |
| D6 | - | 6.3378 | 83.7 | 2.1353 | 201.1 |
| D8 | - | 8.4624 | 81.7 | 3.010 | 191.7 |
| D10 | - | 10.6587 | 69.9 | 3.7848 | 125.7 |
| D12 | - | 12.2916 | 33.5 | 4.3721 | 49.5 |
| xD18 | CP-5 | 17.9909 | - | 6.1632 | - |

NOTES: Peak Value xD18 was extrapolated for use as a control point that ensured the model ran to failure. The displacements for xD18 are those of D12 plus six times the displacements of D1.

1 kip = 4.448 kN, 1 in. = 25.4 mm, 1 ft = 304.8 mm

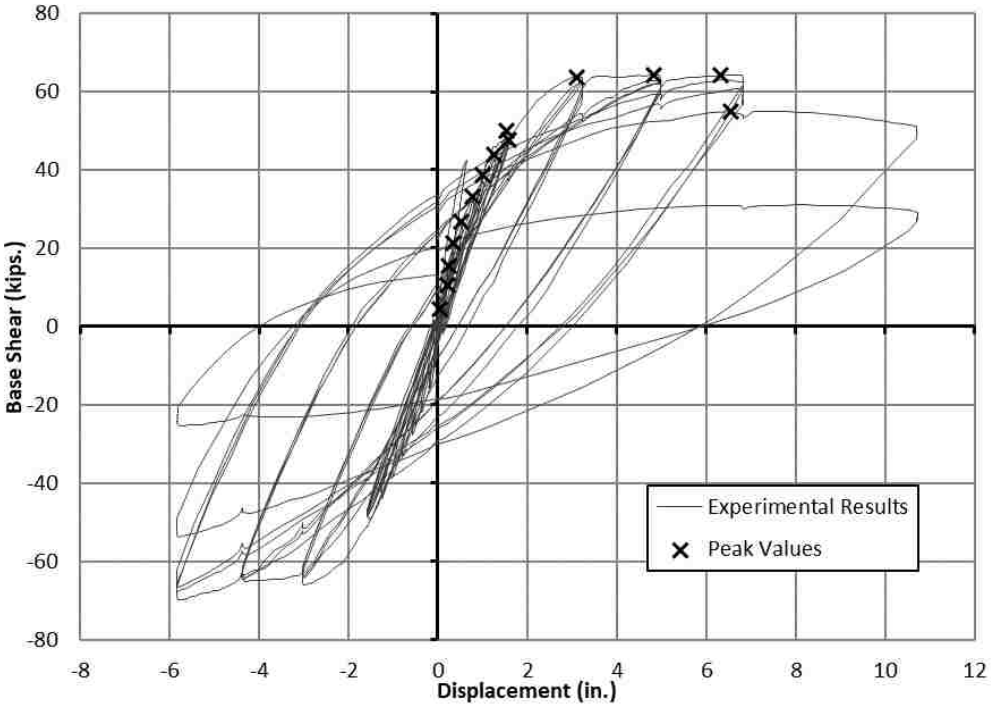


Figure 4.8 - Calt-2 Base Shear vs. Cap Displacement Experimental Results and Corresponding Peak Values (1 kip = 4.448 kN, 1 in. = 25.4 mm)

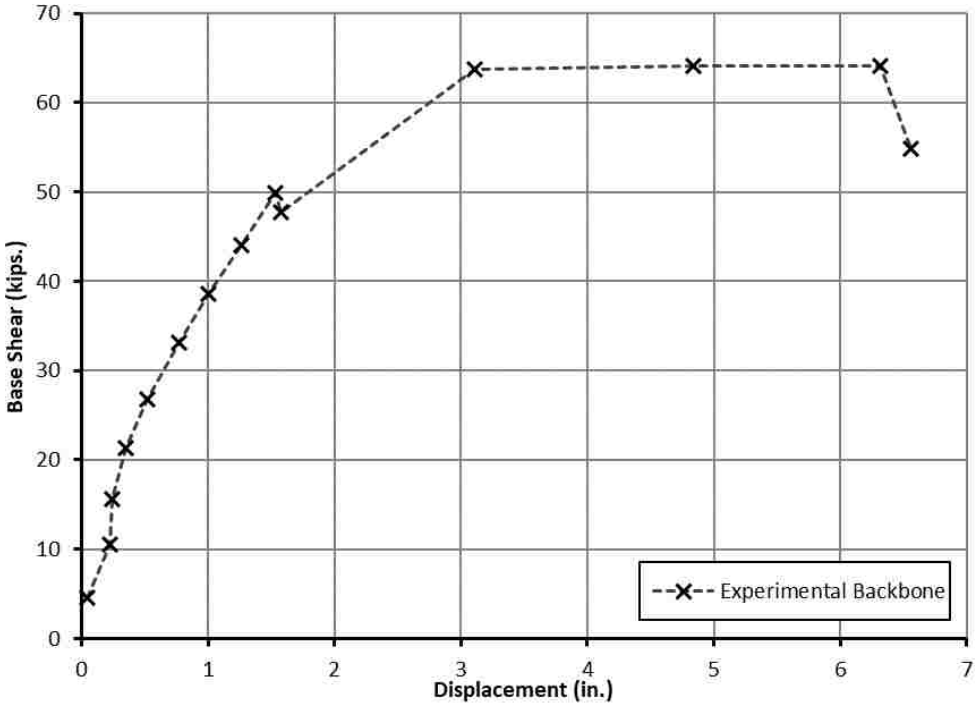


Figure 4.9 - Calt-2 Base Shear-to-Cap Displacement Backbone Relationship (1 kip = 4.448 kN, 1 in. = 25.4 mm)

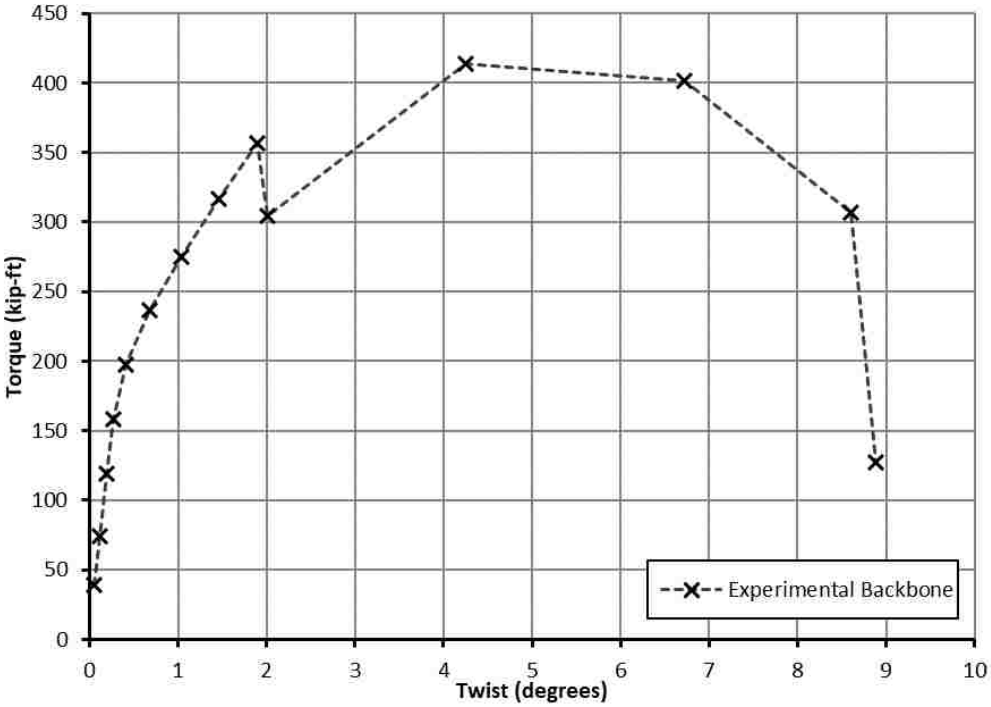


Figure 4.10 - Calt-2 Torque-to-Cap Twist Backbone Relationship
(1 kip-ft = 1.356 kN-m, 1 in. = 25.4 mm)

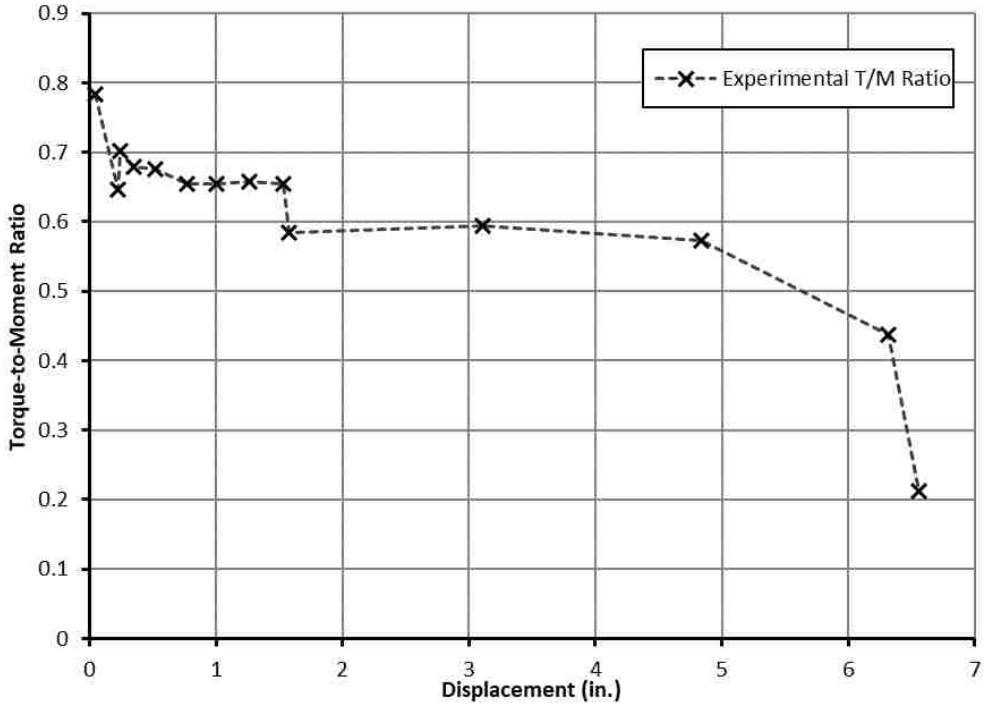


Figure 4.11 - Calt-2 Peak Values from Torque to Moment (T/M) Relationship
(1 in. = 25.4 mm)

Table 4.2 - Calt-2 Peak Values and Model Control Points

| Peak Value (PV) Identifier | Control Point (CP) Identifier | Cap Displacement (in.) | Base Shear (kips) | Cap Twist (degrees) | Torque (kip-ft) |
|---|---|---|---|---|---|
| 0.1*Fy | - | 0.0495 | 4.6 | 0.0555 | 39.1 |
| 0.2*Fy | - | 0.2225 | 10.6 | 0.1200 | 74.7 |
| 0.3*Fy | - | 0.2381 | 15.6 | 0.1929 | 119.1 |
| 0.4*Fy | - | 0.3471 | 21.3 | 0.2689 | 158.3 |
| 0.5*Fy | - | 0.5172 | 26.8 | 0.4069 | 197.6 |
| 0.6*Fy | - | 0.7670 | 33.1 | 0.6763 | 236.7 |
| 0.7*Fy | - | 0.9996 | 38.6 | 1.0339 | 275.3 |
| 0.8*Fy | - | 1.2646 | 44.0 | 1.4592 | 316.5 |
| 0.9*Fy | - | 1.5352 | 49.9 | 1.8955 | 356.9 |
| D1 | CP-1 | 1.5738 | 47.8 | 2.0114 | 304.8 |
| D2 | CP-2 | 3.1128 | 63.8 | 4.2524 | 413.9 |
| D3 | CP-3 | 4.8354 | 64.2 | 6.7142 | 401.9 |
| D4 | CP-4 | 6.3151 | 64.2 | 8.6015 | 306.8 |
| D6 | - | 6.5570 | 54.9 | 8.8832 | 127.5 |
| xD8 | CP-5 | 9.7047 | - | 12.9805 | - |

NOTES: Peak Value xD8 is extrapolated for use as a control point that ensures the model runs to failure. The displacements for xD8 are those of D6 plus two times the displacements of D1.

1 kip = 4.448 kN, 1 in. = 25.4 mm, 1 ft = 304.8 mm

## 4.6. MATERIAL MODELS

The mathematical models that describe the behavior of the materials are known collectively as the material models. The resulting load-deformation behavior of a structural element is a function of the materials that it is composed of.

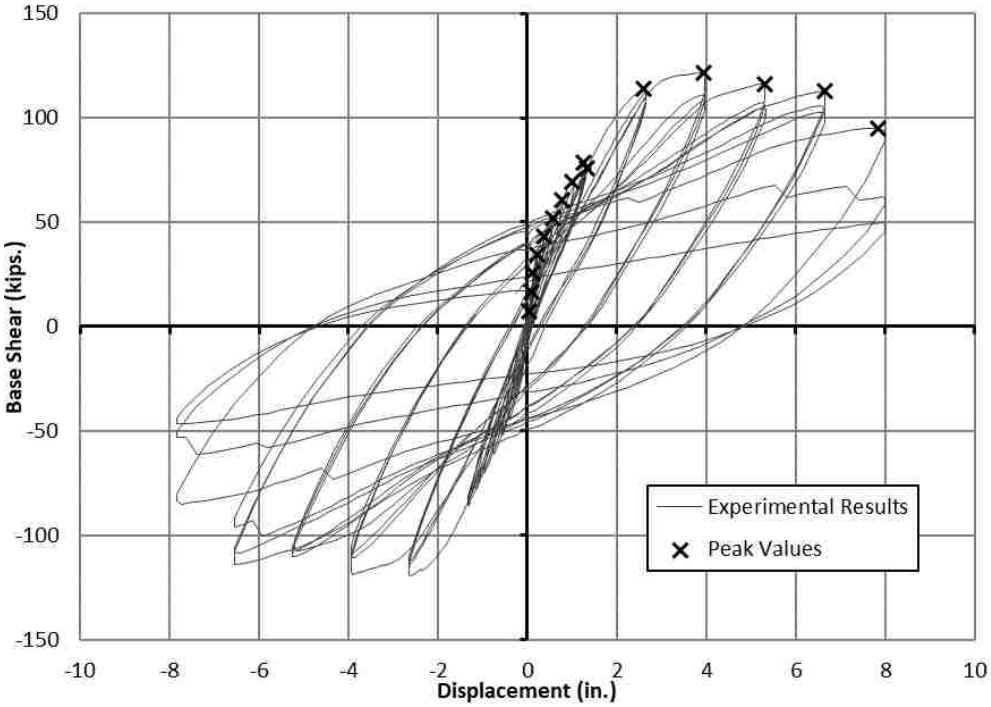


Figure 4.12 - Calt-3 Base Shear vs. Cap Displacement Experimental Results and Corresponding Peak Values (1 kip = 4.448 kN, 1 in. = 25.4 mm)

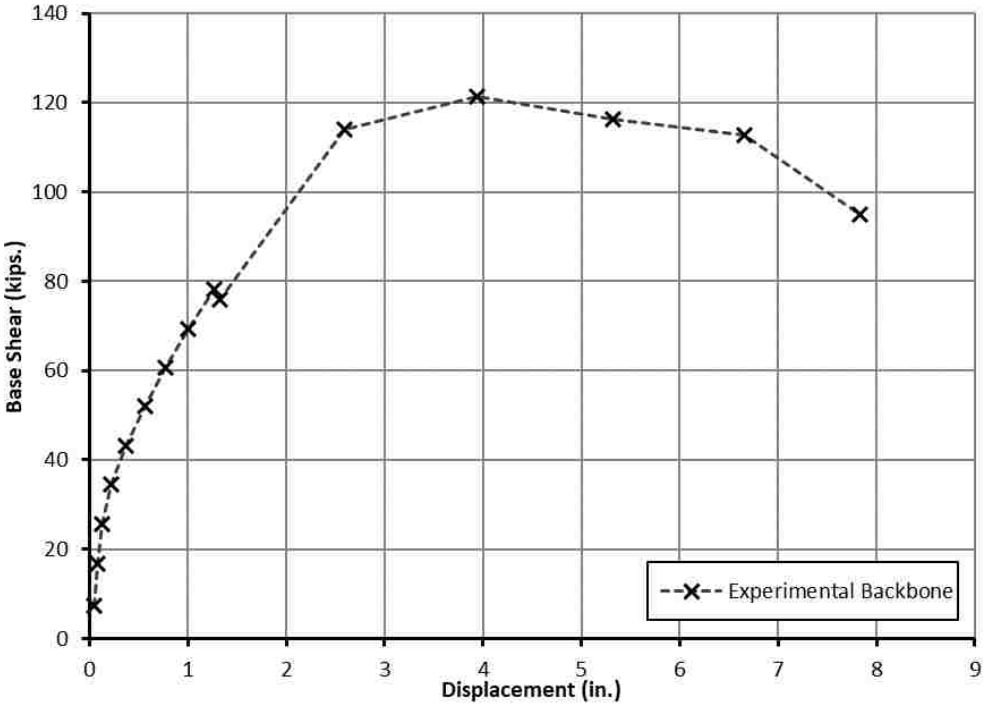


Figure 4.13 - Calt-3 Base Shear-to-Cap Displacement Backbone Relationship (1 kip = 4.448 kN, 1 in. = 25.4 mm)

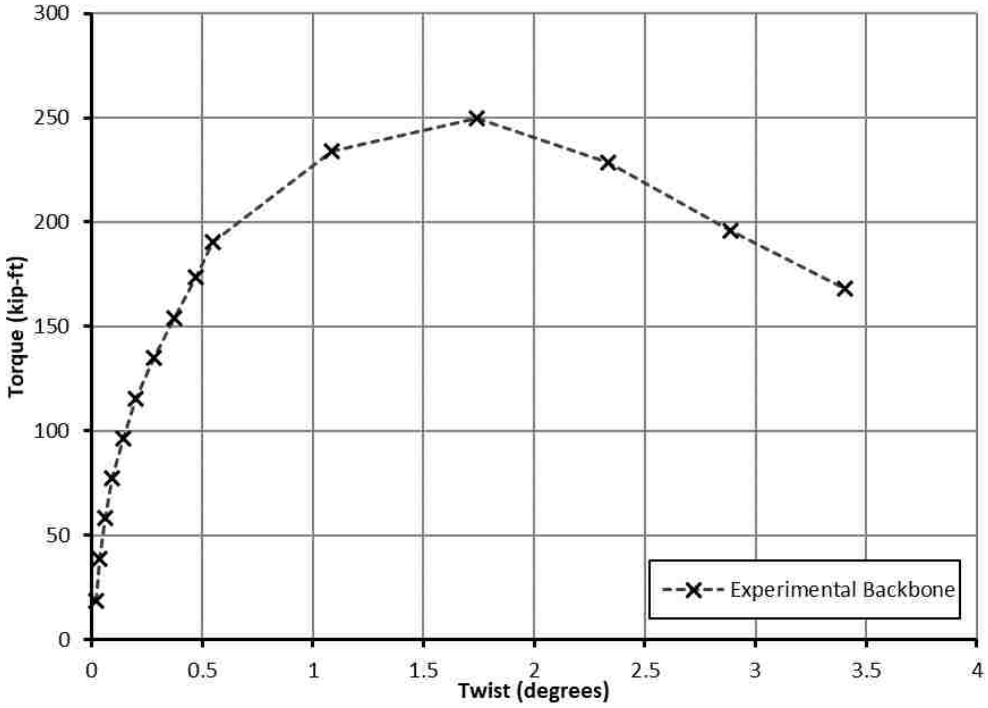


Figure 4.14 - Calt-3 Torque-to-Cap Twist Backbone Relationship
(1 kip-ft = 1.356 kN-m, 1 in. = 25.4 mm)

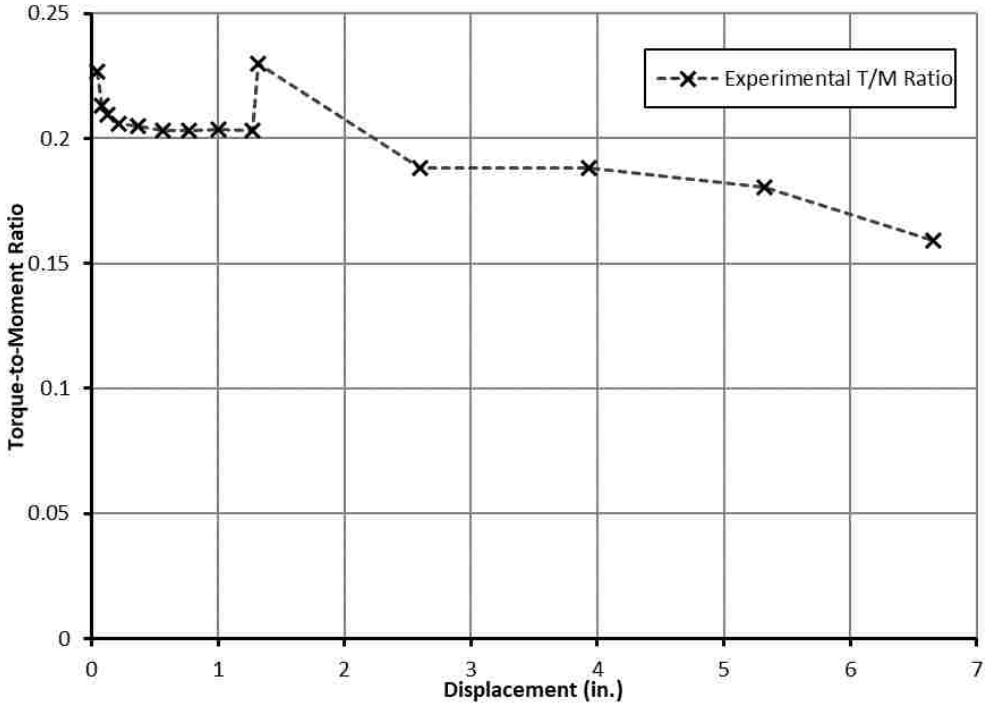


Figure 4.15 - Calt-3 Peak Values from Torque to Moment (T/M) Relationship
(1 in. = 25.4 mm)

Table 4.3 - Calt-3 Peak Values and Model Control Points

| Peak Value (PV) Identifier | Control Point (CP) Identifier | Cap Displacement (in.) | Base Shear (kips) | Cap Twist (degrees) | Torque (kip-ft) |
|---|---|---|---|---|---|
| 0.1*Fy | - | 0.0470 | 7.5 | 0.0198 | 18.5 |
| 0.2*Fy | - | 0.0822 | 16.7 | 0.0359 | 38.9 |
| 0.3*Fy | - | 0.1271 | 25.5 | 0.0623 | 58.3 |
| 0.4*Fy | - | 0.2166 | 34.4 | 0.0923 | 77.3 |
| 0.5*Fy | - | 0.3684 | 43.1 | 0.1458 | 96.4 |
| 0.6*Fy | - | 0.5604 | 52.0 | 0.2022 | 115.4 |
| 0.7*Fy | - | 0.7671 | 60.8 | 0.2791 | 134.7 |
| 0.8*Fy | - | 1.0000 | 69.4 | 0.3723 | 154.2 |
| 0.9*Fy | CP-1 | 1.2679 | 78.3 | 0.4726 | 173.7 |
| D1 | CP-2 | 1.3192 | 76.0 | 0.5466 | 190.6 |
| D2 | CP-3 | 2.5952 | 114.0 | 1.0836 | 234.2 |
| D3 | - | 3.9367 | 121.5 | 1.7403 | 249.7 |
| D4 | - | 5.3197 | 116.2 | 2.3335 | 228.7 |
| D5 | CP-4 | 6.6597 | 112.8 | 2.8876 | 195.7 |
| D6 | - | 7.8321 | 95.0 | 3.4059 | 168.0 |
| xD8 | CP-5 | 10.4705 | - | 4.5018 | - |

NOTES: Peak Value xD8 is extrapolated for use as a control point that ensures the model runs to failure. The displacements for xD8 are those of D6 plus two times the displacements of D1.

1 kip = 4.448 kN, 1 in. = 25.4 mm, 1 ft = 304.8 mm

As a result, reasonably accurate material models are a requisite to obtain realistic results through finite element modeling. As such, the material models ought to exhibit similar characteristics to their physical counterparts in order for the finite element model to accurately simulate the behavior of the physical system. The following sections detail

the material models used to represent the materials in both the original and repaired columns.

**4.6.1. Concrete.** The Concrete Damaged Plasticity (CDP) model in Abaqus was selected to represent concrete in the finite element model. The CDP model is a derivative of the Drucker-Prager strength hypothesis, which is pressure dependent (as discussed in Section 2.2.1). It results in a conical failure surface in stress space and a circular failure surface in the deviatoric stress space. The CDP model in Abaqus has a yield surface based on that proposed by Lee and Fenves (1998) that is a modification of yield criterion proposed by Lubliner et al. (1989) (discussed in Section 2.2.4). This adopted strength hypothesis is similar to the Drucker-Prager hypothesis except that it has a failure surface that may be non-circular in the deviatoric stress space, shown in Figure 4.16. Instead, the failure surface is dependent on the ratio of the distance from the hydrostatic axis to the tension meridian and the distance from the hydrostatic axis to the compression meridian, denoted by $K_c$ in Figure 4.16. The yield function of Abaqus' concrete damaged plasticity model is presented in Equation 14, where $\alpha$ and $\beta$ are dimensionless constants, $\bar{q}$ is the Mises equivalent effective stress, $\bar{p}$ is the effective hydrostatic pressure, $\tilde{\varepsilon}^{pl}$ is the set of hardening variables, $\hat{\bar{\sigma}}_{max}$ is the maximum principal stress, $\gamma$ is a coefficient accounting for stress states of triaxial compression, and $\bar{\sigma}_c$ is the compressive cohesion stress (Dassault Systems, 2010).

$$F(\bar{\sigma}, \tilde{\varepsilon}^{pl}) = \frac{1}{1-\alpha}[\bar{q} - 3\alpha\bar{p} + \beta(\tilde{\varepsilon}^{pl})\langle\hat{\bar{\sigma}}_{max}\rangle - \gamma\langle-\hat{\bar{\sigma}}_{max}\rangle] - \bar{\sigma}_c(\tilde{\varepsilon}^{pl}) \leq 0 \quad \text{(Eq. 14)}$$

This can be shown to be almost identical to the yield function presented by Lee and Fenves, with the addition of the "$-\gamma\langle-\hat{\bar{\sigma}}_{max}\rangle$" term that enters the yield function in states of triaxial compression. The term $\gamma$ is a function of the constant $K_c$ and can be evaluated by Equation 15.

$$\gamma = \frac{3(1-K_c)}{2K_c-1} \quad \text{(Eq. 15)}$$

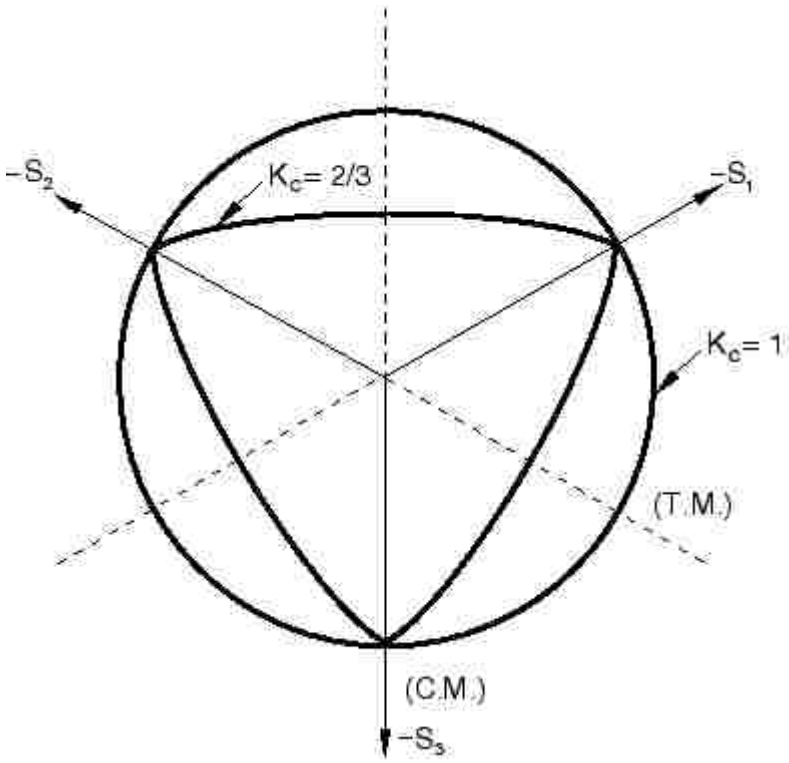


Figure 4.16 - Yield Surface of the CDP in the Deviatoric Stress Space (Dassault Systems, 2010)

The model is defined in the software by a set of tables describing the uniaxial behavior of the concrete in tension and compression and a series of five parameters used to describe the behavior in a multiaxial stress state, namely ψ, $\varepsilon$, $^{f_{b0}}/_{f_{c0}}$, κ, and ν. A key benefit of the CDP model is that these parameters have a specific physical interpretation. The dilation angle, ψ, is interpreted as the internal friction angle and is typically taken at 36° or 40° (Kmiecik & Kaminski, 2011). It was taken as 36° for the development of this model. The *plastic potential* eccentricity, $\varepsilon$, can be calculated as the ratio of the tensile strength to the compressive strength and alters the shape of the plastic potential curve in meridional plan (deviatoric stress vs. pressure), where an eccentricity of zero results in a straight line, corresponding to the Drucker-Prager criterion. The default value of 0.1 was adopted for the development of this model. $^{f_{b0}}/_{f_{c0}}$ is simply the ratio of the concrete strength under biaxial compression to the concrete strength under uniaxial compression, for which a value of 1.25 was adopted. κ is simply the constant $K_c$, described above, that

is used to determine $\gamma$ for cases of triaxial compression. For this a value of 0.7 was adopted based on the work of (Yu, Teng, Wong, & Dong, 2010). Lastly, a viscosity parameter, ν, can be entered to allow the material to temporarily exceed the plastic potential surface in order to handle convergence issues in some cases. The viscosity parameter should be kept to a minimum or set at zero, when model stability allows, or otherwise minimized in order to avoid unnecessary error. A small value of 0.002 was selected to improve stability in the model.

As previously mentioned in this section, the CDP model requires tables to be input describing the uniaxial behavior of the concrete. For compression these tables take the form of a stress vs. plastic strain table and an optional compressive damage vs. plastic strain table. The later was left blank in this study due to a lack of cyclic material testing and its implementation being largely unnecessary due to the monotonic loading imposed in this model. Similar tables exist for the tensile behavior, although Abaqus does allow for the tensile behavior to be alternatively defined on the basis of stress vs. displacement or based on a fracture energy formulation. For the purpose of this study, the tensile stress vs. plastic strain method was implemented.

**4.6.1.1. Compression stress-strain relationship.** For the purpose of this study, the compressive stress vs. strain relationship was derived based on the Hognestad relationship (Hognestad, 1951) in which the first portion of the constitutive relationship is described by a parabola given in Equation 16.

$$f_c = f''_c \left[\frac{2\epsilon_c}{\epsilon_0} - \left(\frac{\epsilon_c}{\epsilon_0}\right)^2\right] \quad \text{(Eq. 16)}$$

where $\epsilon_c$ is the strain and $f_c$ is the stress at a given point in the relationship. The term $\epsilon_0$ is the strain at the apex of the parabola and is taken as 1.8 times $f''_c$ divided by the concrete modulus of elasticity. $f''_c$ is taken as a reduction of the compressive strength of concrete cylinders $f'_c$, generally on the order of 85% to 90% of $f'_c$, in order to account for differences between cylinder strength and member strength. These differences occur due to the relatively fast loading rate of test cylinders, vertical migration of bleed water, and variation in where/how the concrete is cured. In the case of this study, the migration

of bleed water is expected to result in a reduced water-to-cement ratio at the location of the plastic hinge, and the loading was applied relatively quickly. As such $f"_c$ was taken as $f'_c$ in the material inputs. As seen in Table 3.2, the nominal 28 day compressive strength varied between the columns utilized in the test. Additionally, in the case of Calt-2 the compressive strength at the time of testing was less than that at 28 days. This brings a level of uncertainty to the value of $f'_c$ obtained experimentally. As a result the design value for the compressive strength of the concrete, 5,000 psi (34.5 MPa), was assumed for use in the finite element model.

The value of the concrete elastic modulus was taken based on Equation 17, which is permitted by the ACI 318 code (2014).

$$E_c = 57{,}000\sqrt{f'_c} \qquad \text{(Eq. 17)}$$

The second portion of Hognestad relationship is described by a linear relationship extending from the apex of the parabola to the limiting strain of 3,800 microstrain. During this portion of the relationship, the stress decreases linearly by 15%.

The model inputs differ from Hognestad's distribution in five key ways. Firstly, as the concrete is passively confined by the spiral reinforcement, the ultimate compressive strain is dramatically increased to approximately 7,600 microstrain. This is so that the model more accurately represents the more ductile behavior of the confined concrete. This effect is illustrated for hoop-confined concrete in the relationship proposed by Mander et al. (1988). For the purpose of this study, double the strain limit of 3,800 microstrain, as proposed by Hognestad, was utilized for a value of approximately 7,600 microstrain. This closely resembles the limit shown in (Yu, Teng, Wong, & Dong, 2010). Additionally, two stages were added to the stress strain behavior. The first is a rapid decrease in stress to a value of 700 psi (4.8 MPa) between plastic strain values of 8,000 microstrain and 8,790 microstrain. From there, it continues at this final stress value indefinitely. The fourth variation is to provide for a longer period of linear behavior in the model, the initial compressive stress-strain relationship is held linear up to a value of stress of 3,200 psi (22.1 MPa). Lastly, to aid in model convergence, the transitions between the various stages of the stress-strain relationship are subjectively blended. This

blending pushes the strain corresponding to peak stress from a strain of 2230 microstrain, as suggested by Hognestad, to 2670 microstrain. The result is a stress-strain relationship that approximates the Hognestad relationship but is distinctly different, as can be seen in Figure 4.17.

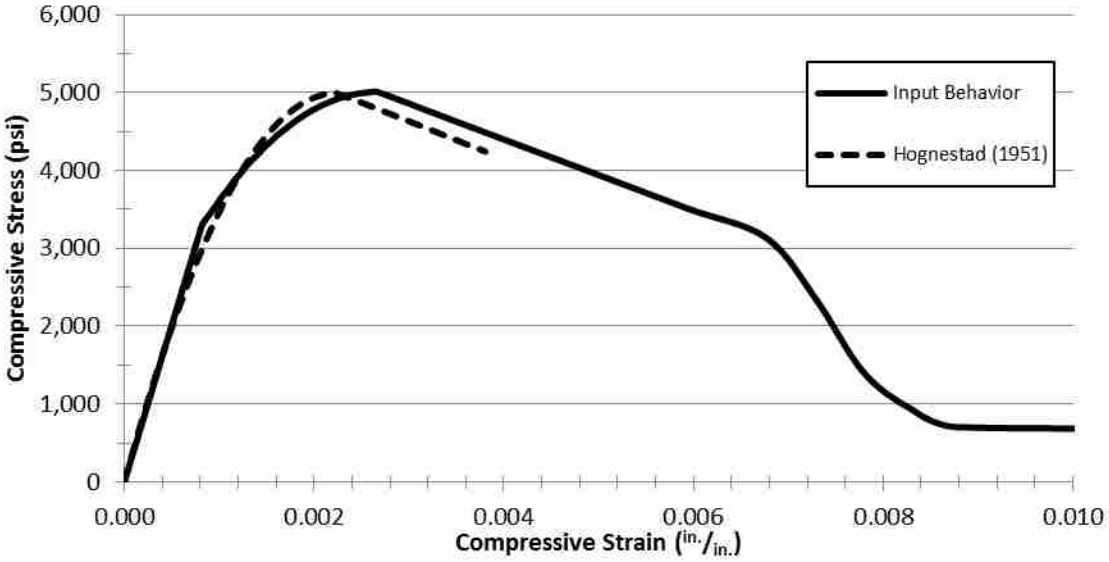


Figure 4.17 - Input Compressive Stress-Strain Relationship Compared to the Hognestad Relationship (1951) (1 psi = 0.00689 MPa, 1 in./in. = 1 mm/mm)

To verify the compression behavior of the concrete material model, a series of small finite element models were created. In these models a 1 in. (25 mm) cube was meshed with 64 regular hexahedral elements and subjected to an axial displacement. Two transverse faces, adjacent to one another, were constrained with symmetry constraints, and the remaining two faces were loaded with various levels of pressure to simulate active confinement. The resulting model is analogous to a 2 in. (50 mm) by 2 in. (50 mm) by 1 in. (25 mm) regular hexahedron compressed about the short (axial) dimension. Stress, in the axial direction, was extracted from a central node along the edge that divides the two symmetry constrained faces and compared to the nominal strain. The resulting stress-strain relationship without any active confining stress is compared to the

model inputs in Figure 4.18. Here it can be seen that the small amount of passive confinement provided by the surrounding material, due to poisson's effect, increased the peak stress by approximately 20%. The effect of active confinement pressure, as illustrated in Figure 4.19, is even more pronounced.

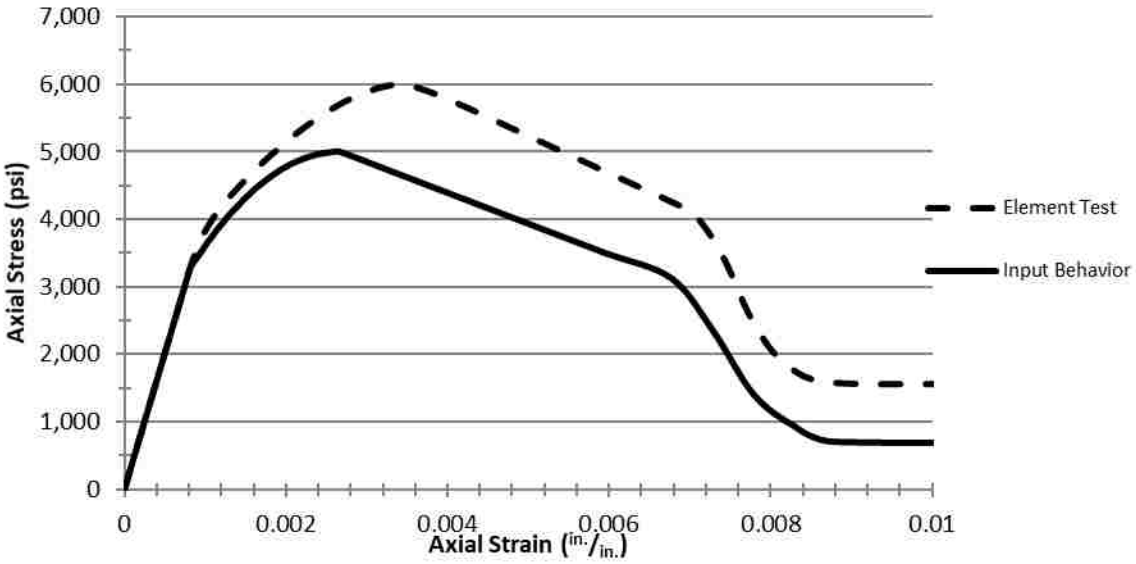


Figure 4.18 - Element Test Results Compared to Model Inputs
(1 psi = 0.00689 MPa, 1 in./in. = 1 mm/mm)

**4.6.1.2. Tensile stress-strain relationship.** The stress vs. plastic strain relationship utilized in this study was greatly simplified with the objective of reducing computation demands. The magnitude of the tensile forces in the concrete are anticipated to be negligible relative to the tensile forces in the longitudinal reinforcement. As a result the inputs were greatly simplified. The tensile stress increases linearly to a value of 1.0% of $f'_c$, then increases linearly to a value of 1.1% of $f'_c$ over the next 10 microstrain, and finally remains at a constant 1.1% of $f'_c$. This can be seen in Figure 4.20.

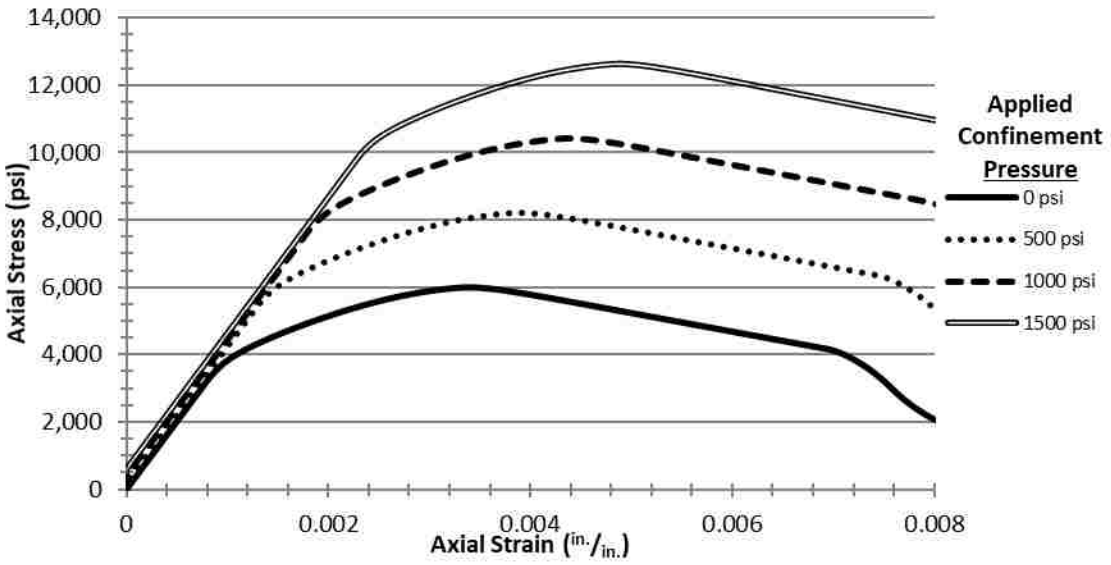


Figure 4.19 - Influence of Active Confinement Pressure on Material Model Response (1 psi = 0.00689 MPa, 1 in./in. = 1 mm/mm)

It is noted that this increase and plateau in tensile stress with increasing strain is not realistic. In reality tensile stress increases relatively linearly until it reaches the tensile strength of the concrete, at which point a fracture process zone forms in the vicinity of the peak stress. The result of the fracture process zone is a rapid decrease in tensile stress with increased elongation until a crack is fully formed and the tensile stress ceases to exist.

The sudden decrease in tensile stress that exists in reality can cause stability issues in the simulation. This is due in part to interactions between the stiffness matrix and the constraint equations governing the interaction between the multiple bodies, where during the process of obtaining a converged constraint between bodies the impact by the body interactions may become invalid forcing reassessment of the stiffness matrix and reiteration of the constraints. As a result, the solver may take additional iterations within a given increment. This can lead to the number of increments exceeding the limits set by the solver, resulting in an aborted solution. For this reason, the tensile stress-strain relationship was set to minimize sudden changes in secant modulus with increased elongation.

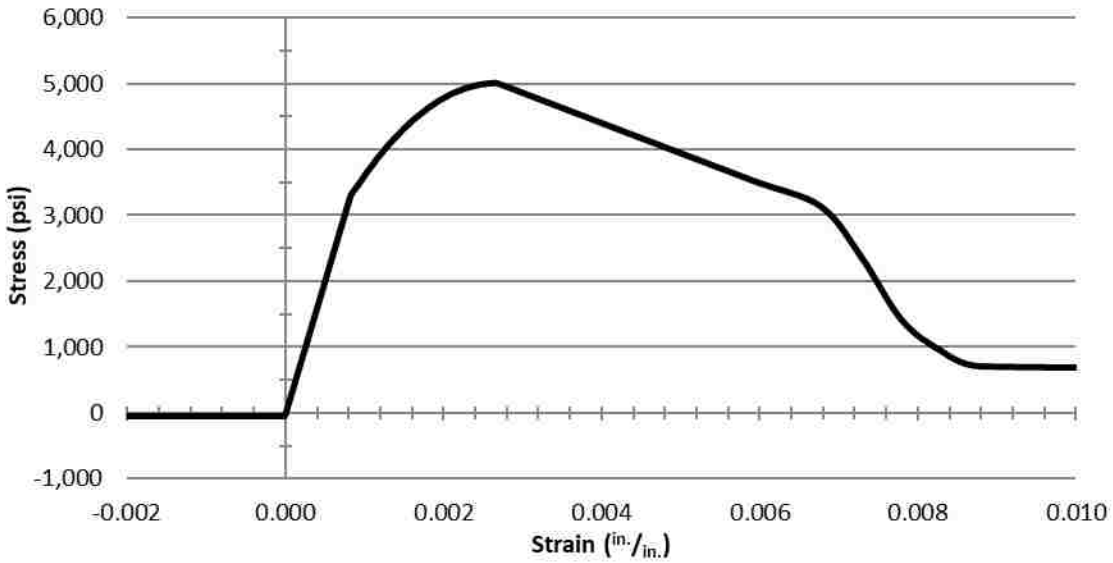


Figure 4.20 - Input Uniaxial Stress-Strain Relationship for Concrete Material
(1 psi = 0.00689 MPa, 1 in./in. = 1 mm/mm)

**4.6.2. Steel Reinforcement.** The steel reinforcing bars were modeled using the classical metal plasticity model in Abaqus using the Mises yield surface, which provides an isotropic yield surface. A table of stress vs. plastic strain are entered to define both the initial yield point and the hardening behavior. A yield strength of 60 ksi (420 MPa) was utilized in the development of the material inputs, despite the higher values shown in Table 3.3. This was done in part due to uncertainty in the reported values, as discussed in the previous section, and also due to the size effect associated with testing a smaller volume of material relative to that represented within the model. Insufficient data were available to quantify this size effect on a statistical basis, and as such the minimum tensile yield strength, specified by ASTM A706, of 60 ksi (420 MPa) was adopted.

For the purpose of this study, the behavior of the reinforcing steel was simplified as an effectively elastic-perfectly plastic behavior. The inputs are based on a linear elastic response up to yielding and a constant stress from the point of yielding to the ultimate strain, with the exception of modifications made at the elastic-to-plastic transition point to assist convergence. These alterations at the elastic-to-plastic transition consisted of a gradual change in stiffness to aid in convergence, which results in the peak

response that is slightly higher than the desired yield stress of 60 ksi (420 MPa) by 4.2%. Beyond the ultimate strain, a sharp decrease in stress is input, to account for fracture, and will result in a concentration of plastic strain during simulation. At 1000 microstrain past the ultimate strength the stress is reduced to 85% of ultimate strength, at an additional 1000 microstrain past ultimate strength the stress is reduced to 30% of the ultimate strength, and finally after an additional 1000 microstrain beyond the ultimate strength the stress is reduced to 15% of ultimate, as shown in Figure 4.21. Sudden changes in tangent stiffness were avoided to prevent numerical issues, and as a result smooth transitions were implemented at transitions.

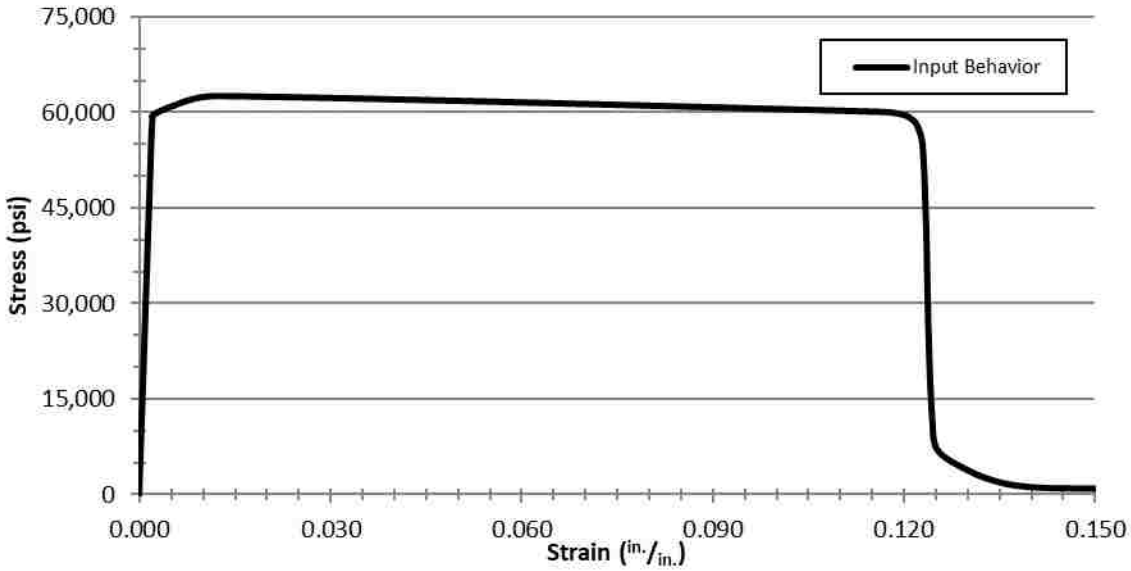


Figure 4.21 - Input Stress-Strain Relationship for Reinforcement
(1 psi = 0.00689 MPa, 1 in./in. = 1 mm/mm)

## 4.7. SOLUTION SETTINGS

As the modeling outlined in this thesis is subject to geometric nonlinearities, material nonlinearities, and interactions between several bodies it was necessary to modify the solution and convergence settings in Abaqus CAE from their defaults in order

to obtain a solution. This was done cautiously and only when necessary, as such these settings vary between the various loading steps, outlined in Section 4.5.2.

For the first two steps, where the boundary conditions are set and where the axial load applied, the solver defaults are adopted. In the subsequent steps the values of $I_0$ and $I_R$ are increased from 4 to 8 and from 8 to 10, respectively. $I_0$ represents the number of equilibrium iterations allowed. After which the solver checks to ensure that the residuals are not increasing in two consecutive iterations. As the model is subject to multiple interactions of nonlinear materials, the convergence is expected to be nonmonotonic, require an increase in $I_0$ compared to the defaults. $I_R$ is the number of equilibrium iterations after which the rate of convergence check is performed. The default value is 8. In cases where convergence is nonquadratic and this cannot be corrected by using the unsymmetric equation solver for the step, the logarithmic convergence check should be eliminated by setting this parameter to a high value. As the flow potential for the concrete material model adopted is asymmetric, the unsymmetric equation solver is required, the only a higher value of $I_R$ is applicable to correcting convergence rate issues. The value of 10 was adopted as it is the recommended value for discontinuous analyses.

In both cases higher values, up to an order of magnitude greater, were tested to try to alleviate convergence issues related to the Calt-3 model and repaired column models. Additionally, the solution control parameters for field equation tolerances were also increased, up to an order of magnitude beyond their defaults, in an attempt to alleviate convergence issues. These attempts had no impact on the ability of the models to converge, and thus only default control parameters were utilized in the models discussed in this study.

Additionally, both the length of the step and the incrementation settings were varied to effectively control the discretization of the application of loads and displacements. That is to say that a step, in which loads and displacements have been prescribed, is broken into a series of increments such that the loads and/or displacements are not applied all at once. Instead the model is solved at many points between the state at the beginning of the step and the final state commanded at the end of the step. This incrementation can be fixed or varied automatically by the solver, such that when a converged solution cannot be obtained for a given increment the solver will retry with a

progressively smaller increment until a converged solution can be met. The step lengths and incrementation settings are outline in Table 4.4.

Table 4.4 - Step Incrementation Settings

| Step | Step End Point End Point | Step Length | Incrementation | | |
|---|---|---|---|---|---|
| | | | Initial Increment | Max Increment | Min Increment |
| 1 | Initial State* | N/A* | N/A* | N/A* | N/A* |
| 2 | Axial Load Applied | 1 | 1 | 1 | 1.0E-05 |
| 3 | CP-1 | 1 | 0.001 | 0.002 | 1.0E-10 |
| 4 | CP-2 | 1 | 0.001 | 0.002 | 1.0E-15 |
| 5 | CP-3 | 1 | 0.001 | 0.002 | 1.0E-15 |
| 6 | CP-4 | 1 | 0.001 | 0.002 | 1.0E-15 |
| 7 | CP-5 | 6 | 0.005 | 0.005 | 0.005 |

* The initial step is set up by the solver and is used to define the boundary constraints defined in Section 4.5.1 and the interactions defined in Section 4.5.3.

In all steps the direct linear equation solver was utilized. This utilizes Gaussian elimination to solve the system equations at each increment. This is done in conjunction with an asymmetric matrix storage, which is necessitated by the non-associated flow rule assumed in the concrete material model, detailed in Section 4.6.1, that is to say the plastic potential is not equal to the yield function. Newton's method is utilized to handle the nonlinearities of the solution wherein, prior to each increments solution the residual load vector, taken as the difference of the internal element loads and external loading, then a linear solution is performed with the residual loads and convergence checks performed. If convergence is not met, the stiffness matrix is updated, the residual loads reevaluated, and a new solution obtained. This iteration continues until the solution converges. Details of the implementation of these methods and solution techniques in the software are available in the (Abaqus Theory Manual, 2010).

## 4.8. DISCUSSION OF ERRORS

There are a variety of errors that are inherent in the process of simulating the real physical response of a system. These errors can provide context to the results and can be categorized into two broad categories. The first category includes errors of idealization that contains the various errors inherent in the construction of the numerical model. The second includes errors of discretization that contains the errors resulting from discretization of the model and solution of the model. The following sections discuss these two types of errors as they pertain to this numerical study.

**4.8.1. Errors of Idealization.** These errors can be understood as those errors associated with assumptions made during the development of a finite element model, that is to say these are the errors associated with conceptualization. The remainder of this section will discuss some key errors of this type as they pertain to this study.

A large number of errors of this type exist in the way the experimental data were interpreted for the development of this model. For the purpose of this model, it was assumed that the entirety of the deformation measured during the experiment was accumulated in the span of the column from the base of the cap to the top of the footing. This is inherently false as the measurements are not only a function of the deformation in the test specimen, including the cap and footing, but also any deformation in the test fixture and any slippage or freeplay in the test fixture. While the majority of deformation is in the area being simulated, each experimentally obtained value also includes a component of deformation from the rest of the test assembly. Thus, at any prescribed displacement based on experimental measurement applied to the model should be expected to result in a model response corresponding to a slightly higher displacement on the physical specimen. As a result, this error resulting from the scope of the domain is expected to result in a stiffer behavior within the elastic regime of the columns response.

An additional error, expected to produce a stiffer behavior in the simulated column response, is induced by the quasi-static modeling approach discussed in Section 4.5.2, wherein the cyclic behavior of the experimental column is compared to a simulated load-deformation response of a column that is progressively deformed. As such, no effects of cyclic loading and unloading, multiple cycles at the same

load/displacement level, and reversed loading are accounted for in the simulated response.

Similarly, the direction in which the measured actuator deflections are assumed to act imparts additional error. The measured deflections are assumed to act purely in the direction of primary loading. However, this is almost certainly not the case as some of the measured deflection is due to transverse and/or vertical drift. Thus, by imposing this measured total deflection as a single component of deflection in the model, the model experiences a greater total deflection than was imposed. As a result of this error the model would be expected to produce a response corresponding to a greater measured deflection than that which was applied.

Other errors of idealization pertain to the various material constitutive relationship utilized in this model. These material models are discussed in more detail in Section 4.6. As note previously, this study utilizes design value approximations of the material properties applied to the material models contained within Abaqus. Both of these facts introduce error into the model. Some error is the result of difference between the assumed design values and the actual properties of the materials utilized in the experiment. Further error is introduced by limitations of the material models themselves. That is to say the material models are not perfect. As pointed out by others (Yu, Teng, Wong, & Dong, 2010), all numerous studies utilizing concrete plasticity models have utilized various, and often considerably different, yield criteria, hardening rules, and/or plastic flow rules in their simulation of concrete. These studies often show similarly 'good' results despite these variations. (Yu, Teng, Wong, & Dong, 2010) went on to argue that these results provide only the necessary but not sufficient evidence for the accuracy and reliability of the proposed models. That is to say that while the studies show good agreement within the scope of which the constitutive relationship was tested, it does not imply robustness for cases outside the verified range of applicability. Their study went on to conclude that, among other things, a concrete material model ought to include a yield criteria that includes the impact of the third deviatoric stress, a hardening/softening rule that is a function of the confining pressure, a damage variable that is a function of the confinement, and a flow rule that is a function of both the magnitude and rate of confining pressure. While the concrete damaged plasticity model in Abaqus does

account for the third deviatoric stress in its yield criteria, thereby accounting for variations in shear strength between biaxial and triaxial compression, it does not factor the confining pressure into its formulation of its hardening rule, its flow rule, and its damage variables. As such the model can only approximate the behavior of concrete under active and passive confinement to the limits of its formulation.

Similarly, the isotropic plasticity model utilized to represent the steel reinforcing bar cannot account for the Bauschinger effect via kinematic or mixed mode hardening. As this model was developed to simulate the quasi-static behavior of the columns, this simplification is assumed to be negligible but does limit this model's applicability to other situations. The impact of these limitations are more difficult to quantify, and the inputs, outlined in Section 4.6, are intended to mitigate these errors. A complete discussion of errors and limitations associated with the material models utilized is beyond the scope of this study.

**4.8.2. Errors of Discretization.** These errors can be understood as those errors associated with the numerical interpretation of the model. These are the errors associated with discretization of the domain and those associated with the solution method. These are most commonly associated with the mesh of the model and can generally be attributed to having an insufficient number of degrees of freedom to appropriate characterize the domain and solution over the domain.

For the purpose of this study an appropriate mesh was established by first determining an appropriate meshing method and element types, as described in Section 4.4. The suitability of the elements is often governed by their compatibility with the various material models and solvers available in Abaqus.

The appropriate level of refinement was determined by creating a baseline mesh for the model. This model is then loaded and constrained according to its intended purpose. For this study the displacement controls utilized in the Calt-1 model were implemented for determining an appropriate mesh. The material models were then simplified to a linear elastic model for reduced computational demand. Lastly this mesh model was run with increasing level refinement, achieved by increasing the number of elements. Typically, the resulting error in the energy norm would then be examined until it reached a suitably low level. However, this value cannot be established for a mesh that

contains beam elements, and thus this method could not be implemented. In lieu of this, a sample response, in this case total reaction force at the control point, was extracted and compared to the total model variables, i.e., the number of degrees of freedom in the mesh plus lagrangian multipliers. This is shown in Figure 4.22. This shows a suitably stable response, with the last three levels of refinement resulting in only a 0.42% change in reaction force with an 87% increase in total model variables. This resulted in a nominal beam element length of 2.5 in. (63.5 mm) and 3.0 in. (76.2 mm), for the longitudinal and transverse reinforcement, respectively. Similarly, the edge seed size for the solid mesh representing the concrete was selected as 1.5 in. (38.1 mm) as a result of this mesh sensitivity study.

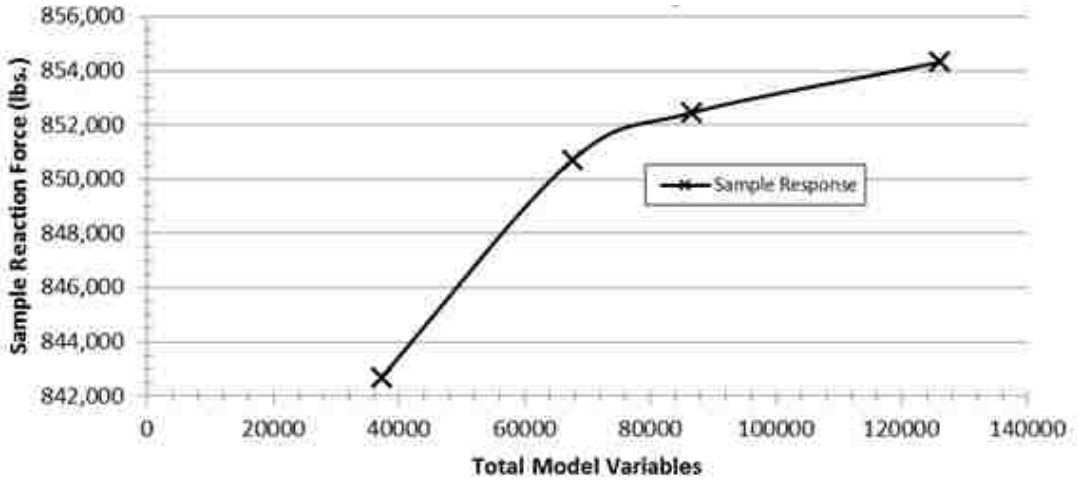


Figure 4.22 - Sample Response of Mesh Evaluation Model (1 lb = 0.445 kN)

Another error of discretization is associated with the solution method employed. That is to say the incremental-iterative nature of the solver, as discussed in Section 4.7, results in an error. Similar to how the number of degrees of freedom are associated with the discretization error of the mesh, the incrementation over a given step dictates the discretization of the solver. While Abaqus contains methods for automatically adjusting increment size to reach a suitable level of convergence, these were found to be ineffective for this model and often led to excessive iterations and an inability to converge in

subsequent increments. As a result, a suitably small fixed increment size was set for each step. This increases the computational demand, as a small increment size must be fixed in portions of a step where it is not necessary, but was found to be necessary for this study. These are outlined for the various load steps in Table 4.4, where the control points are defined in Table 4.1, Table 4.2, and Table 4.3 for the columns Calt-1, Calt-2, and Calt-3, respectively.

## 4.9. DISCUSSION OF RESULTS

The results of the finite element model's predicted response of the original columns, Calt-1, Calt-2, and Calt-3 as compared to the response observed during the physical testing, are presented in this section.

**4.9.1. Results of Calt-1 Finite Element Model.** Results are presented within this section and are compared to the experimental backbone curves presented in Section 4.5.2.1. Figure 4.23 presents the base shear-to-displacement relationship predicted by the model, Figure 4.25 presents the torque-to-twist relationship predicted by the model, and Figure 4.26 presents the corresponding torque-to-moment ratio against the drift of the cap.

The base shear-to-displacement relationship predicted by the model is in relatively good agreement with the experimental results. As expected, due to a number of the errors discussed in Section 4.8, the model initially predicts an overly stiff response. This is likely due to compliance in the physical test setup and other displacement not associated with deformation of the column that is not reflected in the measured values. This overly stiff response continues up to the peak base shear capacity predicted by the model, of 82.2 kip (366 kN), at a displacement of 3.0 in (76.2 mm). Thereafter the experimental backbone curve exceeds the model prediction as it continues to its higher peak value of 87.7 kip (390 kN).

It is worth noting that the base shear from the model is taken as the sum of both the reaction forces and concentrated forces at the control point. The reaction forces are those which result from the applied displacement, and the concentrated forces are those which result from the applied axial load. As the column in the model deflects the axial load remains parallel to the centerline of the column at the cap, and as a result the

corresponding concentrated forces act to oppose the reaction forces. While this sum more accurately depicts the applied loading in the model, the reaction forces are a better analog of the actuator loads to which the model is being compared. The peak reaction force of 86.5 kips (385 kN) is reached at a slightly greater displacement of 3.16 in. (80.3 mm) and better matches the experimental results. Both measures, either the model reaction force value or the sum of reaction forces and concentrated forces, are imperfect compared to the physical experiment as the former neglects the influence of the prestressing tendons, and the later neglects the forces resulting from the prestressing tendons acting along the height of the model. As such the two values effectively bound the solution, and both show good agreement with the experimental results for peak base shear.

Additionally, the shape of the predicted base shear to displacement relationship is in good agreement with the experimental results, with the predicted base shear value being within 15% of the measured value for the first 11 in. (279 mm) of displacement. However, the model response is excessively ductile with a sudden loss of capacity not occurring until a cap displacement of approximately 13.5 in. (343 mm), while the physical test specimen lost a substantial amount of capacity during the hysteric cycling corresponding to the D10 peak value at a displacement of approximately 10.7 in. (272 mm). While some of this lost capacity may be due to the cyclic nature of the test, it is worth noting that most of the errors of idealization discussed in Section 4.8.1 would tend to cause the physical specimen to fail at higher measured displacements, as a number of unattributed sources would be adding to the measured displacements.

Unfortunately, the torque to twist relationship was not as well predicted. As expected, due to a number of the errors discussed in Section 4.8, the model initially predicts an overly stiff response. However, the torque response suddenly plateaus off at a torque of 33.8 kip-ft (45.8 kN-m) at a twist of only 0.06 degrees. This is before the first displacement step, which ends in the imposed displacements of CP-1 in Table 4.1. Examining the von mises stresses in transverse reinforcement through the end of this step indicates stresses never exceeded 8.42 ksi (58.1 MPa), as shown in Figure 4.24.

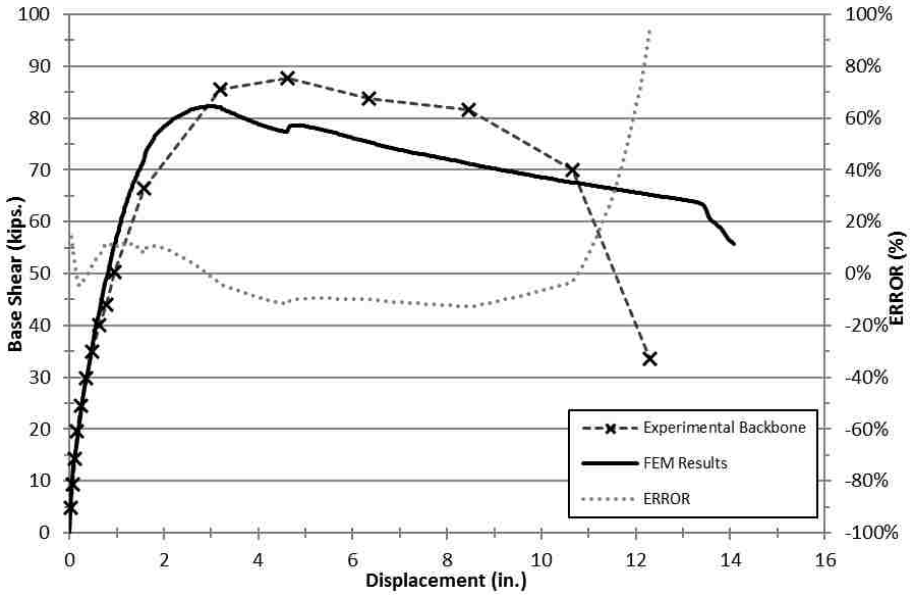


Figure 4.23 - Calt-1 Model Results | Base Shear-to-Displacement
(1 kip = 4.448 kN, 1 in. = 25.4 mm)

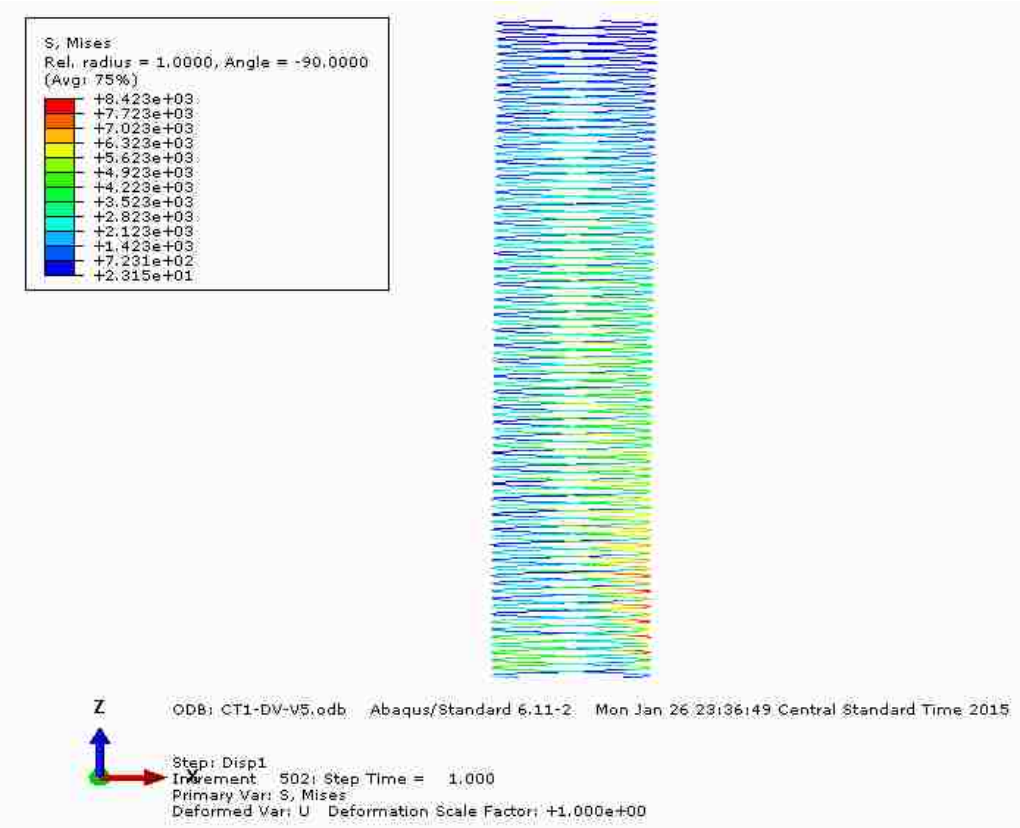


Figure 4.24 - Calt-1 Transverse Reinforcement | Von Mises Stress |
At CP-1 Displacements

This indicates that the issue is not due to premature yielding of the transverse reinforcement elements but rather an issue with transfer of load to the transverse reinforcement, within the framework of the model. This poor prediction of one aspect of the model's response, namely the torque-to-twist relationship, may have a wider reaching impact as the overall model response, and physical response of the columns, are not independent. It has been shown in (Prakash, Li, & Belarbi, 2012) that the shear, bending, and torsional capacity of columns are related. As such, inaccurate torque-to-twist response would be expected to impact the base shear-to-displacement response as well, thereby inducing error. However, the model's torque-to-twist response deviates from the experimental results early on, and no corresponding change in behavior can be observed in the base shear-to-displacement response of the model. As a result, it is unclear what impact the erroneous torque-to-twist response has on the base shear-to-displacement relationship.

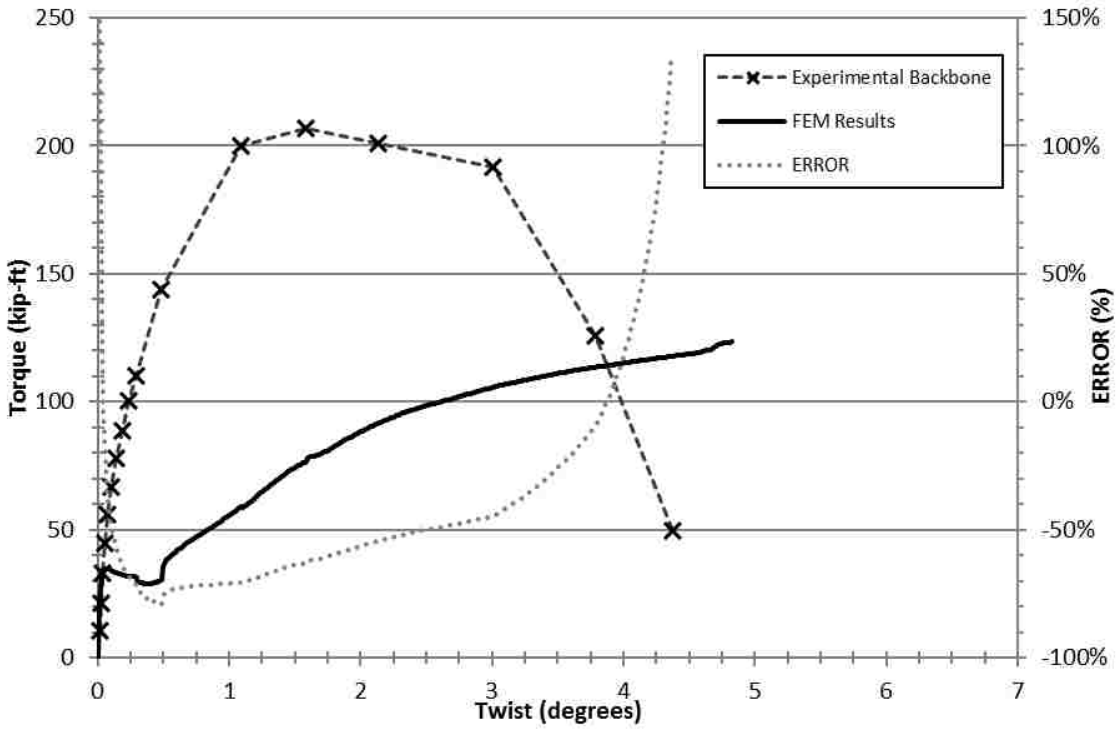


Figure 4.25 - Calt-1 Model Results | Torque-to-Twist (1 kip-ft = 1.356 kN-m)

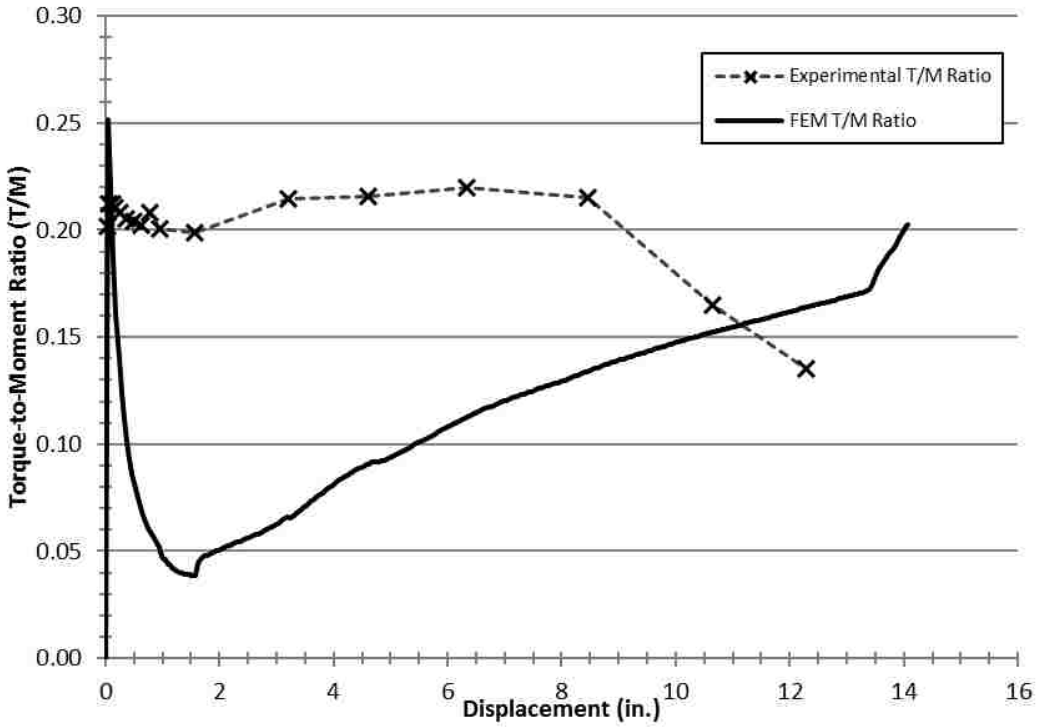


Figure 4.26 - Calt-1 Model Results | Torque-to-Moment Ratio (1 in. = 25.4 mm)

**4.9.2. Results of Calt-2 Finite Element Model.** Results are presented below and compared to the experimental backbone curves presented in Section 4.5.2.2. Figure 4.27 presents the base shear-to-displacement relationship predicted by the model, Figure 4.28 presents the torque-to-twist relationship predicted by the model, and Figure 4.29 presents the corresponding torque-to-moment ratio against the drift of the cap.

The base shear-to-displacement relationship predicted by the model is in relatively good agreement with the experimental results. As expected, due to a number of the errors discussed in Section 4.8, the model initially predicts an overly stiff response. This is likely due to compliance in the physical test setup and other displacement not associated with deformation of the column that is not reflected in the measured values. This overly stiff response continues up to the peak base shear capacity predicted by the model, of 75.7 kip (336.6 kN), at a displacement of 3.41 in (86.7 mm). This overly stiff response continues to failure, which occurs at a displacement of 6.35 in (161.3 mm) at base shear load of 64.5 kip (286.9 kN). This is in good agreement with the experimental

results at the nearest experimental control point, corresponding to D4 in Table 4.2, where the measured response was 64.2 kip (285.4 kN) at a displacement of 6.32 in (160.4 mm).

It is worth noting that the base shear from the model is taken as the sum of both the reaction forces and concentrated forces at the control point. The reaction forces are those which result from the applied displacement, and the concentrated forces are those which result from the applied axial load. As the column in the model deflects the axial load remains parallel to the centerline of the column at the cap, and as a result the corresponding concentrated forces act to oppose the reaction forces. While this sum more accurately depicts the applied loading in the model, the reaction forces are a better analog of the actuator loads to which the model is being compared. The peak reaction force of 81.0 kips (360.2 kN) is reached at a slightly greater displacement of 3.80 in. (96.6 mm). Both measures, either the model reaction force value or the sum of reaction forces and concentrated forces, are imperfect compared to the physical experiment as the former neglects the influence of the prestressing tendons, and the later neglects the forces resulting from the prestressing tendons acting along the height of the model. As such the two values effectively bound the solution, and both are in reasonable agreement with the experimental results for peak base shear.

Additionally, the shape of the predicted base shear to displacement relationship is in reasonable agreement with the experimental results, with the predicted base shear value being within a maximum of 37.6% of the measured value. However, the peak error occurs relatively early on and begins to decrease at displacements greater than 1.6 in (40.7 mm), and decreases below 20% before peak displacement shear occurs. The error continues to decrease for the remainder of the simulation.

As with Calt-1, the torque-to-twist response degraded prematurely. This began at a torque of approximately 77.8 kip-ft (105.5 kN-m) and a twist of approximately 0.1 degree. Unlike Calt-1, the torque response did not initially drop. Instead the tangent stiffness suddenly degraded. The predicted torque response gradually increased with displacement until failure.

As noted in Section 4.9.1, the influence of increased torsional loading should be a decrease in both the flexural and shear capacities of the column. Neither the Calt-1 nor Calt-2 models accurately predicted the torque-to-twist response observed, and thus the

validity of the simulated torque influence on flexural capacity is questionable. It is worth nothing that the model does predict a reduced flexural capacity with the increased twist imposed on Calt-2. The Calt-2 peak base shear, 75.7 kip (337 kN), is reduced by approximately 8% compared to the Calt-1 peak base shear of 82.2 kip (366 kN). While this shows that the model correctly predicts a diminished flexural capacity, it does not predict the magnitude of this decrease well. The Calt-2 measured peak base shear of 64.2 kip (285.4 kN) represents a decreased capacity of approximately 27% when compared to the Calt-1 measured peak base shear of 87.7 kip (390 kN). This inability to accurately reproduce the reduced flexural capacity with increased torque/twist is believed to be a symptom of the model's inability to accurately predict the torque-to-twist response.

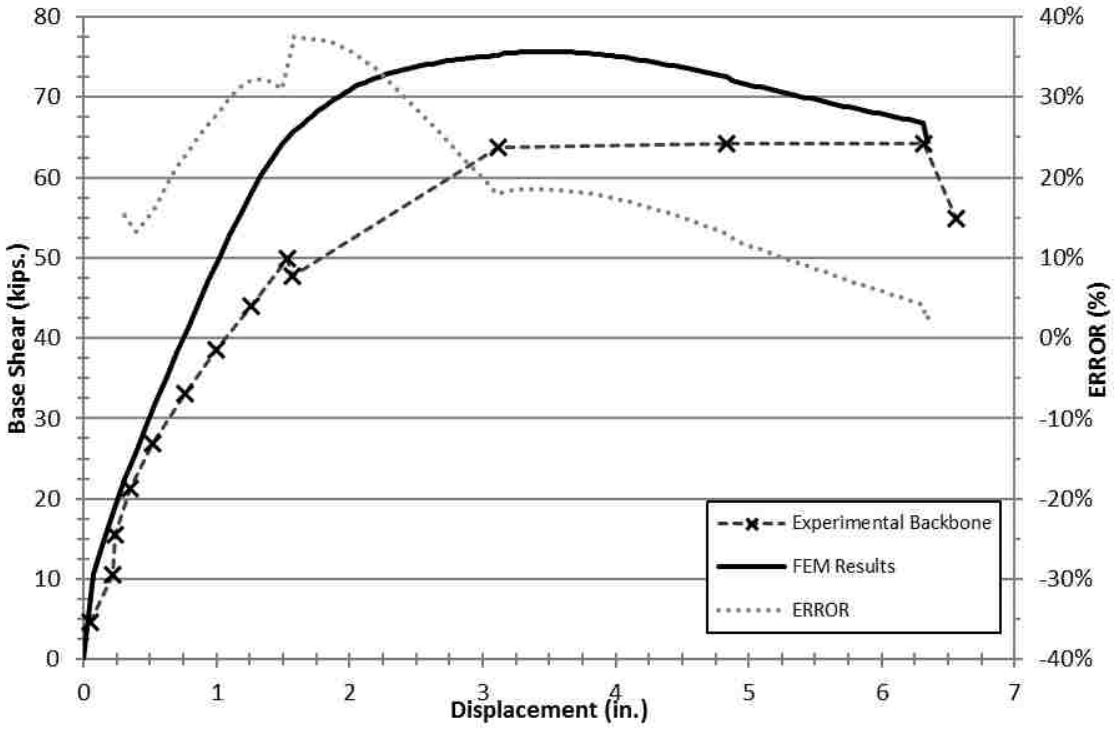


Figure 4.27 - Calt-2 Model Results | Base Shear-to-Displacement
(1 kip = 4.448 kN, 1 in. = 25.4 mm)

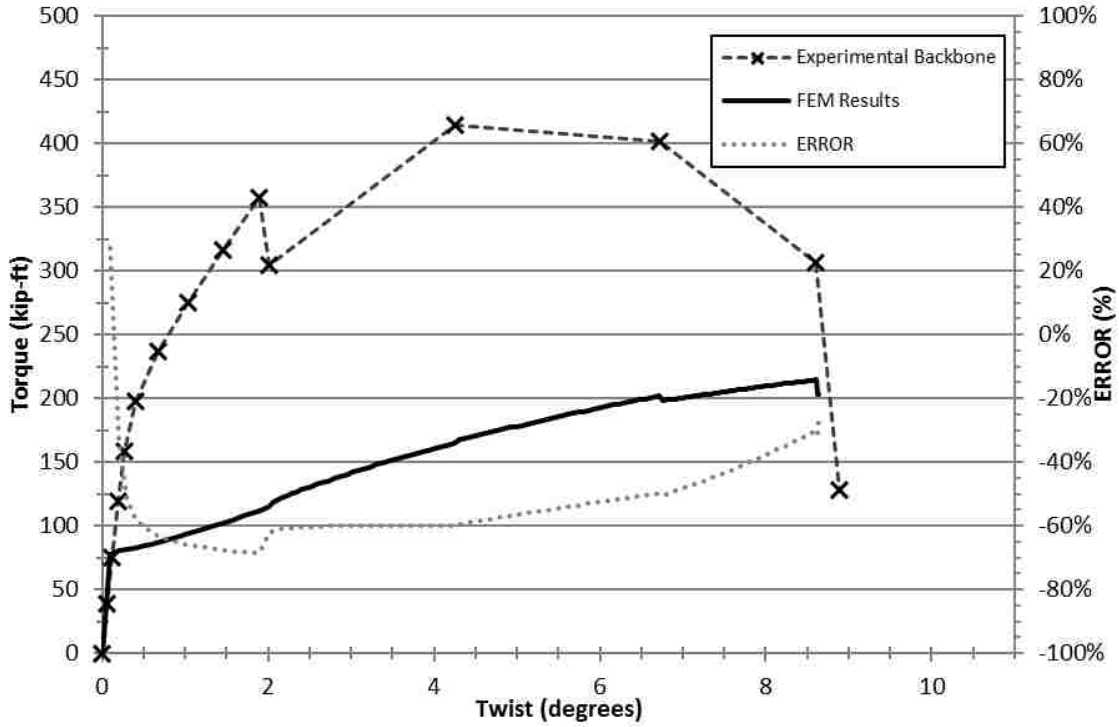


Figure 4.28 - Calt-2 Model Results | Torque-to-Twist (1 kip-ft = 1.356 kN-m)

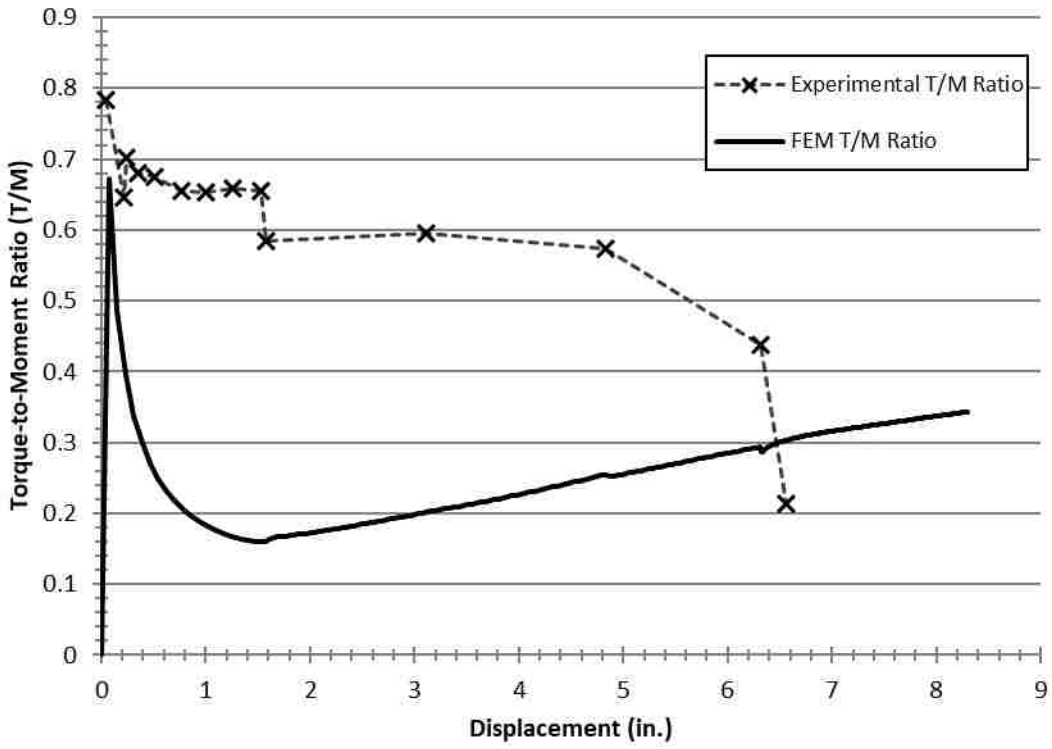


Figure 4.29 - Calt-2 Model Results | Toque-to-Moment Ratio (1 in. = 25.4 mm)

**4.9.3. Calt-3 Finite Element Modeling.** The model used for Calt-3 was unique from either Calt-1 or Calt-2 in that it was loaded 35 degree off the strong axis, as opposed to across the weak axis. As such all bodies in the Calt-3 model were rotated 55 degrees, such that X-axis in the model was oriented 35 degrees off the model's strong axis.

Results of Calt-3 finite element model are presented below and compared to the experimental backbone curves presented in Section 4.5.2.3. Figure 4.30 presents the base shear-to-displacement relationship predicted by the model, Figure 4.31 presents the torque-to-twist relationship predicted by the model, and Figure 4.32 presents the corresponding torque-to-moment ratio against the drift of the cap. The Calt-3 model resulted in convergence failure at a base displacement of 1.27 in (32.3 mm).

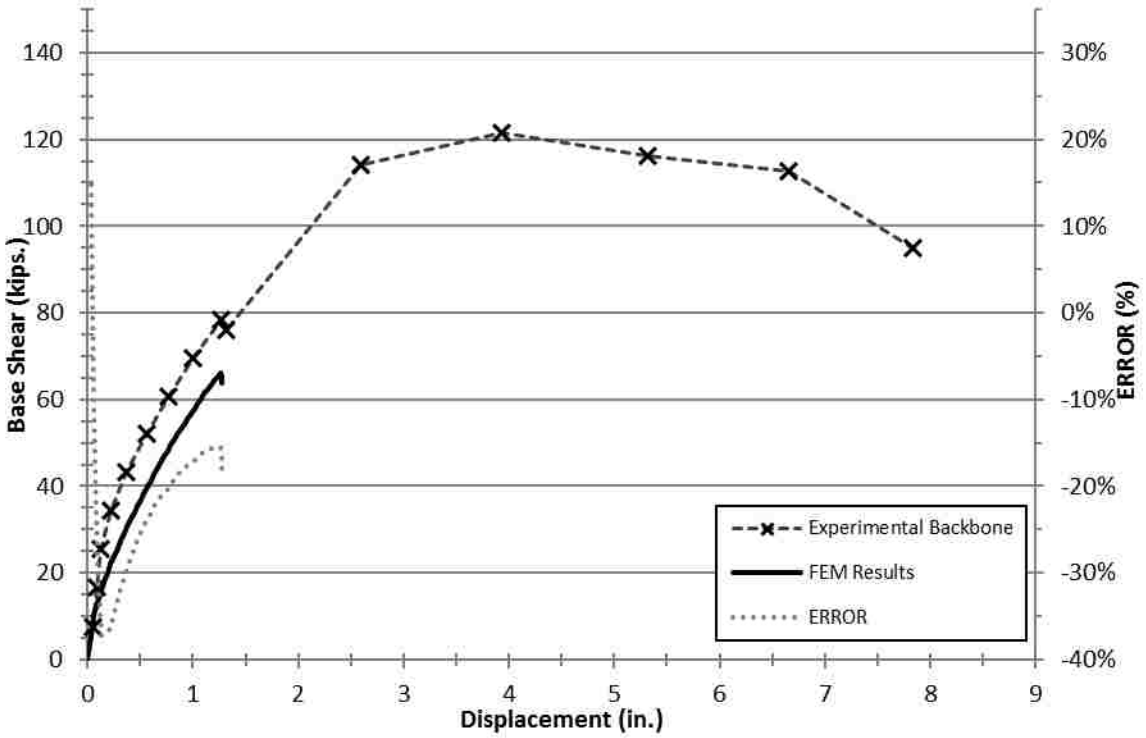


Figure 4.30 - Calt-3 Model Results | Base Shear-to-Displacement
(1 kip = 4.448 kN, 1 in. = 25.4 mm)

Up to the convergence failure, the base shear-to-displacement relationship predicted by the model was in relatively good agreement with the experimental results. As expected, due to a number of the errors discussed in Section 4.8, the model initially predicts an overly stiff response. This is likely due to compliance in the physical test setup and other displacement not associated with deformation of the column that is not reflected in the measured values. This was quickly replaced with an overly soft response, as the experimental results quickly showed a greater base shear than the model, beyond the initial base displacements. This soft response continued until the model failed to converge, which was immediately proceeded by a short but pronounced loss in strength. This sudden drop in capacity prior to convergence failure was also observed in the torque-to-twist response. However, the simulated torque values plateaued prematurely at a value of approximately 41.1 kip-ft (55.7 kN-m) and gradually decreased to 37.7 kip-ft (51.1 kN-m).

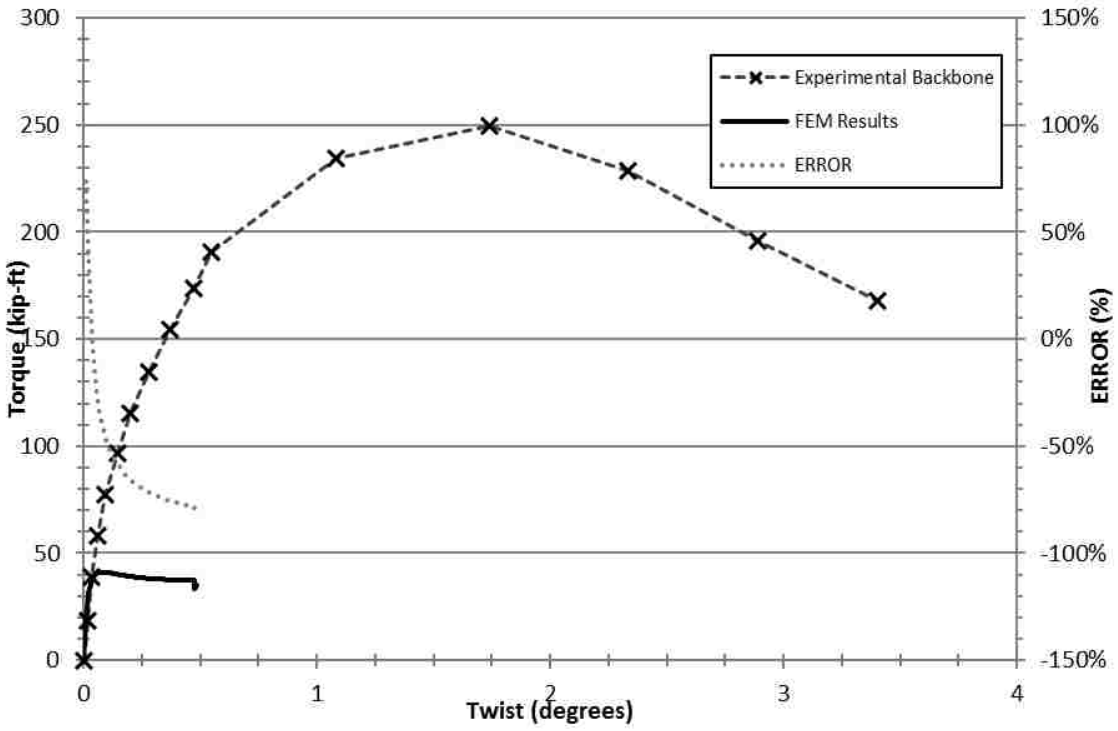


Figure 4.31 - Calt-3 Model Results | Torque-to-Twist (1 kip-ft = 1.356 kN-m)

As with Calt-1 and Calt-2, the torque-to-twist response degraded prematurely. This began at a torque of approximately 41.1 kip-ft (55.7 kN-m) and a twist of approximately 0.08 degrees. Similar to Calt-1, the torque response initially dropped and plateaued off at 37.6 (51.0 kN-m) until the model failed to converge. Just prior to convergence failure the torque response dropped from 37.7 (51.1 kN-m), to 33.5 (45.4 kN-m), and rebounded to 35.3 (47.9 kN-m) in the last 0.011 degrees of twist prior to failure. It is unclear if this dramatic change in torque response in a relatively short amount of time is related to the convergence failure; however, sudden changes in material stiffness can lead to convergence issues.

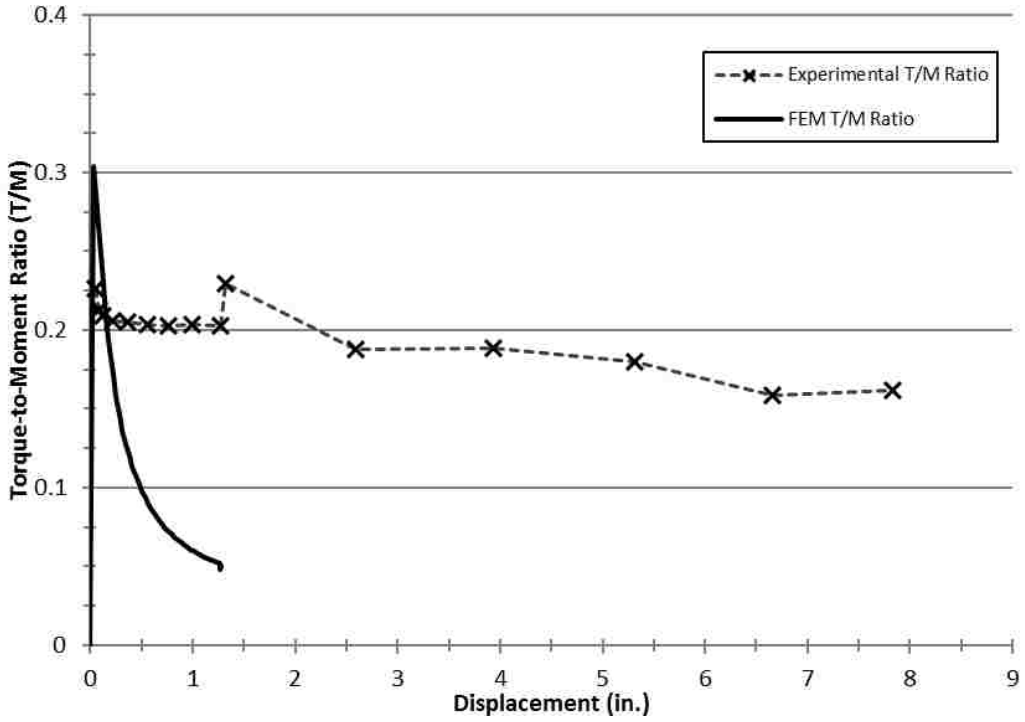


Figure 4.32 - Calt-3 Model Results | Torque-to-Moment Ratio (1 in. = 25.4 mm)

## 4.10. EXTENSION OF THE MODEL

Several attempts were made to extend the finite element model to similar RC bridge columns repaired and strengthened with externally bonded fiber reinforced polymer (FRP) composite jackets. The aim was to replicate the response of repaired

columns R-Calt-1 and R-Calt 2 discussed in Section 3. The cursory attempts to model the columns with an external jacket of shell elements, representing the FRP reinforcement of the repaired columns, all resulted in convergence failure as the model approached inelastic behavior, similar to what occurred with the finite element model of Calt-3 (Section 4.9.3). These efforts to extend the finite element model to the repaired configurations also included removal of the elements representing the portions of the spiral reinforcement removed as part of the repair (Section 3.3). No attempt to modify the properties of the elements representing the longitudinal reinforcement in the area of the splices was attempted as the local change in stiffness, associated with the larger cross section of bar and splice assembly, was assumed to be negligible in the overall response of the column. Additionally, it has been shown in coupon level testing that the couplers were capable of reaching loading consistent with yielding of the reinforcing bar and often facilitated failure away from the splice (Yang, 2014). As such it would not be expected that the inclusion of the couplers would significantly alter the model's response, due to the localized nature of stiffness changes, and would not be expected to alter the local failure mode of the longitudinal reinforcement within the framework of the model.

In attempting to obtain convergence for these preliminary modeling attempts linear isotropic properties were assigned to the shell elements in order to eliminate the possibility of convergence issues due to material parameters, to no effect. This suggests that the error, and resulting failure of the model, is a result of the several multi-body interactions and their effect on one another. While Abaqus precludes these constraints interacting on a single node, it does not preclude them acting on different nodes of the same element. As a result, there is potential for interactions between the surface tie constraints, between the surface of the concrete and the shell elements of the FRP jacket, and the nearby embedded constraints, of the reinforcing bars within the concrete. These interactions between kinematic constraints could be the source of some of the convergence difficulties experienced not only in the repaired RC column models but also the unstrengthened RC column models as well, due to the proximity of the embedded constraints to the upper and lower surfaces/constraints of the concrete.

In an effort to overcome these issues several modifications to the step incrementation and solution settings were attempted. These included increasing the

duration of the step and reducing the incrementation to the minimum allowable value. Additionally, both the number of equilibrium iterations allowed and the number of equilibrium iterations allowed between the rate of convergence checks, $I_0$ and $I_R$ respectively, were increased dramatically. These changes in combination result in a massive increase in computational expense as the set of equilibrium equations need to be solved more often to discern the impact of the same change in displacement. Additionally, the tolerances on field residuals, i.e., error, were increased in hopes that a stable solution could be obtain at the expense of accuracy. Unfortunately, neither approach had any noted impact on the ability of the repaired models, or the Calt-3 model, to reach convergence or even an increase in the displacement level at which convergence could be obtained.

# 5. CONCLUSIONS AND RECOMMENDATIONS FOR FUTURE WORK

## 5.1. CONCLUSIONS

This thesis outlined the development of a three-dimensional (3D) finite element model of reinforced concrete (RC) bridge columns with an oval shaped cross-section and interlocking spiral transverse reinforcement. A non-conformal meshing approach was adopted wherein the groups of elements representing the concrete, reinforcing bars, and other bodies were discretely meshed with defined interaction between them, as opposed to techniques where the bodies would share nodal locations. This approach allows for the helical spiral transverse reinforcement to be accurately represented without resulting in skewed or invalid elements within the encompassing solid elements representing the concrete.

The model was used to simulate the response of three RC columns subjected to combined flexure, shear, torsion, and axial load. The first of which, Calt-1, was loaded transversely to the weak axis with displacements consistent with those that produced a desired torque-to-moment ratio of 0.2 in the experimental study. The second, Calt-2, was loaded transversely to the weak axis with displacements consistent with those that produced a desired torque-to-moment ratio of 0.6 in the experimental study. The final column, Calt-3, was loaded 35 degrees off the weak axis with displacements consistent with those that produced a desired torque-to-moment ratio of 0.2 in the experimental study. Additionally, unsuccessful attempts were made to extend the model to assess the response of RC columns externally strengthened with FRP jackets.

Conclusions from this study are summarized as follows:

1. The model had mixed successes when attempting to simulate the response of the RC columns in this study. In the case of Calt-1, the model predicted the bending response well, but it failed to produce a realistic torsion-to-twist response. The peak base shear capacity predicted by the model [82.2 kip (366 kN)] was 94% of the experimental value [87.7 kip (390 kN)]. Similarly, the model was able to predict the bending response of Calt-2, although not with the same accuracy seen with Calt-1, and failed to reproduce the torque-to-twist response. The peak base shear capacity predicted by the model [75.7 kip (336.6 kN)] was 118% of the

experimental value [64.2 kip (285.4 kN)]. Although the results of the model are in reasonable agreement with those from the experiment, the model underestimated the reduction in flexural capacity (relative to that of Calt-1) caused by the larger torque-to-moment ratio. The measured peak base shear of Calt-2 had a decreased capacity of approximately 27% when compared to the measured peak base shear of Calt-1, whereas the model predicted an 8% reduction in peak base shear for Calt-2 relative to Calt-1. The inability to accurately reproduce the reduced base shear (and therefore flexural capacity) with increased torque/twist is believed to be a symptom of the model's inability to accurately predict the torque-to-twist response.

2. Unlike Calt-1 or Calt-2, the model was unable to reach a converged solution when presented with the biaxial bending condition of Calt-3. It is unclear if the convergence failure is related to the dramatic change in torque response exhibited by the model in a relatively short amount of time; however, sudden changes in material stiffness can lead to convergence issues.
3. The cursory attempts to model the columns with an external jacket of shell elements, representing the FRP reinforcement of the repaired columns in the experimental study, all resulted in convergence failure as the model approached inelastic behavior, similar to what occurred with the model of unstrengthened column Calt-3. In attempting to obtain convergence for these preliminary modeling attempts, linear isotropic properties were assigned to the shell elements in order to eliminate the possibility of convergence issues due to material parameters, to no effect. This suggests that the error, and resulting failure of the model, is a result of the several multi-body interactions and their effect on one another. While Abaqus precludes these constraints interacting on a single node, it does not preclude them acting on different nodes of the same element. As a result, there is potential for interactions between the surface tie constraints, between the surface of the concrete and the shell elements of the FRP jacket, and the nearby embedded constraints, of the reinforcing bar within the concrete. These interactions between kinematic constraints could be the source of some of the convergence difficulties experienced not only in the repaired RC column models

but also the unstrengthened RC column models as well, due to the proximity of the embedded constraints to the upper and lower surfaces/constraints of the concrete.

## 5.2. RECOMMENDATION FOR FUTURE INVESTIGATION

It has been shown by Prakash, Li, and Belarbi (2012) that the shear, bending, and torsional capacity of columns are related. As such, inaccurate torque-to-twist response would be expected to impact the base shear-to-displacement response as well, thereby inducing error. In the case of Calt-1 and Calt-2, although the base shear-to-displacement response of the model was in general agreement with the experimental results, it is unclear what impact the erroneous torque-to-twist response had on the base shear-to-displacement relationship (see Conclusion 1 in Section 5.1). Therefore, additional efforts are needed to improve the model under combined bending and torsion.

From Conclusion 3 in Section 5.1, it is recommended that further efforts be spent examining the proximity and number of elements separating multiple kinematic constraints. This would require a larger parametric study than the complexity of the model presented in this study would allow, due to computational demand. Consequently, this effort would warrant the creation an additional experimental effort to devise smaller, less complicated test specimens for calibrating the model. These experimental efforts could consist of concrete filled steel tubes CFST with a thin-walled steel exterior with varying levels of internal reinforcement embedded within them. These CFST specimens could then be tested under combinations of shear, bending, and torsion to develop an experimental database. This database would form a suitable foundation on which to build and calibrate a series of finite element models examining the rate of convergence and accuracy as a function of meshing parameters, with focus on the mesh formulation between the elements representing the internal reinforcement and the elements representing the external steel jacket. This would also form an experimental foundation for a deeper understanding of the interaction of axial, shear, bending, and torsional loading in RC columns.

# APPENDIX

## SAMPLE INPUT DECK FOR PLAIN RC COLUMN

```
*Heading
** Job name: CT1-DV-V5 Model name: Notional-Caltrans1-V5-DV
** Generated by: Abaqus/CAE 6.11-2
*Preprint, echo=NO, model=NO, history=NO, contact=NO
**
** PARTS
**
*Part, name=Cap-Sweep
*Node
      1,   6.38836575,  -11.7978296,         144.

[...]

           353,  -10.2386055,   2.64560556,   145.920944
*Element, type=R3D3
1, 104, 107, 108

[...]

334, 352, 351, 342
*Element, type=R3D4
 5,  84, 116,  15,   2

[...]

361, 352, 342, 336, 353
*End Part
**
```

```
*Part, name=Col-sans-elast
*Node
      1,  -13.2712831,   1.96800494,         143.

[...]

  34080,  -4.22588825,   12.1772785,          25.
*Element, type=C3D8R
    1,    52,   113,     9,     1,   478,   539,   435,   427

[...]

30968, 33600, 33267, 33268, 33654, 34026, 33693, 33694, 34080
*Nset, nset=_PickedSet2, internal, generate
     1,  34080,      1
*Elset, elset=_PickedSet2, internal, generate
     1,  30968,      1
** Section: Column
*Solid Section, elset=_PickedSet2, material="Original Concrete-V8"
,
*End Part
**
*Part, name=Elastic-Foot
*Node
      1,  -13.2712831,   1.96800494,          25.

[...]

    852,  -4.11437702,   11.9996805,          24.
*Element, type=C3D8R
  1,  52, 113,   9,   1, 478, 539, 435, 427
```

```
[...]

392, 402,  34,  35, 426, 828, 460, 461, 852
*Nset, nset=_PickedSet2, internal, generate
  1,  852,    1
*Elset, elset=_PickedSet2, internal, generate
  1,  392,    1
** Section: Elastic_Analog
*Solid Section, elset=_PickedSet2, material=Elastic_Concrete
,
*End Part
**
*Part, name=Elastic-hat
*Node
     1,  -13.2712831,   1.96800494,         144.

[...]

   852,  -4.22588825,   12.1772785,         143.
*Element, type=C3D8R
  1,  52, 113,   9,   1, 478, 539, 435, 427

[...]

392, 372,  39,  40, 426, 798, 465, 466, 852
*Nset, nset=_PickedSet2, internal, generate
  1,  852,    1
*Elset, elset=_PickedSet2, internal, generate
  1,  392,    1
** Section: Elastic_Analog
*Solid Section, elset=_PickedSet2, material=Elastic_Concrete
```

```
,
*End Part
**
*Part, name=Rebar-Long
*Node
      1,   12.5045366,   9.14109516,         144.

[...]

    980,   9.17722321,   13.1064329,         26.5
*Element, type=B31
 1,  1, 41

[...]

960, 980,  40
*Nset, nset=_PickedSet2, internal, generate
   1,  980,    1
*Elset, elset=_PickedSet2, internal, generate
   1,  960,    1
*Nset, nset=_PickedSet3, internal
  19, [...], 510
*Elset, elset=_PickedSet3, internal, generate
 433,  480,    1
*Nset, nset=_PickedSet4, internal
  21, [...], 557
*Elset, elset=_PickedSet4, internal, generate
 481,  528,    1
*Nset, nset=_PickedSet5, internal
  17, [...], 463,
*Elset, elset=_PickedSet5, internal, generate
```

```
 385,  432,    1
*Nset, nset=_PickedSet6, internal
 23, [...], 604,
*Elset, elset=_PickedSet6, internal, generate
 529,  576,    1
*Nset, nset=_PickedSet7, internal
 19, [...], 510
*Elset, elset=_PickedSet7, internal, generate
 433,  480,    1
*Nset, nset=_PickedSet8, internal, generate
   1,  980,    1
*Elset, elset=_PickedSet8, internal, generate
   1,  960,    1
*Nset, nset=Base_Long, generate
  2,  40,   2
** Region: (Rebar_Long:Picked), (Beam Orientation:Picked)
*Elset, elset=_I1, internal
   1, [...], 960
** Section: Rebar_Long  Profile: Number8
*Beam Section, elset=_I1, material=Longitudinal_Reinforcement-v5, poisson = 0.3,
temperature=GRADIENTS, section=CIRC
0.501
-1.,0.,0.
*Orientation, name=Ori-3
1., 0., 0., 0., 1., 0.
1, 0.
** Region: (Rebar_Long:Picked), (Beam Orientation:Picked), (Material
Orientation:Picked)
*Elset, elset=_I2, internal, generate
 385,  432,    1
** Section: Rebar_Long  Profile: Number8
```

*Beam Section, elset=_I2, material=Longitudinal_Reinforcement-v5, poisson = 0.3,
temperature=GRADIENTS, section=CIRC
0.501
-1.,0.,0.
*Orientation, name=Ori-1
1., 0., 0., 0., 1., 0.
1, 0.
** Region: (Rebar_Long:Picked), (Beam Orientation:Picked), (Material
Orientation:Picked)
*Elset, elset=_I3, internal, generate
 433,  480,    1
** Section: Rebar_Long  Profile: Number8
*Beam Section, elset=_I3, material=Longitudinal_Reinforcement-v5, poisson = 0.3,
temperature=GRADIENTS, section=CIRC
0.501
-1.,0.,0.
*Orientation, name=Ori-2
1., 0., 0., 0., 1., 0.
1, 0.
** Region: (Rebar_Long:Picked), (Beam Orientation:Picked), (Material
Orientation:Picked)
*Elset, elset=_I4, internal, generate
 481,  528,    1
** Section: Rebar_Long  Profile: Number8
*Beam Section, elset=_I4, material=Longitudinal_Reinforcement-v5, poisson = 0.3,
temperature=GRADIENTS, section=CIRC
0.501
-1.,0.,0.
*Orientation, name=Ori-4
1., 0., 0., 0., 1., 0.
1, 0.

```
** Region: (Rebar_Long:Picked), (Beam Orientation:Picked), (Material
Orientation:Picked)
*Elset, elset=_I5, internal, generate
 529,  576,    1
** Section: Rebar_Long  Profile: Number8
*Beam Section, elset=_I5, material=Longitudinal_Reinforcement-v5, poisson = 0.3,
temperature=GRADIENTS, section=CIRC
0.501
-1.,0.,0.
*End Part
**
*Part, name=Rebar-Ties
*Node
      1,   6.47384453,  -9.06812191,          24.

[...]

   1968,   9.47804165,  -3.98013902,    143.87793
*Element, type=B31
  1,   1,   5

[...]

1966, 1968,    4
*Nset, nset=_PickedSet2, internal, generate
    1,  1968,     1
*Elset, elset=_PickedSet2, internal, generate
    1,  1966,     1
*Nset, nset=_PickedSet3, internal, generate
    1,  1968,     1
*Elset, elset=_PickedSet3, internal, generate
```

```
   1,  1966,     1
** Section: Rebar_Tie  Profile: Number4
*Beam Section, elset=_PickedSet2, material=Longitudinal_Reinforcement-v5, poisson =
0.3, temperature=GRADIENTS, section=CIRC
0.252
0.,0.,-1.
*End Part
**
**
** ASSEMBLY
**
*Assembly, name=Assembly
**
*Instance, name=Cap-Sweep-1, part=Cap-Sweep
      0.,       0.,       0.
      0.,       0.,       0.,       0.,       0.,       1., 34.9999996046105
*End Instance
**
*Instance, name=Rebar-Long-1, part=Rebar-Long
      0.,       0.,       0.
      0.,       0.,       0.,       0.,       0.,       1., 34.9999996046105
*End Instance
**
*Instance, name=Rebar-Ties-1, part=Rebar-Ties
      0.,       0.,       0.
      0.,       0.,       0.,       0.,       0.,       1., 34.9999996046105
*End Instance
**
*Instance, name=Elastic-hat-1, part=Elastic-hat
      0.,       0.,       0.
      0.,       0.,       0.,       0.,       0.,       1., 34.9999996046105
```

```
*End Instance
**
*Instance, name=Elastic-Foot-1, part=Elastic-Foot
      0.,       0.,       0.
      0.,       0.,       0.,       0.,       0.,       1., 34.9999996046105
*End Instance
**
*Instance, name=Col-sans-elast-1, part=Col-sans-elast
      0.,       0.,       0.
      0.,       0.,       0.,       0.,       0.,       1., 34.9999996046105
*End Instance
**
*Node
     1,  -1.8497393e-13,  -1.26227543e-14,       155.
*Nset, nset=_PickedSet19, internal
 1,
*Nset, nset=_PickedSet20, internal, instance=Cap-Sweep-1, generate
   1,  353,    1
*Elset, elset=_PickedSet20, internal, instance=Cap-Sweep-1, generate
   1,  361,    1
*Nset, nset=_PickedSet22, internal
 1,
*Nset, nset=_PickedSet23, internal
 1,
*Nset, nset=_PickedSet33, internal, instance=Col-sans-elast-1, generate
    1,  34080,      1
*Elset, elset=_PickedSet33, internal, instance=Col-sans-elast-1, generate
    1,  30968,      1
*Nset, nset=_PickedSet34, internal, instance=Col-sans-elast-1, generate
    1,  34080,      1
*Elset, elset=_PickedSet34, internal, instance=Col-sans-elast-1, generate
```

```
    1,  30968,      1
*Nset, nset=_PickedSet37, internal, instance=Elastic-Foot-1, generate
 427,  852,    1
*Elset, elset=_PickedSet37, internal, instance=Elastic-Foot-1, generate
   1,  392,    1
*Elset, elset=Embed_Long, instance=Rebar-Long-1
   2,   [...], 959
*Elset, elset=Embed_Tie, instance=Rebar-Ties-1
   10,   [...], 1957
*Elset, elset=_CP-4-Cap-Sweep-1_SPOS, internal, instance=Cap-Sweep-1, generate
 174,  333,    1
*Surface, type=ELEMENT, name=CP-4-Cap-Sweep-1
_CP-4-Cap-Sweep-1_SPOS, SPOS
*Elset, elset=__PickedSurf30_S1, internal, instance=Elastic-hat-1, generate
   1,  392,    1
*Surface, type=ELEMENT, name=_PickedSurf30, internal
__PickedSurf30_S1, S1
*Elset, elset=__PickedSurf31_S1, internal, instance=Col-sans-elast-1, generate
   1,  392,    1
*Surface, type=ELEMENT, name=_PickedSurf31, internal
__PickedSurf31_S1, S1
*Elset, elset=__PickedSurf32_S2, internal, instance=Elastic-hat-1, generate
   1,  392,    1
*Surface, type=ELEMENT, name=_PickedSurf32, internal
__PickedSurf32_S2, S2
*Elset, elset=__PickedSurf35_S2, internal, instance=Col-sans-elast-1, generate
 30577,  30968,      1
*Surface, type=ELEMENT, name=_PickedSurf35, internal
__PickedSurf35_S2, S2
*Elset, elset=__PickedSurf36_S1, internal, instance=Elastic-Foot-1, generate
   1,  392,    1
```

```
*Surface, type=ELEMENT, name=_PickedSurf36, internal
__PickedSurf36_S1, S1
** Constraint: CP-Cap-Sweep-1-Concrete-Col-1
*Tie, name=CP-Cap-Sweep-1-Concrete-Col-1, adjust=yes, no rotation, type=SURFACE
TO SURFACE
_PickedSurf30, CP-4-Cap-Sweep-1
** Constraint: Cap
*Rigid Body, ref node=_PickedSet19, elset=_PickedSet20
** Constraint: Foot-Body
*Tie, name=Foot-Body, adjust=yes, no rotation
_PickedSurf36, _PickedSurf35
** Constraint: Hat-Body
*Tie, name=Hat-Body, adjust=yes, no rotation
_PickedSurf32, _PickedSurf31
** Constraint: Long_to_Col
*Embedded Element, host elset=_PickedSet33
Embed_Long
** Constraint: Tie_to_Col
*Embedded Element, host elset=_PickedSet34
Embed_Tie
*End Assembly
**
** MATERIALS
**
*Material, name=Elastic_Concrete
*Elastic
 2e+06, 0.2
** Elasto-plastic Approximation with plateu of AVG(Fy, Fu)
** E = 29,000 ksi
** Y = 90.4 ksi
** e_u = 12.2%
```

```
**
*Material, name=Longitudinal_Reinforcement-v5
*Density
 0.1,
*Elastic
 2.9e+07,0.
*Plastic
57000.,         0.
58000.,       3e-05
59000.,     4.5e-05
59500.,       6e-05
61000., 0.00337333
62500.,        0.01
60000.,       0.115
59500.,       0.118
59000.,       0.119
58000.,        0.12
55000.,       0.121
42500.,       0.122
25000.,       0.123
12000.,       0.124
 7000.,       0.125
 3750.,        0.13
 1900.,       0.135
 1150.,        0.14
  975.,       0.145
  950.,        0.15
** f_cu = 5.0ksi
*Material, name="Original Concrete-V8"
*Elastic
 4.0305e+06, 0.2
```

*Concrete Damaged Plasticity
36., 0.01, 1.25, 0.7, 0.002
*Concrete Compression Hardening
3181.82, 0.
3299.09, 3e-05
3417.27, 0.0001
3533.64, 0.00017
3643.64, 0.00023
3750., 0.0003
3851.82, 0.00036
3950., 0.00043
4042.73, 0.00049
4132.73, 0.00056
4216.36, 0.00063
4297.27, 0.00069
4372.73, 0.00076
4444.55, 0.00082
4511.82, 0.00089
4575.45, 0.00096
4633.64, 0.00102
4688.18, 0.00109
4737.27, 0.00115
4783.64, 0.00122
4823.64, 0.00128
4860.91, 0.00135
4893.64, 0.00142
4921.82, 0.00148
4945.45, 0.00155
4965.45, 0.00161
4980.91, 0.00168
4991.82, 0.00175

```
4998.18, 0.00181
 5000., 0.00188
4625.45,  0.0027
 4250., 0.00352
3875.45, 0.00434
 3500., 0.00516
3125.45, 0.00598
2340.82,  0.0065
1404.49,   0.007
 936.33,  0.0075
702.247,   0.008
*Concrete Tension Stiffening
50.,    0.
55., 1e-05
**
** BOUNDARY CONDITIONS
**
** Name: Fix_Col Type: Symmetry/Antisymmetry/Encastre
*Boundary
_PickedSet37, ENCASTRE
** Name: Fix_Long Type: Symmetry/Antisymmetry/Encastre
*Boundary
Rebar-Long-1.Base_Long, ENCASTRE
** ----------------------------------------------------------------
**
** STEP: Load
**
*Step, name=Load
*Static
1., 1., 1e-05, 1.
**
```

```
** LOADS
**
** Name: Conc_Force   Type: Concentrated force
*Cload, follower
_PickedSet22, 3, -150000.
**
** OUTPUT REQUESTS
**
*Restart, write, frequency=0
**
** FIELD OUTPUT: F-Output-1
**
*Output, field, variable=PRESELECT, frequency=10
**
** HISTORY OUTPUT: H-Output-1
**
*Output, history, variable=PRESELECT, frequency=10
*End Step
** ----------------------------------------------------------------
**
** STEP: Disp1
**
*Step, name=Disp1, nlgeom=YES, inc=10000000, unsymm=YES
*Static
0.001, 1., 1e-10, 0.002
**
** BOUNDARY CONDITIONS
**
** Name: Disp1 Type: Displacement/Rotation
*Boundary
_PickedSet23, 1, 1, 0.949885
```

```
_PickedSet23, 6, 6, 0.00518777
**
** CONTROLS
**
*Controls, reset
*Controls, analysis=discontinuous
**
** OUTPUT REQUESTS
**
*Restart, write, frequency=0
**
** FIELD OUTPUT: F-Output-1
**
*Output, field, variable=PRESELECT, frequency=25
**
** HISTORY OUTPUT: H-Output-1
**
*Output, history, variable=PRESELECT, frequency=10
*End Step
** ----------------------------------------------------------------
**
** STEP: Disp2
**
*Step, name=Disp2, nlgeom=YES, inc=100000000, unsymm=YES
*Static
0.001, 1., 1e-15, 0.001
**
** BOUNDARY CONDITIONS
**
** Name: Disp1 Type: Displacement/Rotation
*Boundary
```

```
_PickedSet23, 1, 1, 1.57443
_PickedSet23, 6, 6, 0.00845357
**
** OUTPUT REQUESTS
**
*Restart, write, frequency=0
**
** FIELD OUTPUT: F-Output-1
**
*Output, field, variable=PRESELECT, frequency=25
**
** HISTORY OUTPUT: H-Output-1
**
*Output, history, variable=PRESELECT, frequency=10
*End Step
** ----------------------------------------------------------------
**
** STEP: Disp3
**
*Step, name=Disp3, nlgeom=YES, inc=10000000, unsymm=YES
*Static
0.001, 1., 1e-15, 0.001
**
** BOUNDARY CONDITIONS
**
** Name: Disp1 Type: Displacement/Rotation
*Boundary
_PickedSet23, 1, 1, 3.19843
_PickedSet23, 6, 6, 0.0190722
**
** OUTPUT REQUESTS
```

```
**
*Restart, write, frequency=0
**
** FIELD OUTPUT: F-Output-1
**
*Output, field, variable=PRESELECT, frequency=25
**
** HISTORY OUTPUT: H-Output-1
**
*Output, history, variable=PRESELECT, frequency=10
*End Step
** ----------------------------------------------------------------
**
** STEP: Disp4
**
*Step, name=Disp4, nlgeom=YES, inc=10000000, unsymm=YES
*Static
0.001, 1., 1e-15, 0.001
**
** BOUNDARY CONDITIONS
**
** Name: Disp1 Type: Displacement/Rotation
*Boundary
_PickedSet23, 1, 1, 4.61462
_PickedSet23, 6, 6, 0.0277108
**
** OUTPUT REQUESTS
**
*Restart, write, frequency=0
**
** FIELD OUTPUT: F-Output-1
```

```
**
*Output, field, variable=PRESELECT, frequency=25
**
** HISTORY OUTPUT: H-Output-1
**
*Output, history, variable=PRESELECT, frequency=10
*End Step
** ----------------------------------------------------------------
**
** STEP: Disp5
**
*Step, name=Disp5, nlgeom=YES, inc=100000000, unsymm=YES, convert sdi=NO
*Static, direct=NO STOP
0.0005, 6.,
**
** BOUNDARY CONDITIONS
**
** Name: Disp1 Type: Displacement/Rotation
*Boundary
_PickedSet23, 1, 1, 17.9909
_PickedSet23, 6, 6, 0.107568
**
** CONTROLS
**
*Controls, reset
*Controls, parameters=time incrementation
7, 9, , , , , , , , ,
**
** OUTPUT REQUESTS
**
*Restart, write, frequency=0
```

```
**
** FIELD OUTPUT: F-Output-1
**
*Output, field, variable=PRESELECT, frequency=40
**
** HISTORY OUTPUT: H-Output-1
**
*Output, history, variable=PRESELECT, frequency=10
*End Step
```

# BIBLIOGRAPHY

ACI 318. (1989). Building Code Requirements for Structural Concrete. Farmington Hills, MI: American Concrete Institute.

ACI 318. (2014). Building Code Requirements for Structural Concrete. Farmington Hills, MI: American Concrete Institute.

ACI 440. (2002). *Guide for the Design and Construction of Externally Bonded FRP Systems forStrengthening Concrete Structures.* Farmington Hills, MI: American Concrete Institute.

Beck, J., & Kiyomiya, O. (2003). Fundamental pure torsional properties of concrete filled circular steel tubes. *J Mater Conc Struct Pavements*, 85-96.

Belarbi, A., Silva, P. F., & Bae, S.-W. (2008). Retrofit using CFRP Composites of RC Bridge Columns under Combined Loads. *Fourth International Conference on FRP Composites in Civil Engineering (CICE2008)*, (pp. 1-6). Zurich, Switzerland.

California Department of Transportation. (2006, June). Seismic Design Criteria Version 1.4. California, USA: Earthquake Engineering Service Center.

California Department of Transportation. (2007). Memo to Designers 20-4. *Earthquake Retrofit Guidelines for Bridges*. California, USA: Earthquake Engineering Service Center.

Collins, M. P. (1978). Towards a Rational Theory for RC Members in Shear. *Journal of the Structural Division*, 649-666.

Dassault Systems. (2010). *Abaqus 6.10 Theory Manual.* Providence, RI, USA: Dassault Systems.

Dassault Systems. (2010). *Abaqus 6.10 Users's Manual.* Providence, RI, USA: Dassault Systems.

Drucker, D. C., & Prager, W. (1952). Soil mechanics and plastic analysis for limit design. *Quarterly of Applied Mathematics*, 157–165.

Gong, A. (1989). *Experimental study on concrete-filled steel tubular short column under combined torsion and compression.* Bejing, China: Bejing Institute of Civil Engineering and Architecture.

Gopalaratnam, V. S., & Shah, S. P. (1985). Softening response of plain concrete in direct tension. *ACI JOURNAL*, 310-323.

Han, L., & Zhong, S. (1995). Study on the working mechanism and behavior of concrete-filled steel tubular (CFST) members subjected to compression, bending and torsion. *Journal of Building Structures*, 32-39.

Han, L.-H., Yao, G.-H., & Tao, Z. (2007). Behaviors of concrete-filled steel tubular members subjected to combined loading. *Thin-Walled Structures*, 600–619.

Han, L.-H., Yao, G.-H., & Tao, Z. (2007). Performance of concrete-filled thin-walled steel tubes under pure torsion. *Thin-Walled Structures*, 24-36.

He, R., Grelle, S., Sneed, L. H., & Belarbi, A. (2013). Rapid repair of a severely damaged RC column having fractured bars using externally bonded CFRP. *Composite Structures*, 225-242.

Hillerborg, A., Modeer, M., & Petersson, P. (1976). Analysis of Crack Formation and Crack Growth in Concrete by Means of Fracture Mechanics and Finite Elements. *Cement and Concrete Research*, 773-782.

Hognestad, E. (1951). *A Study of Combined Bending and Axial Load in Reinforced Concrete Members.* Urbana, Illinois: University of Illinois, Urbana.

Johnson, S. (2006). *Comparison of Nonlinear Finite Element Modeling Tools for Structural Concrete* . Urbana, Illinois: University of Illinois at Urbana-Champaign.

Karsan, I. D., & Jirsa, J. O. (1969). Behavior of concrete under compressive loadings. *Journal of the Structural Division*, 2535-2563.

Kmiecik, P., & Kaminski, M. (2011). Modelling of reinforced concrete structures and composite structures with concrete strength degradation taken into consideration. *ARCHIEVES OF CIVIL AND MECHANICAL ENGINEERING*, 623-636.

Kupfer, H., Hilsdorf, H. K., & Rusch, H. (1969). Behavior of concrete under biaxial stresses. *ACI JOURNAL*, 656-666.

Lee, J., & Fenves, G. L. (1998). PLASTIC-DAMAGE MODEL FOR CYCLIC LOADING OF CONCRETE STRUCTURES. *JOURNAL OF ENGINEERING MECHANICS*, 892-900.

Lefas, I. D. (1990). Behavior of reinforced concrete structural walls: strength, deformation characteristics, and failure mechanism. *American Concrete Institiude Structural Journal*, 23-31.

Lehman, D. E., & Moehle, J. P. (1998). Seismic Performance of Well-Confined Concrete Bridge Columns. *PEER-1998/01, Pacific Earthquake Engineering Research Center*, 316.

Lehman, D. E., Gookin, S. E., Nacamuli, A. M., & Moehle, J. P. (2001). Repair of Earthquake-Damaged Bridge Columns. *ACI STRUCTURAL JOURNAL*, 233-242.

Li, Q. (2012). *Performance of RC Bridge Columns under Cyclic Combined Loading including Torsion.* Houston: University of Houston Department of Civil and Environmental Engineering.

Li, Q., & Belarbi, A. (2011). Seismic Behavior of RC Columns with Interlocking Spirals under Combined Loadings Including Torsion. *The Twelfth East Asia-Pacific Conference on Structural Engineering and Construction* (pp. 1281-1291). Elsevier Ltd.

Lubliner, J., Oliver, J., Oller, S., & Onate, E. (1989). A Plastic-Damage Model For Concrete. *International Journal of Solids and Structures*, 299-326.

Mander, J. B., Priestley, M. J., & Park, R. (1988). Theoretical Stress-Strain Model for Confined Concrete. *Journal of Structural Engineering*, 1804-1826.

Mitchell, D., & Collins, M. P. (1974). Diagonal Compression Field Theory - A Rational Model for Structural Concrete in Pure Torsion. *ACI JOURNAL*, 396-408.

NZS 3101-Part 1. (1982). Code of Practice for the Design of Concrete Structures. Wellington, New Zealand: Standards Association of New Zealand.

NZS 3101-Part 2. (1982). Commentary on the Design of Concrete Structures. Wellington, New Zealand: Standards Association of New Zealand.

Prakash, S. S., Li, Q., & Belarbi, A. (2012). Behavior of Circular and Square Reinforced Concrete Bridge Columns under Combined Loading Including Torsion. *ACI Structural Journal*, 317-327.

Prakash, S., Belarbi, A., & You, Y.-M. (2010). Seismic performance of circular RC columns subjected to axial force, bending, and torsion with low and moderate shear. *Engineering Structures*, 46-59.

Reinhardt, H. W. (1984). Fracture mechanics of an elastic softening material like concrete. *Heron*, 1-42.

Tanaka, H. (1990). *Effect of Lateral Confining Reinforcement on the Ductile Behaviour of Reinforced Concrete Columns.* Christchurch, New Zealand: University of Canterbury.

Tanaka, H., & Park, R. (1993). Seismic Design and Behavior of Reinforced Concrete Columns. *ACI STRUCTURAL JOURNAL*, 192-203.

Vecchio, F. (1989). Nonlinear Finite Element Analysis of Reinforced Concrete Membranes. *ACI STRUCTURAL JOURNAL*, 26-35.

Vecchio, F. (1992). Finite Element Modeling of Concrete Expansion and Confinement. *Journal of Structural Engineering*, 2390-2406.

Vecchio, F. J., & Collins, M. P. (1986). The Modified Compression-Field Theory for Reinforced Concrete Elements Subjected to Shear. *ACI JOURNAL*, 219-231.

Wang, T., & Hsu, T. T. (2001). Nonlinear finite element analysis of concrete structures using new constitutive models. *Computers and Structures*, 2781-2791.

Weibull, W. (1939). The phenomenon of rupture in solids. *Generalstabens litografiska anstalts förlag*, 1-55.

Wilson, E. (2008). *Three Dimensional Static and Dynamic Analysis of Structures.* Berkeley, California: Computers and Structures, Inc.

Xu, J., Zhou, J., & Lee, G. (1991). Experimental studies on concrete-filled steel tubular medium and long columns under compression and torsion. *Third international conference on steel-concrete composite structures* (pp. 159-164). Fukuoka, Japan: ASCCS.

Yang, Y. (2014). *Seismic repair of bridge columns with interlocking.*

Yang, Y., Sneed, L. H., Morgan, A., Saiidi, M. S., & Belarbi, A. (2015). Repair of RC bridge columns with interlocking spirals and fractured longitudinal bars – An experimental study. *Construction and Building Materials*, 405-420.

Yang, Y., Sneed, L., Saiidi, M. S., Belarbi, A., Ehsani, M., & He, R. (2015). Emergency repair of an RC bridge column with fractured bars using externally bonded prefabricated thin CFRP laminates and CFRP strips. *Composite Structures*, 727-738.

Yu, T., Teng, J., Wong, Y., & Dong, S. (2010). *Engineering Structures*, 665-679.

Zhou, J. (1990). *The experimental research of concrete-filled steel tubular slender column under combined compression and torsion.* Bejing, China: Beijing Institute of Civil Engineering and Architecture.

# VITA

Adam Christopher Morgan was born November 2nd, 1986 in Clayton, Missouri, USA. After graduating from Missouri University of Science and Technology, with a bachelor's degree in both civil engineering and architectural engineering, in 2011, he began working on a master's degree in civil engineering at Missouri S&T. Under the advisement of Dr. Lesley Sneed, he assisted with research focused on developing repair techniques for reinforced concrete column and modeling their behavior by use of finite element modeling. In May 2018, he received his Master of Science in Civil Engineering from Missouri University of Science and Technology.